Thermodynamic Analysis of Active and Passive Drag Reduction Techniques for Elevated Enthalpy Hypersonic Reacting Flows

A thesis submitted
in partial fulfillment of the requirements
for the Degree of

DOCTOR OF PHILOSOPHY
in
Mechanical Engineering
by

AJAY PATIL

Roll No : 166103006

Under the guidance of

Dr. Vinayak Kulkarni

Department of Mechanical Engineering
Indian Institute of Technology Guwahati
Guwahati-781039

Certificate

It is certified that the work contained in the thesis entitled, **'Thermodynamic Analysis of Active and Passive Drag Reduction Techniques for Elevated Enthalpy Hypersonic Reacting Flows'**, presented by Ajay Patil, a student in the department of mechanical engineering, Indian Institute of Technology Guwahati, India, for the award of degree of Doctor of Philosophy has been carried out under my supervision and that this work has not been submitted elsewhere for a degree.

Dr. Vinayak N. Kulkarni
Professor
Dept. Mechanical Engineering
IIT Guwahati

ACKNOWLEDGEMENT

Firstly, I thank **God** to give me such an prestigous life and supportive environment which helped me to reach to this stage.

I would like to express my sincere gratitude towards my thesis supervisor **Dr. Vinayak N. Kulkarni**, Department of Mechanical Engineering, Indian Institute of Technology Guwahati, for his valuable guidance, caring, excellent lab environment and encouragement during the research work. It was an honour to work under him who has motivated me at each and every stage of my research to carry out my thesis work successfully. I thank him for giving an opportunity to work under him. I would also thank Department of Mechanical Engineering, Indian Institute of Technology Guwahati, to provide me superb computing facilities and beautiful premises to work for such an long period.

I am thankful to **Dr. Pranab K. Mondal** and **Dr. Dipankar N. Basu**, Department of Mechanical Engineering, Indian Institute of Technology Guwahati, for their kind suggestions and encouragement throughout the progress of this work. I am also thankful to **Dr. Peela N. Rao**, Department of Chemial Engineering, Indian Institute of Technology Guwahati for his expertise comments. I am deeply grateful to them for the long discussions that helped me sort out the technical details of my work. Thanks to current and previous HODs of Mechanical department, Indian Institute of Technology Guwahati, Professor **S.K. Dwivedy**, Professor **S.S. Senthivelan**, Professor **KSR Krishna Murthy** for their kind permission to make use of such an excellent research facilities in the department. Also, I am thankful to Professor **Amaresh Dalal** who taught me basics of computational fluid dynamics so clearly.

I would like to thank my colleagues **Mr. Shailendra Kumar** whose support helped me in completing my thesis work, **Mr. Ali**, **Mr. Jubajyoti**, **Ms. Amrita** who helped me manytimes to connect my lab PC to continue my study in corona pandemic period. I am also thankful to my seniors **Dr. Siddesh**, **Dr. Shuvayan**, **Dr. Mukesh** who always helped me in learning research related techniques rapidly.

Last, but not the least, I am deeply in debt to my family especially my parents **Vijay Patil**, **Mangla Patil** who always focused on my positive and overall development. Their unconditional love, support and blessings are solely responsible for my success. I can never pay their debts for such a nice upbringing of mine and the sacrifices they have done to ensure the fulfillment of my dreams. We know that without friends our research

life is incomplete. So, I thank all my friends for their constant support and valuable contribution in any ways.

Ajay Patil

ABSTRACT

Objects cruising at high speeds often encounter common problems of large wave drag and elevated surface heating. Thus, to have an efficient and durable flights flying at high altitude, these problems must be properly mitigated. Computational fluid dynamics is an effective tool to analyse the flow field induced during high speed to overcome these adverse effects. Hence, the current investigations consider computational fluid dynamics based finite volume method for two dimensional axisymmetric compressible non-equilibrium flows. Present solver which invokes Navier-Stokes equations and species continuity equations is developed in OP2 framework incorporating five species and eleven chemical elementary reactions often observed in high enthalpy flows. Both real gas flows and calorically perfect gas flows can be modelled using current solver. This solver also includes dependence of thermo-physical and flow properties on temperature field which is essential for high enthalpy flows. Before conducting current investigations, the present solver is well validated with measured experimental data for various flow condtions reported in open literature.

Initial investigations are based on counter flow injection and spike based drag reduction techniques to compare them on a common platform. These techniques being constitutionally different, are governed by different governing parameters but are assessed by percentage drag reduction. This assessment parameter is not suitable to compare two techniques of different categories, therefore, exergy destruction is proposed as a unified performance assessment parameter. Test case of supersonic flow over hemisphere, provided with counterflow injection, portrayed monotonic variation for percentage drag reduction and percentage exergy destruction for increase in injection pressure ratio. However, injection effectiveness, suitable assessment parameter for counterflow injection, shows inversion characteristics with a peak at specific injection pressure ratio. Mounting of a spike has also been assessed for different lengths and here as well percentage drag reduction and percentage exergy destruction showed similar trend with inverse relation among them. Spike and jet combination has also been considered to highlight the importance of percentage exergy destruction as a performance assessment parameter. Present investigations recommend percentage exergy destruction as a unified performance assessment parameter for passive, active and combinatorial drag reduction techniques.

Investigations are further extended to examine the effect of higher freestream stagnation enthalpy on flow field alteration for counter−jet drag reduction technique for a hemispherical object. Results include the real gas effects on flow field, wave drag and wall heat flux. Further the effect of various flow parameters is observed on surface pressure distribution, surface heat flux and drag force for the hypersonic flow over a hemisphere. Results proved that the perfect gas assumption overestimates surface properties and wave

drag value. Drag coefficient is found to reduce with freestream total enthalpy (H_o) in the presence of real gas effects. Higher pressure ratio of the jet has resulted in lower surface pressure and Stanton number on the object.

Efforts are further continued to reveal the thermodynamic behaviour of opposing jet technique which includes variation of entropy generation rate, exergy destruction and drag force analysis considering real gas effects. In this context, high entahlpy hypersonic flow over the hemisphere is studied. Numerical simulations are performed for different flow and geometrical parameters of jet and freestream to examine their impact on the flow field, drag reduction, exergy destruction and entropy generation rate. Results revealed that freestream parameters have lesser effect on drag values and flow field but there is monotonic variation in entropy generation rate and exergy destruction for constant momentum ratio of the jet. For given momentum ratio, jet parameters give almost linear reduction in entropy generation rate and exergy destuction while minor alterations in flow field and drag values are observed. Linear reduction in drag forces and sharp rise in entropy generation rate and exergy destruction is obtained with momentum ratio of the jet. Larger shock stand-off distance for higher momentum ratio gives higher entropy generation rate and exergy destruction making the process much more irreversible.

Lastly, real gas effects on surface pressure and flow field are analysed for the combinatorial technique (opposing jet and cavity) for high enthalpy hypersonic flow over the blunt body. A new thermodynamic parameter named entropy generation rate is proposed which can be used as a tool to analyze the performance of any drag reduction technique. Drag variation and entropy generation rate are also noted for different flow conditions and associated flow field alterations are examined. Results showed that perfect gas assumption over−estimates the surface pressure and wave drag as the surface pressure found is much lower when the real gas effects are considered. Significant flow field and shock alterations are observed when the real gas reactions are taken into consideration. Coefficient of drag and entropy generation rate vary in almost similar manner for different flow conditions. Introduction of cavity reduces the surface pressure, drag and entropy generation rate but significant reduction in these parameters is noted when the opposing jet is turned on. For given jet pressure ratio, opposing jet technique predicts lower drag and entropy generation rate as compared to combinatorial technique.

CONTENTS

LIST OF FIGURES

LIST OF TABLES

ABBREVIATIONS

$AUSM$	Advective upstream splitting method
CFD	Computational fluid dynamics
CFL	Courant friedrichs levy
DC	Direct current
FVM	Finite volume method
LPM	Long penetration mode
$N-S$	Naveir-stokes
PR	Jet pressure ratio
PS	Perfect solver
RS	Reacting solver
SPM	Short penetration mode

Nomenclature

a	Acoustic speed (m/sec)
A	Area ratio
A_p	Projected area of body (m^2)
A_s	Surface area of body (m^2)
C_d	Drag coefficient
C_{do}	Drag coefficient for no-spike or no-jet case
C_p	Coefficient of pressure
C_{pi}	Specific heat at constant pressure of i^{th} species (J/kgK)
d_b	Body diameter (mm)
D_m	Coefficient of mass diffusion (m^2/s)
DR	Percentage drag reduction
e	Specific internal energy (J/kg)
E	Total specific energy (J/kg)
e_i	Species internal energy (J/kg)
E_I	Inviscid flux in x direction
F_I	Inviscid flux in y direction
G_I	Inviscid axi-symmetric source term
E_v	Viscous flux in x direction
F_v	Viscous flux in y direction
G_v	Viscous axi-symmetric source term
h_1	Freestream specific enthalpy (J/kg)
h_2	Jet specific enthalpy (J/kg)
h_3	Outlet specific enthalpy (J/kg)
h_i	Specific enthalpy of i_{th} species (KJ/kg)
h^0_{fi}	Heat of formation of species i$(KJ/kmol)$
H_o	Stagnation enthalpy (KJ/kg)
k	Thermal conductivity (W/mK)
K_{bi}	Backward reaction rate coefficient $(\text{cm}^3/molsec)$
K_{fi}	Forward reaction rate coefficient $(\text{cm}^3/molsec)$
L	Length of cavity (mm)
$\dot{m}_1$	Freestream mass flow rate (kg/s)
$\dot{m}_2$	Jet mass flow rate (kg/s)

MW_i	Molecular weight i^{th} species (kg/mol)
p	Pressure (N/m^2)
PR	Jet pressure ratio
q_x	Heat flux in x direction (J/m^2)
q_y	Heat flux in y direction (J/m^2)
r	Cavity radius (mm)
r_j	Jet radius (mm)
R	Sphere radius (mm)
R_u	Universal gas constant $(J/kmolK)$
R_{ma}	Jet momentum ratio
Re	Reynolds number
s_1	Freestream specific entropy (J/kgK)
s_2	Jet specific entropy (J/kgK)
s_3	Outlet specific entropy (J/kgK)
$\dot{S}_g$	Entropy generation rate (W/K)
S	Source term
t	time (s)
T	Temperature of the fluid (K)
T_R	Reference temperature (K)
T_{aw}	Adiabatic wall temperature (K)
T_w	Wall temperature (K)
T_{ref}	Reference Temperature (K)
T_∞	Freestream temperature (K)
u_∞	Freestream velocity (m/s)
u	Velocity in x direction (m/sec)
u_{di}	Difusion velocity in x direction (m/sec)
v	Velocity in y direction (m/sec)
v_{di}	Diffusion velocity in y direction (m/sec)
X	Conservative variable vector

Greek Symbols

α	Constant ($\alpha = 0$ for 2D and $\alpha = 1$ for 2D-axisymmetric flows)
Δ	Shock stand-off distance (mm)
η	Injection effectiveness

κ	Courant friedrichs levy number
ρ_∞	Freestream density (kg/m^3)
$\tau_{11}, \tau_{12}, \tau_{22}, \tau_{33}$	Shear stress components (N/m^2)
θ	Angle (Deg)
μ	Fluid viscosity (Ns/m^2)
μ_{ref}	Reference viscosity (Ns/m^2)

CHAPTER 1

INTRODUCTION

This chapter includes some introduction about aerodynamics flows and its characteristics. Various problems often encountered during high speed flows and their respective mitigation by different techniques are also discussed. Detailed literature related to these techniques and their conclusions are also presented and at last some objectives of the current work derived from in-depth literature review is also discussed.

1.1 Aerodynamics

The updated technology of today's world is only possible due to continuous efforts of numerous reserachers from many centuries in various fields. Evolution in aerodynamic technology also faced many hurdles to arrive at existing state. The imagination to make flying vehicles for human started from impersonating the bird flight but due to lack of comprehensive knowledge and unawareness of fundamental theories, this desire to fly remained only an imagination. Pioneering work in imitating the flying trajectory of birds initiated in 15^{th} century when 'Ornithopter' showed some hope to achieve impossible. It faced many failures, as often encountered in any innovating technique. Ornithopter's contribution gave significant thrust to enhance research in this area. Further, the discovery of air balloons and introduction of Glider in 1783 helped to the research. Later, need of separate propulsion system was required for manned flight. Afterwards, Wright brothers demonstrated the first human flight on December 17, 1903 using gasoline powered engine. This acheivement helped to acquire the belief of human flying. But the desire to fly faster gained popularity thereafter. As a result, the first supersonic flight was possible in 1947. This innovation helped for faster transport in militants and civil applications. Devotion and constant efforts of many researchers is still going on for future upgradation in aerodynamic field.

Gas dynamics deals with understanding the compressible flows over high speed aircrafts, missile, re-entry vehicle etc. There are various flow regimes which are classified based on flow Mach number. Among those, flows with Mach number more than 1 are supersonic while hypersonic flows are characterised when flow Mach number exceed 5. Vehicles exposed to these flows often encounter various undesirable effects like excessive wave drag, surface heating, shock wave boundary layer interaction etc. These flow features are important and must be dealt with care to avoid complete failure. For the safe and effective operation of high speed flights for long durations, all these effects must be properly mitigated. For flows at elevated temperatures, dissociation and ionization reactions can take place which affect the flow field significantly and thus their effects must be taken into consideration for accurate prediction of flow field and aerodynamic coefficients.

1.2 Elevated temperature effects

For low speed or subsonic vehicles, there are very less chances of chemical reactions to occur as alterations in temperature field are minor. Thus, calorically perfect gas model can easily be used to solve the flow field variables. In this model, thermo-physical properites like specific heat at constant pressure (C_p), specific heat at constant volume (C_v), thermal conductivity (k) and flow properties like viscosity (μ) are assumed to be constant. Also, the concentration of chemical species of flow does not undergo any alteration in chemical composition.

For high speed vehicles (supersonic or hypersonic), there is chance of formation of very strong detached shock in front of body. Thus, very high post-shock temperature can be observed due to conversion of flow kinetic energy into flow internal energy which is non-recoverable making this process highly irreversible. This elevated temperature zone results in commencement of dissociation chemical reactions. Air is mainly composed of gases like oxygen (O_2) and nitrogen (N_2). Concentration of these species alters in these high temperature zones. Also, specific heat at constant pressure (C_p), specific heat at constant volume (C_v), thermal conductivity (k) and viscosity (μ) change with temperature and this change must be incorporated in solution methodology to accurately capture the flow information as calorically perfect gas assumption remains no longer valid for such conditions.

1.3 Reactions of gases at high temperature

Various chemical reactions are often encountered during high speed and high enthalpy flows. These reactions are listed below:

1.3.1 Dissociation

When the temperature of air is below 2500 K, no reaction occurs in it but as the temperature exceeds 2500 K, oxygen molecules starts to dissociate to form oxygen atoms by absorbing heat from surroundings and this process continues upto 4000 K temperature. When the temperature crosses 4000 K, nitrogen molecules also start to dissociate and it completely dissociates upto 9000 K. Full details of dissociation and ionisation reactions with the temperature range are depicted in Fig 1.1.

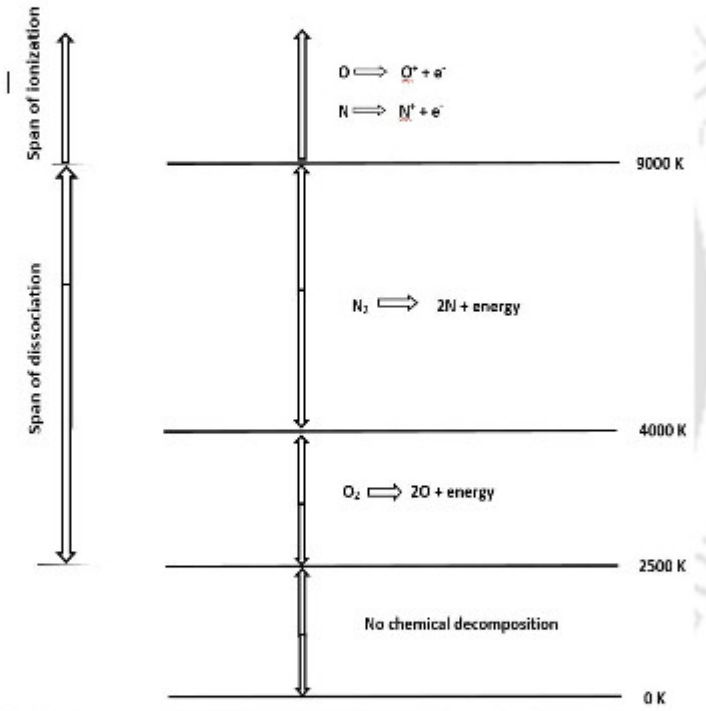

Figure 1.1: Reactions of gases at elevated temperature

$$O_2 + energy \rightarrow 2O(2500K < T) \tag{1.1}$$

$$N_2 + energy \rightarrow 2N(4000K < T < 9000K) \tag{1.2}$$

1.3.2 Ionisation

When the temperatures of air goes above 9000 K, atoms of oxygen and nitrogen get converted into their respective ions by absorbing energy from surroundings.

$$O + energy \rightarrow O^+ + e^-(T > 9000K) \tag{1.3}$$

$$N + energy \rightarrow N^+ + e^-(T > 9000K) \tag{1.4}$$

1.4 Models of compressible flows

In hypersonic flows, high temperature regions are encountered at post-shock location. So appropriate model should be used for accurately solving the fluid flow problems. Different models based on air temperature range are discussed below:

1.4.1 Perfect gas model

This model is applicable when the temperature of flow is below 2500 K and there are no chemical reactions occurring in fluid flow.

1.4.1.1 Calorically perfect gas flow

In this type of gas flow, specific heats of gas (C_p ,C_v) and specific heat ratio remain constant with temperature while the enthalpy and internal energy of air are linear function of temperature.

$$h = C_pT \tag{1.5}$$

$$e = C_vT \tag{1.6}$$

1.4.1.2 Thermally perfect gas flow

In this type of gas flow, specific heats of gas (C_p ,C_v) and specific heat ratio are functions of temperature. Total enthalpy and internal energy of air are obtained by integrating the differential values in the flow field.

$$dh = \int C_pdT \tag{1.7}$$

$$de = \int C_vdT \tag{1.8}$$

1.4.2 Reacting gas model

Real gas flows often undergoes alterations in chemical composition at elevated thermal conditions. These alterations in chemical composition take place at certain rate depending on extent of thermal elevation and this rate is generally termed as reaction time (t_r).

Let t_f be the flow time scale. When the temperature of air flow exceeds certain temperature limit, chemical reactions commence within the flow and reacting gas model must be considered to accurately solve the flow field. Various types of models are shown in fig 1.2 and discussed below:

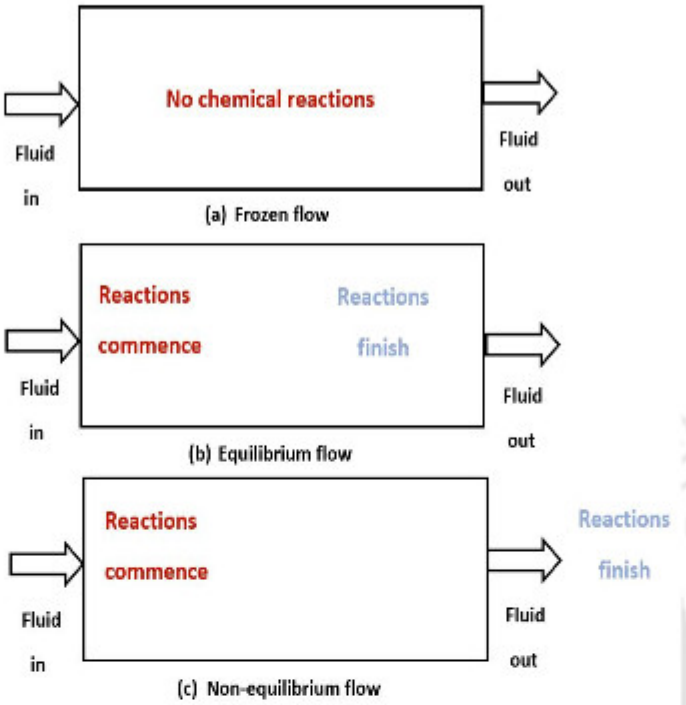

Figure 1.2: Models used in aerodynamic flows

1.4.2.1 Frozen flow model

This model can be used when the time scale of reactions of air is very large such that air can pass over the surface before the reaction commences and hence it doesn't experience any change in its chemical composition ($t_r >>>> t_f$).

1.4.2.2 Equilibrium flow model

This model is used if the time scale of reactions is very small such that air would experience sudden change in its properties. When the temperature of air flow exceeds 2500 K, then air molecules start to dissociate into atoms and this model must be used to accurately solve the flow field ($t_r <<<< t_f$).

1.4.2.3 Non-equilibrium flow model

This model is taken into consideration when the time scale of reactions is of same order of flow time scale. Reactions gets started in the flow field but do not complete till the

flow completely passes over the surface ($t_r \sim t_f$).

1.5 Drag and heat reduction techniques

Vehicles flying at hypersonic speeds like satelite, launch vehicles, re-entry vehicles, aircrafts and missiles have blunt nose shapes. Surface heating is inversely proportional to the nose radius of the body. Thus to reduce the thermal loads on the body surface, nose of these objects is intensionally blunt. Such blunted configuration reduces thermal load over object but increases the surface pressure and related wave drag. Higher amount of fuel is consumed due to such large drag force. To overcome both the problems of high suface heating and large drag force, different active and passive techniques are successfully employed by numerous researchers. These methods induce alterations in bow shock structure making it relatively weaker to form a new flow field around the body which results in lowered wave drag and surface heating over the body. Some of the active and passive techniques used in the current work are stated and explained in detail below,

1) **ACTIVE TECHNIQUES**

a) Counter-flowing jet or opposing jet

b) Upstream energy deposition

2) **PASSIVE TECHINQUES**

a) Retractable aero-spike

b) Forward facing cavity

Opposing jet

Releasing a counter-jet near the stagnation point from the body is an active technique for drag and heat reduction in high speed flows over blunt body [1]. For lower jet pressures flow field is highly unstable and steady state is seen only when jet pressure goes above critical value. Figure 1.3 depicts the steady flow features in which a counter-jet is issued from blunt body. For any given jet pressure the bow shock is forced to move away from the body and thus the high pressure region is moved away from body. When PR_{jet}>PR_{∞} then an under-expanded jet issues from blunt body. This jet expands as it

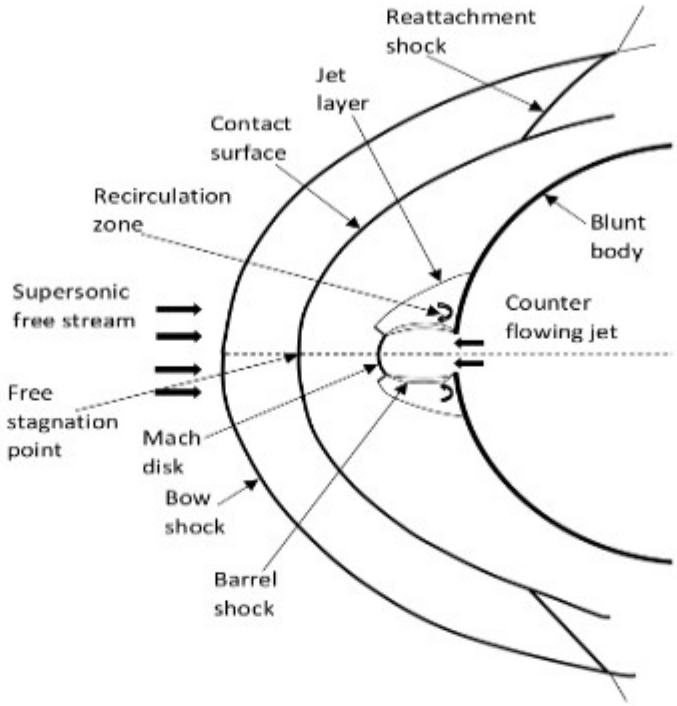

Figure 1.3: Flow features of counter-flowing jet based drag reduction method

encounters expansion waves near the nose of body. These set of expansion waves turns into set of compression waves as they interact with jet boundary which eventually form a compression shock. If the jet is too under-expanded then this compression shock looks like a barrel and thus called a barrel shock. The pressure of jet upon expansion becomes lower than free-stream pressure but to match the pressure of both streams, a Mach disk is formed as shown in figure. Free stagnation point is formed where both the streams meet after the Mach disk. Then the jet turns in the free-stream direction forming a contact surface with it. Some fluid from the jet gets entrained in the recirculation zone which acts as an envelope for the body and thus pressure and heat flux on body surface lower which in turn reduces the drag on body [2]. The flow hits the surface at reattachment point and thus creating a reattachment shock and this shock also interacts with the bow shock as shown in Fig 1.3.

Energy Deposition

Another effective method to reduce drag is by depositing energy from an energy source upstream of the flow. This is an active technique to reduce drag which forces the flow to separate early [3] and thus forming a low pressure region downstream of energy source which reduces drag force on body as shown in Fig 1.4. Amount of drag force reduced depends on the location and strength of energy source [4]. Energy can be released in

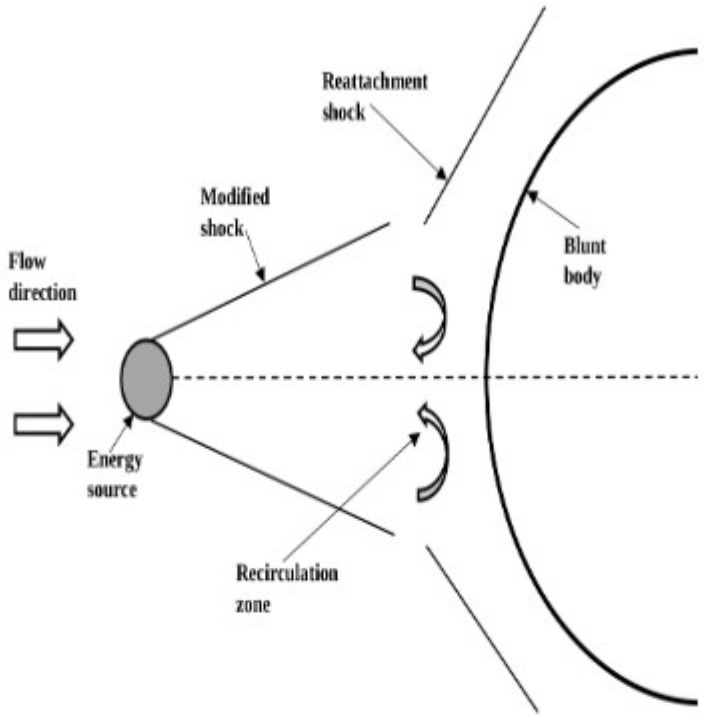

Figure 1.4: Flow features of Energy release based drag reduction method

number of ways like ensuring exothermic reaction, laser, micro-wave etc and this energy release generates low density area near the stagnation point [5] resulting in lowered drag force. Major drawback of this process is that it may enhance body surface heating as energy is being released in the fluid flow.

Aero-spike

During high speed flow over blunt body, strong bow shock is observed in front of the body. High pressure and temperature regions are seen after the shock near stagnation point. In this type of drag and heat reduction technique, an aero-spike is attached at nose of blunt body as shown in Fig 1.5. This aero-spike converts strong bow shock in relatively weaker conical shocks and also separates the flow from surface to form recirculation zone [6]. This separated flow region is comprised of large vortices which act as resistance for incoming high speed flow and avoid the direct exposure of body surface to the freestream flow resulting in lowering of wave drag on the body. Lower surface pressures are observed in this zone as it acts as a blanket in front of the body. Surface heat transfer is also lowered in this area as hot free-stream gases doesn't come in direct contact with the body surface. This is a relatively cheap and efficient method to reduce heat and drag on body but drawback is that it requires frequent replacements as the tip of spike gets overheated during high speed flows.

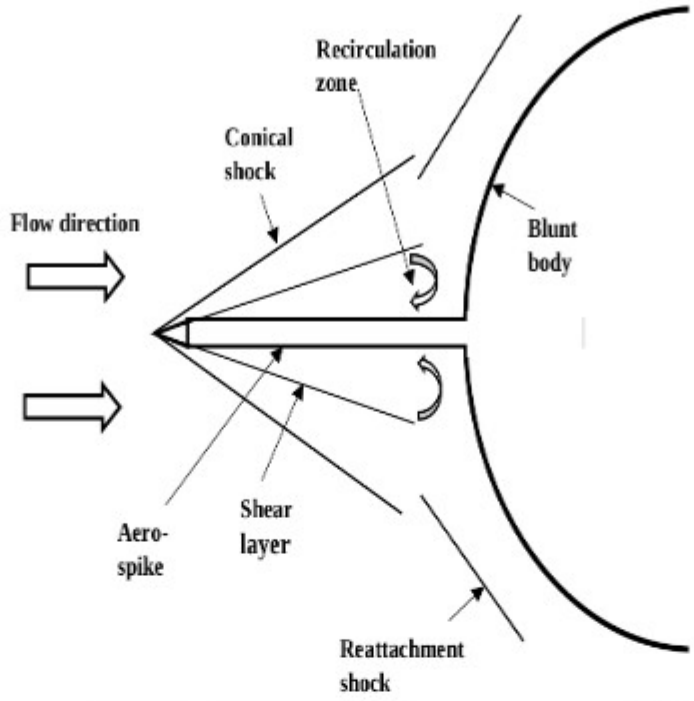

Figure 1.5: Flow features of spike based drag reduction method

Forward facing cavity

As there is formation of strong detached shock in front of body which gives elevated heat flux and drag on body. To mitigate these problems, a forward facing cavity is attached at the vicinity of nose, near the stagnation point, as shown in Fig 1.6. Introduction of cavity allows the flow to swirl around the nose of body and this flow pattern results in lowering of heat flux on body. Shock stand-off distance does not alter much but the high temperature region formed at post shock location diminishes in size. This is also one of the passive technique but one problem with this technique is that it increases the wave drag on the body.

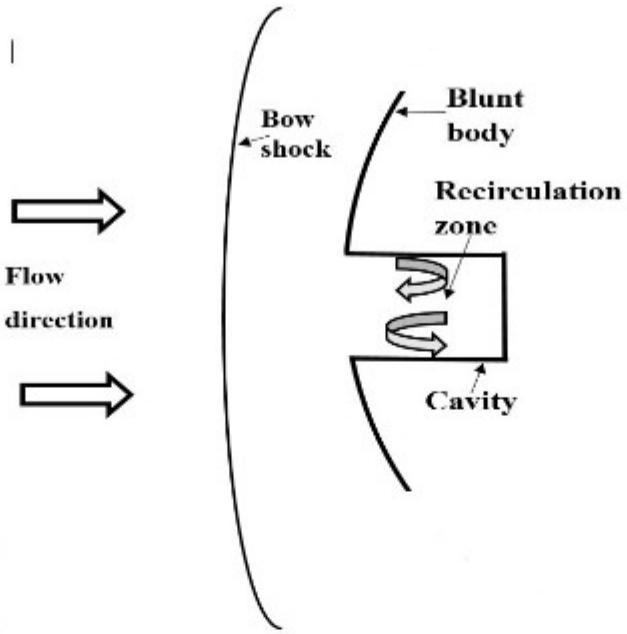

Figure 1.6: Flow features of cavity based drag reduction method

1.6 Literature review

Flights in the hypersonic flow regime are only possible if surface heat flux is reduced to the sustainable limits of the common materials used for designing thermal protection system. Having nose part of the vehicle blunt reduces the surface heat flux but still keeps it higher than the actual applicable limits. Further, introduction of leading edge bluntness enhances the drag force encountered by the vehicle. Hence, hypersonic aerodynamics always deals with reduction of surface heat load and drag force so as to make the flight feasible, safe and affordable. Different drag reduction techniques are documented in the previous section which include mounting of metallic spike on the nose, deposition of energy upstream of the vehicle and injection of fluid from the stagnation point. Literature review related to different flow alteration techniques and associated simulation methods are given in this section.

1.6.1 Review of drag and heat reduction by counter-flowing jets

Finley [7] studied jet flow from body opposing supersonic free-stream as depicted in Fig 1.7(a). Surface pressure was found to be lower in recirculation zone and it increased to peak value at reattachment point and then reduced again as shown in Fig 1.7(b). Increasing jet Mach number was noticed to reduce surface pressure for steady jets as area

of dead air zone grows. Surface pressure was found to be lower for larger jet diameters. Hayashi et al [8] experimentally examined the effect of opposing jet on surface heat flux

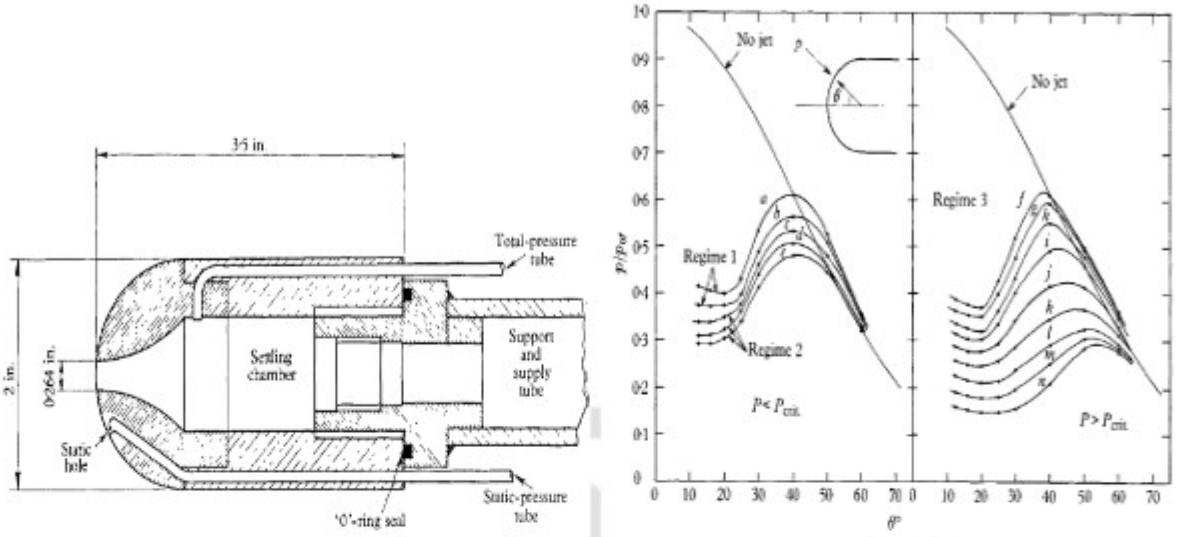

Figure 1.7: (a) Model used in experiment (b) Surface pressure distribution [7]

for supersonic flows. For lower jet pressure, flow field was unsteady and it gave higher surface heat flux as compared to no jet case while for higher jet pressure, surface heat flux was lower since recirculation area covers the body surface. Li et al [9] examined the effect of jet parameters on drag and heat reduction for hypersonic vehicles. They found that for odd number of jet, drag reduces with increase in jet number as the orifice was located at centre of stagnation line and high pressure region after bow shock was moving away from body surface but for even number of jets the trend obtained was opposite. Morimoto et al [10] examined the effect of opposing jet through extended nozzle on aerodynamic heating for high enthalpy flows. They concluded that Stanton number reduces with increase in nozzle length and value of peak Stanton number moves downstream as reattachment point shifts downstream. Also heat flux increased behind the recompression shock wave and also behind the impinging shock and thus heat flux had two peak values on body surface. Haung et al [11] studied the effect of counter-flowing jet on flow properties in supersonic flows. As per their observation shock stand-off distance and height of Mach disk increase with jet pressure and triple point moves downstream. Increasing jet Mach number increased Mach disk height and subsonic region near Mach disk got increased. Heat flux was found to be lower but surface pressure was higher for low jet Mach number so need of optimization was proposed. Kulkarni et al [12] experimented with counter-flow drag reduction using supersonic jet in high enthalpy flows and accelerometer force balance for drag measurement. The schlieren image showing key flow features during experiments is shown in Fig 1.8(a). Increasing jet pressure reduced drag as elucidated in Fig 1.8(b) while increasing freestream enthalpy reduced drag faster with jet pressure due to dissoci-

ation reaction near free stagnation point and recombination at same point due to cold jet which adds energy in shock layer which in turn reduces stagnation pressure. Venukumar

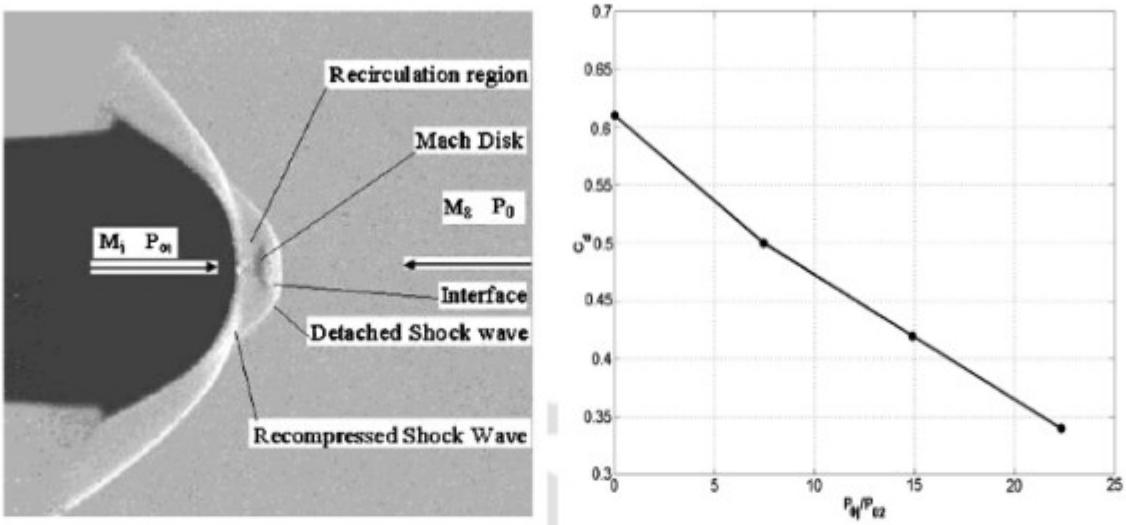

Figure 1.8: (a) Schlieren image (b) Drag coefficient variation [12]

et al [13] examined drag reduction by supersonic jet for blunt body in hypersonic flow. They found that drag reduction percent increases with jet pressure as jet moves out from nozzle and flows over recirculation region to reattachment point entraining some fluid as it flows downstream. Meyer et al [14] studied heat and drag reduction with a forward facing jet for hypersonic flows. They found that with increase in jet Mach number, jet thrust on body reduces which brings shock closer to body and forces recirculation zone to shrink and thus heating of body enhances. In other observation, it was noticed that, as jet diameter increases, reattachment point shifts downstream and skin friction drag on body surface lowers. Haibo et al [15] examined effect of angle of attack for blunt body with opposing jet flow. They concluded that drag increases with angle of attack but surface heat flux on windward generatrix increases while it reduces on leeward generatrix. Also recompression shock wave combines with detached bow shock on leeward side and it becomes even stronger, while on windward side, it forms local high temperature region near jet exit. Zhou and Ji [16] investigated for drag reduction on spherical body with opposing jet. They focused on the effect of jet pressure, jet size and angle of attack on drag and found that drag reduces faster with angle of attack in unsteady mode than in steady mode due to faster shortening of shock stand-off distance. It was also noted that, reducing jet diameter increases surface pressure as jet mass flow rate lowers with jet diameter which brings bow shock closer to body. Warren [17] experimentally studied effect of type of injection method and angle of incidence on surface pressure and heat flux. The model employed in experiments is shown in Fig 1.9(a). Measured surface pressure was lower near nose of body but it was almost same at shoulder for straight-out

injection as depicted in Fig 1.9(b). For injection with swirl, heat flux on body increased in comparison with no jet case as swirl gives high velocity to jet in tangential direction and increases surface shear and thus heat flux by Reynolds analogy. Gerdroodbary et al

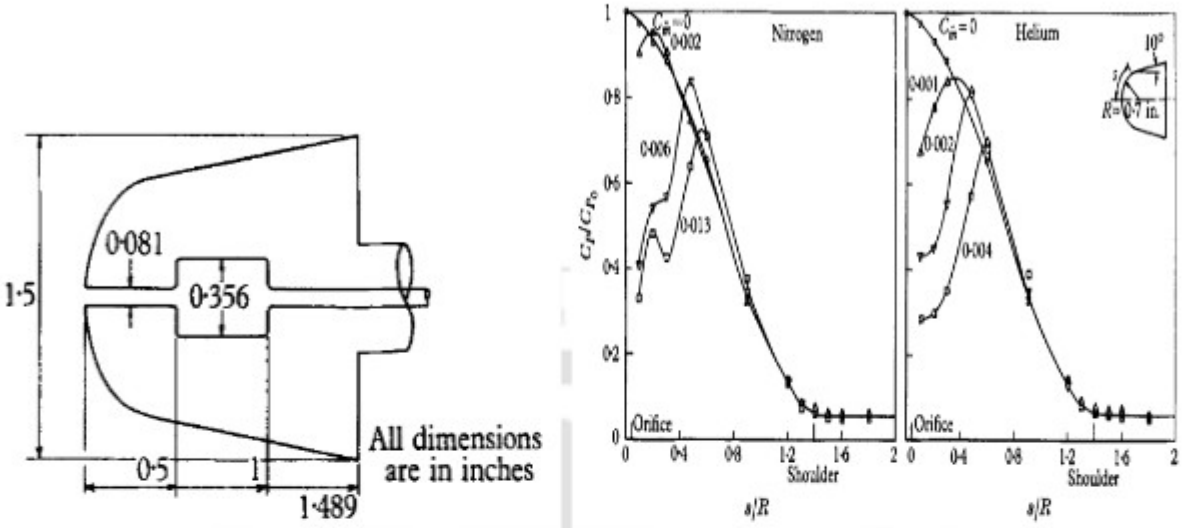

Figure 1.9: (a) Model used in experiment (b) Surface pressure variation [17]

[18] examined effect of angle of incident shock wave on mass distribution of jet injectant for transverse injection. They indicated that increasing shock angle reduces mass distribution of hydrogen as shock wave interacts with bow shock much strongly and subsonic region shifts upstream of flow. As a result, shock wave pushes the barrel shock more downstream to form narrow Mach disk. Daso et al [19] aimed at the effect of flow rate, attack angle, diameter, Mach number of jet on heat flux of body. They showed that at low flow rates of jet, bow shock wave gets divided in number of compression waves while all compression waves coalesced into thin bow shock at higher flow rates. At lower injection pressures, unsteadiness were seen while flow field became steady at higher flow rates. Another important note was that, heat flux on body surface reduces with jet flow rate and jet Mach number and it is even negative for larger flow rates. Gerdroodbary et al [20] examined effect of jet gas on surface heating and flow structure for hypersonic flows. As per their results, heat load on body was higher for helium than carbon-dioxide jet as helium jet gives larger jet penetration. Carbon-dioxide jet was seen to transit to SPM (short penetration mode) from LPM (long penetration mode) earlier than helium counter-flowing jet as carbon-dioxide has lower diffusion coefficient than helium. Sahoo et al [21] experimentally studied effect of jet species on surface heat transfer and drag on object. They found higher reduction in heating near nose of body for air injection while this reduction was higher for helium at downstream locations on body because helium is a lighter gas and it expands faster along surface so that cooling takes place at later portion of body surface. It was also recorded that, injection of gases increases density in

stagnation region which accelerates free-stream flow and increases drag on body which rises more for heavier injectant resulting in much higher drag. Lopatoff [22] studied effect of jet Mach number and jet thrust on drag of body. Counter-flowing jet produced strong vortex ring in vicinity of nose of body so high negative pressure was seen in this region which lowered drag on body. Imoto et al [23] had focus on effect of coolant type and pressure ratio on heating of model surface. Jet pressure ratio can be defined as $PR = \frac{P_{oj}}{P_{o\infty}}$. Here P_{oj} and $P_{o\infty}$ are jet and freestream total pressure respectively. They indicated that Stanton number increases for low pressure ratios of nitrogen jet at shoulder of body due to relocation of reattachment point of high temperature flow. Stanton number difference between opposing jet and no-jet case was insignificant downstream on body surface. Helium gas reduced heating at small mass flow rate of jet as compared to nitrogen jet; due to smaller molecular weight of helium it gives higher velocity to it than other gas for sonic injection. Gerdroodbary et al [24] aimed at effect of counter-flow species, for pressure and heat flux of body surface. Their results showed that helium gives better cooling performance at low pressures due to lower C_p than CO_2 jet. Karashima et al [25] had objective to understand the effect of jet pressure ratio on surface pressure in supersonic flows. They showed that at low pressure ratio, detached shock wave was unstable while it was stable and recompression shock wave was unstable at high jet pressure ratios. Peak pressure values were seen on body when detached shock wave was closer to model surface while it was minimum when shock wave was far away from model. Tamada et al [26] were keen to understand the effect of nose configuration and jet pressure ratio on heat and drag reduction. They found that heat flux on ogive body reduces for both supersonic and hypersonic flows with jet pressure ratio due to enhancement of recirculation region. Increasing jet pressure reduced form drag more for ogive body due to larger low pressure recirculation region and weaker recompressed shock. Attaching extended nozzle to ogive body decreased heat distribution on body with the use of opposing jet and this also lowered the drag on body. Zheng et al [27] worked for the effect of jet velocity on static temperature reduction at nose of blunt body. Their results indicated existance of thermal oscillations for both jet velocities but these oscillations were significant at lower jet velocity. Reduction in static temperature was seen near nose of body as compared to no jet case. Min et al [28] studied effect of jet pressure and jet Mach number on normal force and pitching effect of missile. They found barrel shock region becoming larger while its inclination was almost same with increase in jet pressure. Diameter of barrel shock increased with jet Mach number due to jet momentum enhancement as it was proportional to square of jet Mach number. Venukumar and Reddy [29] studied effect of injection pressure on drag reduction for nitrogen and helium supersonic opposing jets. The experimental test model used is shown in Fig 1.10(a). They noticed appreciable reduction in

drag as elucidated in Fig 1.10(b) upto injection pressure of 2 bar after which it is almost constant. Drag reduction trend for nitrogen and helium jets was identical and it became independent beyond a particular injection pressure. Bin et al [30] studied effect of jet

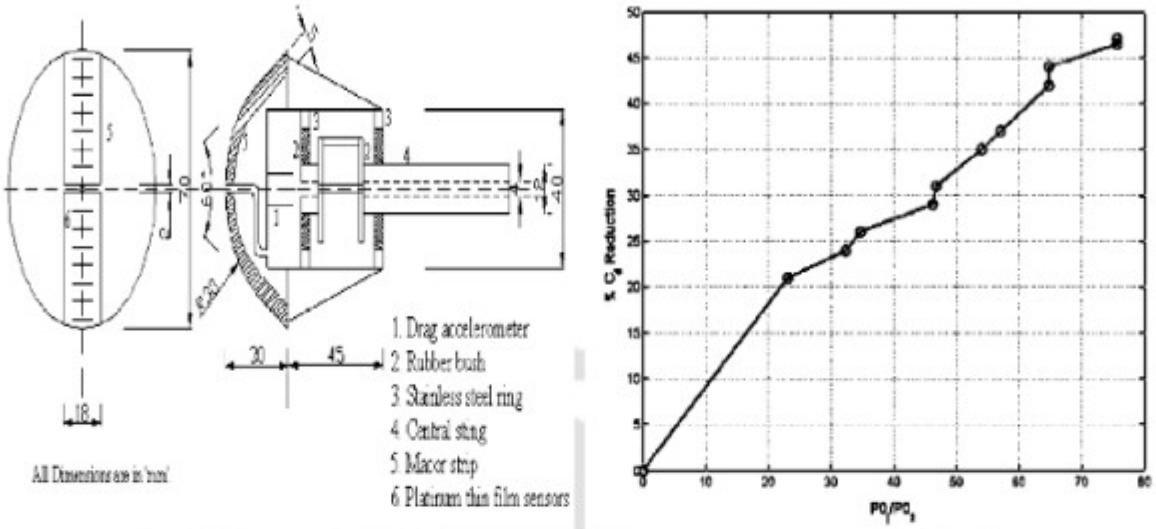

Figure 1.10: (a) Schematic diagram of experimental facility (b) Percentage drag reduction variation [29]

orifice configuration on drag reduction of blunt body. They found that pentacle shape gives best drag reduction performance as it pushes detached bow shock farthest from body due to larger penetration of jet which gives larger recirculation region, but square shape was best for both drag and heat reduction performance. Chang et al [31] focused on effect of jet and freestream Mach number on drag and heat reduction of body. They found that drag force reduces by increasing counter-flowing jet Mach number but again average heat flux rises due to enlargement of separation region. Drag and surface heating increased as compared to no-jet case for freestream Mach number of 4.96. Cheng et al [32] reported for the effect of jet mass flow rate, attack angle on surface pressure and heat flux. For low jet flow rates, pressure and heat flux on body was more than no-jet case but both reduced for higher jet flow rates. Pressure and heat flux were much higher at windward side for 10^o attack angle but both were lower for any counter-flow jet condition. Hayashi et al [33] examined effect of jet pressure ratio, jet Mach number on surface heat flux of blunt body. They found that increasing jet pressure gives more jet mass flow rate and thus enhancement of jet temperature after interaction with freestream is small which reduces temperature in recirculation region and at reattachment point and hence surface heat flux drops. Shah and Lu [34] examined effect of jet pressure ratio on drag reduction for different freestream Mach number. Bow shock oscillates between SPM and LPM for range of pressure ratio at all freestream Mach number as the jet extends along bow shock forming recirculating region which contains toroidal vortex that are dynamic

in nature. Hayashi and Aso [35] were interested in relation between the jet pressure and aerodynamic heating. They noticed that increasing jet pressure pushes bow shock away from body and Stanton number is higher for lower values of jet pressure as compared to no jet case due to unsteady flow field. Keyes and Hefner [36] examined effect of jet pressure on drag of body at zero attack angle at Mach 6. Bow shock moves away from body with increase in jet pressure and it becomes unsteady at larger jet pressure ratios. Drag on body enhances with jet pressure as compared to no-jet case. This rise is not significant at lower jet pressure but at higher jet pressures, there is sharp increment in drag on body. Stalder and Inouye [37] examined effect of jet pressure and Reynolds number of free-stream on convective heat transfer on model surface for direct tangential injection from body. They found that for direct air injection into main-stream, convective heat transfer almost doubles as the static temperature after conical shock rises due to increased injection. For tangential injection, heat transfer reduces but this reduction diminishes with increase in injection rate due to presence of local disturbances which accelerates injectant flow locally and thus reduces effectiveness of injection. Aso et al [38] experimentally studied effect of jet pressure width of injection on wall pressure and separation distance. Their results shows that wall pressure rises in front of injection slot due to flow separation and then it reduces at slot and again rises to give a local pressure peak downstream of slot. For cross-jet, surface pressure increases as separation of turbulent boundary layer moves upstream and separation region becomes large.

Researchers have also studied array of counterflowing jets for heat reduction in hypersonic flows [39]. Simulations for high speed turbulent flows are also explored [40]. Moreover alteration in drag force as well as heat flux [41] was also explored in the literature. Some investigations in the open literature accounted plasma for injection from stagnation point [42]. Among such studies, Sahoo et al [43] experimentally studied the effect of jet species on surface heat transfer and drag. They found reduction in heating near nose of the object to be higher for air injection while this reduction was higher for helium in the downstream region because it is a lighter gas. Among them, Shang et al [44] considered high temperature plasma counter-flowing jet for drag reduction. They found that drag on the object increases with temperature of injectant since the density lowers and results in reduced mass flow rate. Surface pressure was noted to be significantly lower for plasma jet injection due to dissociation of air and release of energy in the jet. Poggie [45] worked on steady and unsteady plasma actuation to control separation for Mach number of 5. Similarly, Shang et al [46] also adopted plasma actuation and observed that effectiveness of flow control increases with freestream Mach number. This plasma based flow control technique was also found suitable in reducing the drag force.

In this regard, Watanabe and Suzuki [47] studied the effectiveness of DC arc plasma discharge on hypersonic flows. They found that there is decrease in the surface pressure using plasma actuation technique and maximum reduction in drag coefficient was observed as 56%.

1.6.2 Study on drag and heat reduction by aero-spike

Spike attachment at the nose of the blunt body is also considered as a effective drag reduction technique. Numerous researchers have explored the effect of spike length, spike diameter, spike configuration on drag and heat reduction for high speed flows. Pioneering experiments was conducted by Mair [48] for spike length (L) to body diameter (D) ratio of 1.5. It was concluded that migration of separation point on the spike surface strongly contributes to conical shock shape and recirculation zone. Maull [49] experimentally investigated the influence of axisymmetric spike on flow field and drag reduction. Unsteady flow pattern was observed upto certain length of spike while this unsteadiness also depends on nose shape of the body. Fluctuating drag coefficient was noted for most of the spike lengths. Wood [50] carried out research for hypersonic flow over spiked cone-cylinder. It was noted that shape and size of separated flow depends mainly on reattachment point location. A semi-empirical relation between separation point location and spike length was suggested. Reding et al [51] attached extendible spike near the body nose and obtained reduced drag force on the body by generation of low pressure separated flow region. This flow separation also induced negative aerodynamic damping for certain flow conditions. Mikhail [52] studied numerically supersonic flow over spiked-nose configuration. Flow pattern was unsteady for low freestream Mach numbers while this unsteadiness became negligible at higher freestream Mach numbers. Milicev and Pavlovic [53] explored the effect of spike shape on drag force for various angle of attack experimentally. Results revealed that sharp spiked configuration gave weaker conical shock as compared to hemispherical tipped spike. Menezes et al [54] conducted experiments for hypersonic flow over flat tipped spike attached at the nose of body. More than 50% drag reduction was obtained for moderate angle of attack but drag increases at higher angle of attack as flow separation shock gets impinged on the windward side of the body. Gilinsky et al [55] examined effect of spike length on drag coefficient of blunt body. Multiple spikes located at center of blunt body increased drag but also enhanced lift force of body. Here, drag reduced with spike length for single-spike case. Kulkarni et al [56] investigated the influence of flat tip spike as shown in Fig 1.11(a) on drag reduction for different freestream stagnation enthalpy conditions and concluded that around 57% drag reduction was seen for given freestream stagnation enthalpy as compared to no-spike case but drag coefficient remained almost constant for various freestream stag-

nation enthalpies as depicted in Fig 1.11(b). Mehta [57] examined the effect of spike

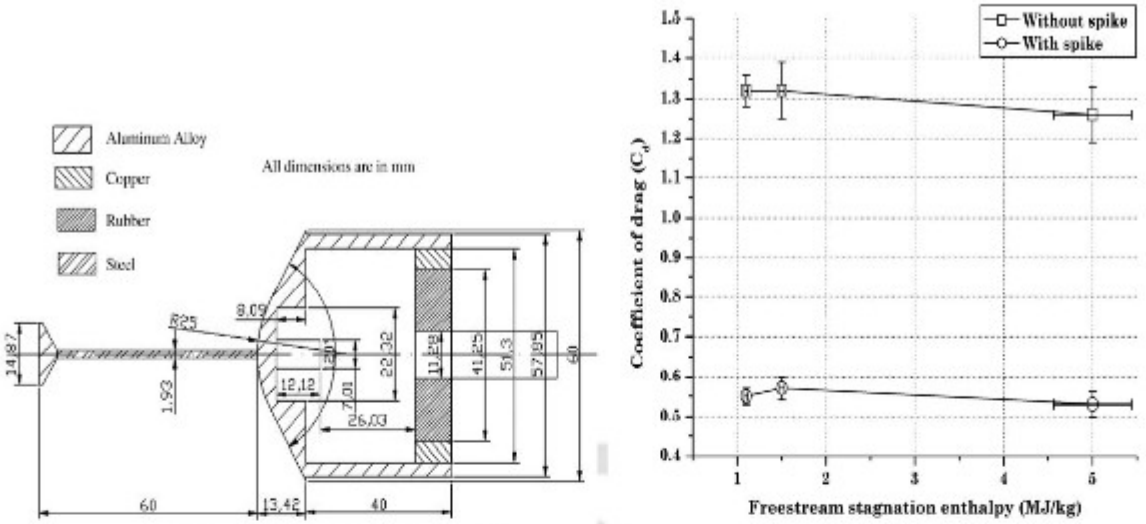

Figure 1.11: (a) Model geometry with spike (b) Drag variation with enthalpy [56]

configuration on drag and wall heat flux at zero angle of attack and freestream Mach number of 6 for L/D ratio of 0.5 numerically. Hemispherical shaped spike gave higher aerodynamic drag and wall heat flux as compared to flat faced spike. Yadav et al [58] showed the effect of spike length on drag and heat reduction for hypersonic flows. Higher wall heat and drag coefficient were observed for shorter spikes as compared to longer spikes. Mohandas et al [59] numerically studied the influence of spike tip configuration on the wave drag of the body for supersonic flows. They used $k-\omega$ turbulence model along with N-S equation and concluded that spike with large bluntness gives higher drag reduction percentage. Srinath and Reddy [60] studied the effect of plain and telescopic shaped spikes on the drag reduction. They found that the telescopic spike gives more drag reduction as compared to the plain spike. Khurana et al [61] were keen to see the effect of spike on the drag reduction for flow over a blunt body. Their results indicated that hemispherical spike with largest L/D ratio offers the best drag reduction as it forms largest separation region. Kalimuthu et al [62] were interested in effect of spike geometrical parameters on drag and pitching moment of the object. Model used with spike attached to it is shown in Fig 1.12(a). Maximum of 78% drag reduction was observed for spike L/D ratio of 2 as elucidated in Fig 1.12(b) with minor increase in pitching moment of the body. Jones et al [63] explored the influence of spike length on the wave drag of body at various freestream Mach numbers and found that spike L/D ratio of 1.5 gives minimum drag while drag reduction increases with freestream Mach number. Guy et al [64] studied the effect of spike diameter and spike semi-vertex angle on drag reduction percentage and concluded that drag on the body reduces with both these parameters for given body diameter. Dhumieres and Stollery [65] noted the effect of spike length on drag

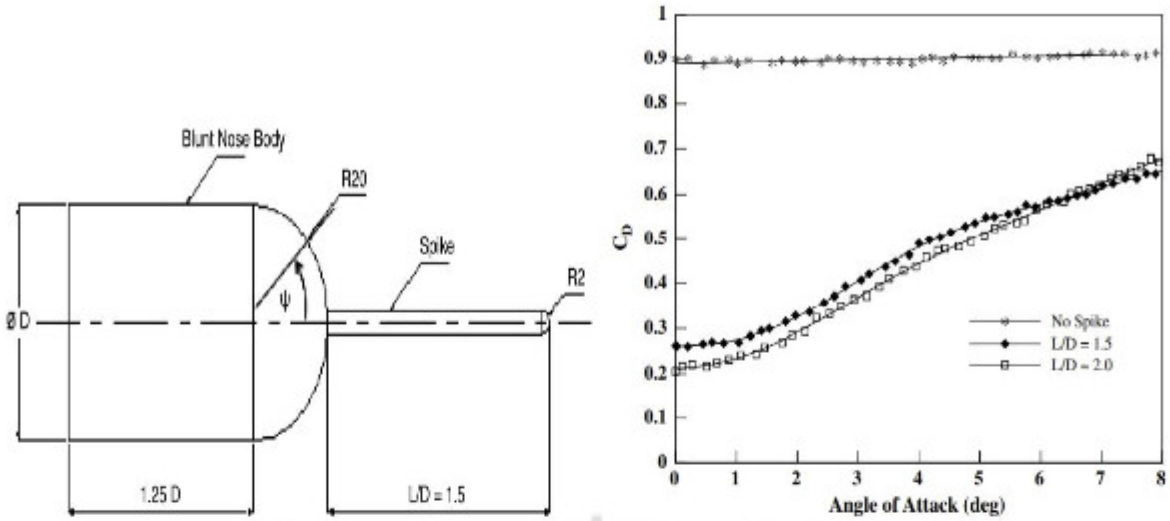

Figure 1.12: (a) Spike attached geometry (b) Drag variation [62]

over the body for high speed flows. Their results showed that shorter spike is responsible for lesser drag values while flow is steady for the range of spike length considered in the study. Gauer and Paull [66] examined the effect of spike length and spike configuration for hypersonic flows on drag reduction of the object. Spike with aerodome having L/D ratio of 2 proved to be best for drag reduction. Calculated drag reduction was obtained when their spike configuration was attached in flight on the tip of the HyCAUSE nose cone. Kumar et al [67] explored the effect of real gas on drag reduction for high enthalpy flows. They concluded that wave drag increases for higher freestream total enthalpy for no spike case but when spike is attached percentage drag reduction reduces with increase in freestream total enthalpy.

1.6.3 Review of upstream energy deposition technique

Upstream energy deposition is also an advanced and effective technique for drag reduction in high speed vehicles. Numerous researchers have explored drag reduction over various objects using steady and pulsed energy deposition [68]. Borzov et al [69] focused on effect of local energy deposition on drag for hypersonic flow over body with different nose bluntness. Their results showed that nose with large bluntness offers lesser drag on the body for given energy supply. Levin and Terenteva [70] explored supersonic flow over cone with heat release near the apex. They concluded that effective drag reduction can be obtained by concentrated energy supply as it generates freestream non-uniformity near the energy source. Levin et al [71] were interested in drag and heat reduction for supersonic flow by local energy supply. They observed the effect of intensity and size of

energy source on wall heat and drag of the body. Results revealved that significant drag reduction was achieved by using smaller size of energy source but it resulted in minor intensification of heat exchange. Vlasov et al [72] investigated the influence of local energy deposition on the flow field for both subsonic as well as supersonic flows. They obtained two different shock structures, for supersonic freestream flow, shock was attached to the energy source while it was detached for subsonic flows. They also proposed the corelation to evaluate the gas density at the center of energy source for constant and periodic energy deposition. Bracken et al [73] examined experimentally the effects of electric arc energy deposition as shown in Fig 1.13(a) on drag of the body at freestream Mach number of 10. They proved that drag force on the object reduces by the introduction of energy supply and this reduction is more significant for lower arc power. Corresponding drag signals are depicted in Fig 1.13(b). Georgievskii and Levin [74] studied the effect of

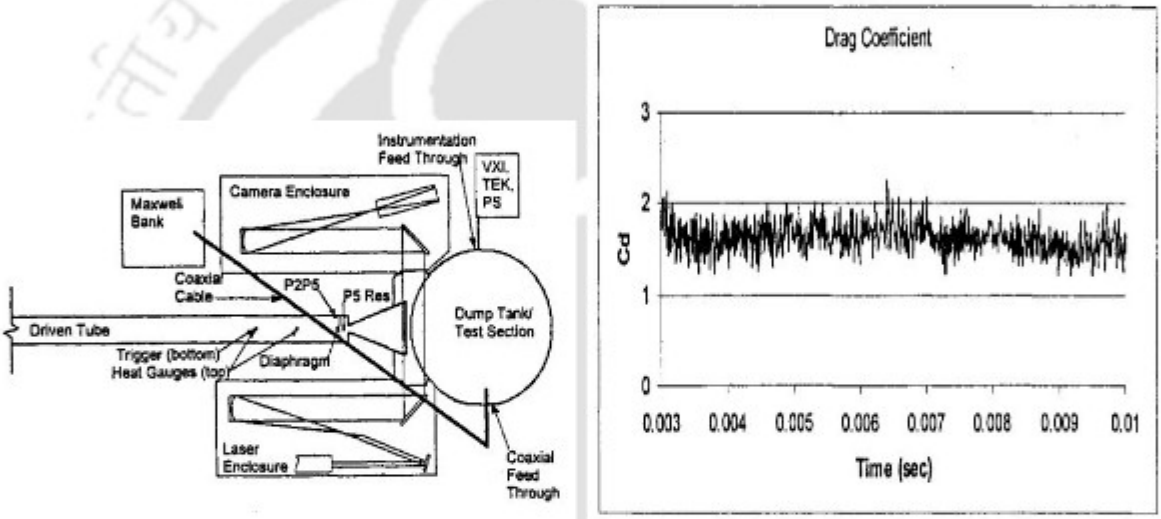

Figure 1.13: (a) Experimental test facility (b) Drag variation signals [73]

local energy supply on flow features and drag for supersonic freestream flow. Significant shock restructuring was observed as a result of energy deposition due to thin temperature wake effect in recirculation area. Appreciable drag reduction can be obtained for higher energy supply. Erdem et al [75] focused on drag reduction by steady energy deposition for freestream Mach number of 5. Local energy source was generated by the electric arc discharge and good amount of drag reduction was seen for higher frontal area of energy deposition. They suggested that, greater drag reduction can be obtained for shorter distance of energy source from the object. Gutierrez and Poggie [76] investigated effects of energy deposition on drag force of the slender body. Drag reduction upto 80% was acheived for pulsed energy deposition while significant drag reduction was obtained when the energy deposited was of the order of kinetic energy flux of the freestream flow. Kulkarni et al [77] explored experimentally aerodynamic drag reduction over blunted body for

hypersonic flows. Maximum of 47% drag reduction was seen for freestream Mach number of 8 and freestream stagnation enthalpy of 3.4 MJ/kg due to the addition of heat into shock layer. Ganesh and John [78] added concentrated energy input for drag reduction in hypersonic flows. Here, wave drag varied inversely with energy magnitude and directly with energy bubble size. Shock recasting and size of recirculation zone were strongly dependent on energy source parameters which in turn affected the wave drag of the body. Shneyder et al [79] carried out research on effect of steady and pulsed energy deposition on drag reduction of the object and concluded that flow field and drag forces gets altered significantly by pulsed energy source rather than steady energy source. Desai et al [80] examined the influence of real gas effects on drag reduction. Their results showed that consideration of real gas effects lowers percentage drag reduction. Power effectiveness of the energy supply also reduced at higher freestream stagnation enthalpy. Das et al [81] compared the amount of energy deposition required for maximum power effectiveness for earth and mars atmospheres and concluded that larger amount of concentrated energy is required in case of mars atmosphere. Higher dependence of specific heats on temperature was considered to be responsible for such observation. Further, performance of this technique was lower at higher freestream stagnation enthalpy. Georgievsky and Levin [82] studied the influence of periodic energy input on shock wave structure for supersonic flows. It was observed that by the elongation of energy source, transition of shock wave from pulsing regime to quasi-stationary occurs and this could be one of the effective methods to control the shock wave structure for high speed flows. Tahsini [83] studied heat release effects on drag reduction in high speed flows. Body surface was coated with 10 μm chromium layer which would release energy at high temperatures. Centreline temperature remained constant on surface due to chromium melting and it jumped due to exothermic reactions at Mach disk. Melting of chromium layer increased shock stand-off distance which in turn reduced drag on body. Zaidi et al [84] were interested in influence of pulsed energy deposition on flow field and shock wave structure. Energy pulse was generated by laser and they observed that there is significant alterations in flow features and corresponding shock wave structure when the energy source is moved towards the body. Ogino et al [85] showed the interaction between upstream deposited energy and shock structure. Drag reduction was also noted for supersonic flow around a sphere. Amount of energy deposited reduced drag significantly while energy source location had lesser impact on drag reduction. Sangtabi et al [86] conducted numerical simulations for unsteady laser energy deposition and observed its effect on flow field. Effect of Mach number, location of energy deposition, number of laser pulses and the frequency of energy deposition on drag reduction were studied and concluded that drag reduction duration increases with number of energy pulses and frequency while the duration of drag reduc-

tion reduces with freestream Mach number and location of deposited energy. Kandala and Candler [87] explored the effect of energy deposition on shock structure and surface pressure for reacting high speed flows. Their results indicated that delayed release of chemical energy sustains the effect of energy deposition while there is greater surface pressure decrement for reacting flows as compared to perfect gas flow. Zheltovodov et al [88] analysed the influence of laser induced energy deposition on flow features and wave drag reduction of the body. Location and frequency of energy source significantly altered the wave drag while unsteady energy deposition gave better drag reduction as compared to steady energy deposition.

1.6.4 Review on cavity based studies

Saravanan et al [89] studied effect of cavity on heat transfer rates over missile shaped object for various angles of attack. Significant reduction in surface temperature and surface convective heating rates were seen due to formation of recirculation region inside the cavity. Maximum of 27% reduction in heating rates were observed near tip of cavity and it is only marginally affected at other locations. Schlieren images and their corresponding Stanton number distribution are shown in Fig 1.14(a) and Fig 1.14(b) respectively. Xiao et al [90] studied experimentally shock iteraction of blunt body with forward facing

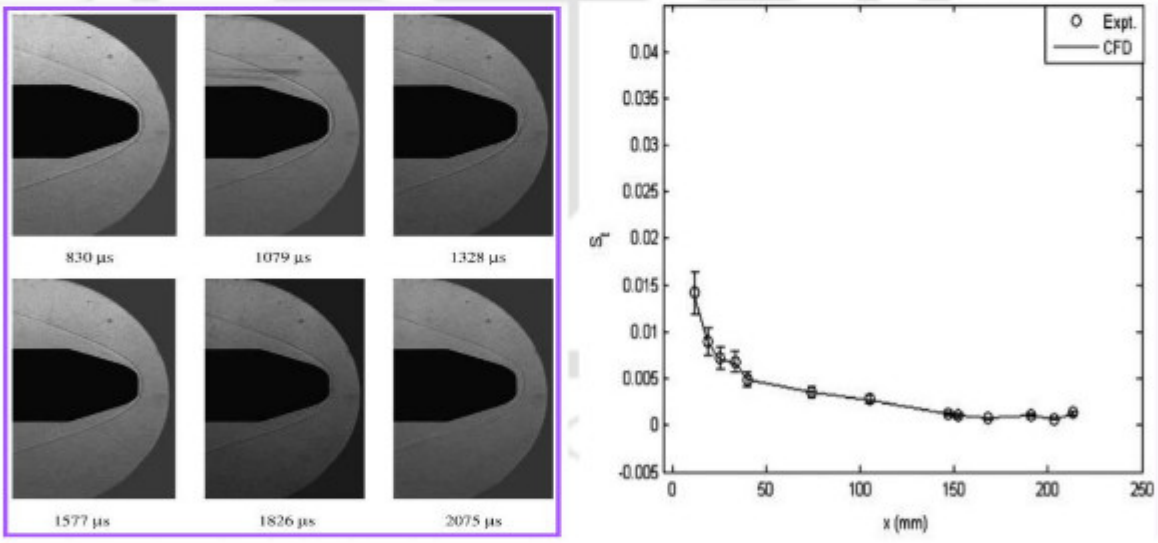

Figure 1.14: (a) Schlieren images (b) Stanton number variation [89]

cavity. They observed two different oscillation modes of the shock namely high frequency forward-backward oscillation and low frequency up-down oscillation. Also, with increase in cylinder length-to-diameter ratio, frequency of shock oscillation reduced significantly. Shock wave oscillation mainly depends on interference between freestream flow and cav-

ity. Silton and Goldstein [91] investigated the effect of cavity length, cavity lip radius and diameter of cavity on the heat flux reduction. They concluded that least heat flux was obtained when the cavity length was four times the cavity diameter for given nose radius. Cavity diameter has least impact on heat flux for given cavity lip radius. Introduction of forward facing cavity delays the onset of ablation without enhancing drag. Mohri and Hillier [92] examined the effect of rectangular shaped cavity on surface pressure for laminar and turbulent flow regimes. They found that periodic fluctuations are present at the front corner of the L/D=1.33 cavity. Time-averaged surface pressure matched well with the computational results.

1.6.5 Review on drag and heat reduction by combination techniques

Zhu et al [93] investigated the effect of spike with combination of multi-jet on drag and heat reduction. They used stainless steel blunt body and found that drag and surface heat flux reduce by increasing jet pressure ratio as bow shock wave gets pushed further away from body and size of recirculation zone increases. Good heat and drag reduction was found when lateral jet was located away from body. Lower heat flux was obtained for shorter spike but it gave high surface pressure so a compromise should be made for optimum spike length. Shang et al [94] examined the effect of jet-spike combination in high speed flows. They concluded that maximum drag reduction can be achieved at critical pressure of jet where flow field changes from unsteady to steady as jet showed maximum penetration into shock layer. Unsteady oscillations were seen for low jet pressure and surface pressure reduces near face of body whereas it was almost same at shoulder of body. Huang et al [95] studied drag reduction by combination of jet and spike for supersonic flows. They concluded that drag on body reduces with increase in length of spike or with increase in jet pressure due to increase in recirculation zone formed between jet layer and spike but increasing spike length has more impact on drag reduction than jet pressure. Location of peak pressure also moved downstream with the increase in length of spike. Jiang et al [96] experimented for the effect of lateral jet on surface pressure of body. They found that introduction of lateral jet near spike tip pushed oblique shock away from spike and oblique shock interacted with reattachment shock more away from body as compared to no-jet case which gave lower surface pressure on body. Introduction of spike became ineffective for non-zero attack angle as peak pressure on body surface crossed the stagnation pressure. Huang et al [97] studied the combined effect of jet and cavity on heat flux reduction for supersonic flows. They concluded that value of peak heat flux can be reduced for shorter cavity and as jet pressure increases heat flux on surface reduces due to enlargement of recirculation zone. Lighter injectant gave lower heat

flux on body surface. Haibo et al [98] focused on the effect of combination of cavity and opposing jet on drag and heat reduction. With increase in jet pressure drag was found to be lowered as the reattachment point moved further downstream on body surface due to larger recirculation zone. Stanton number was found to be reduced with increase in jet pressure as hot freestream gases doesn't come in direct contact with major part of body surface. It was also mentioned that, jet flow can be saved when acceptable heating is desired with the use of cavity alone. Sun et al [99] examined the effect of cavity and jet combination on drag and heat flux for hypersonic flows. They found that heat flux for parabolic configuration cavity was higher than conventional shape but pressure values were lower for low values of jet pressure. Lighter gases gave lower drag and heat flux on body surface and gases with similar molecular weight and thermodynamic properties replaced each other as they gave similar pressure distribution on body. Smaller jet orifice offered better heat and drag reduction. Haung et al [100] studied effect of combination of cavity and jet on drag and heat reduction for hypersonic vehicles. They concluded that when cavity is located near the nose of body, pressure and heat flux on body are lower due to formation of smaller recirculation zone near Mach disk. In their studies, injectant with smaller molecular weight gave smaller drag and heat flux on body surface. Ou et al [101] studied drag and heat reduction by combination of spike and opposing jet in hypersonic flows. They found that Lower jet dia. has negative effect on drag and heat reduction while for higher jet dia. drag reduces with increasing jet pressure. Increasing spike length reduces surface pressure and heat flux but this reduction is smaller for higher spike length. Sun et al [102] observed drag and heat reduction induced by combination of cavity and opposing jet in hypersonic flows for conventional and parabolic cavity configuration. Effect of different turbulence models was examined. They concluded that SST $k-\omega$ model was more suitable and combination technique of parabolic configuration of cavity and jet was more effective in pushing the shock away from body resulting in reduction in peak values of surface pressure and Stanton number due to better expansion of jet which avoids total pressure loss of the jet. Lu and Liu [103] noted effect of combination of cavity and opposing jet on drag and surface heat flux. They found that Stanton number reduces with the introduction of cavity and it is further reduced when the opposing jet is turned on. Jet pressure ratio also controls the cooling performance of the combination technique.

1.6.6 Development of fluid flow solver

Dependence of specific heats and flow parameters on temperature were introduced by Moore [104]. Later, theory for stagnation point heat transfer in high speed reacting flows was proposed by Fay and Riddell [105]. Then, stagnation point heat transfer

in dissociated air was given by Rose and Stark [106] and Rose and Stankevics [107]. Further, ionization along with the dissociation reaction was introduced by Fenster [108] for stagnation point heat flux. Conti and Dyke [109] considered effect of flow properties on drag for inviscid flow incorporating variable reaction rates. Later, UPWIND algorithm was proposed by Liu and Vinokur [110] for general non-equilibrium flows. Further, newly flux splitting scheme was developed by Grossman and Cinnella [111] for thermal and chemical non-equilibrium flows. Then, second order upwind scheme was developed and used by Netterfield [112] for the calculation of convective fluxes in high speed reacting flows. Later, Park [113] studied two temperature model incorporating translational and vibrational energy of air molecules. Again, Park [114] considered non-equilibrium flows and concluded that significant drag variation was observed by considering temperature dependent flow properties. Higher order reacting flow solver was proposed by Sawley and Wuthrich [115]. Sabetta et al [116] incorporated various temperature dependent reactions for high speed flows and observed that considerable alterations were seen in the flow features for non-equilibrium flows as compared to equilibrium flows.

1.7 Objectives of the current study

From the literature it is evident that the major governing parameters considered by the researchers while understanding the performance of counter-flowing sonic or supersonic jets are injection pressure ratio, opposing jet species, jet diameter and jet Mach number. Similarly, spike dimensions and shapes were studied and their effects are reported in the literature for the spike based drag reduction technique. Alteration of drag or surface heat flux should be expected with alteration in these parameters. Since both techniques are constitutionally different, they have different performance parameters. Hence it is not possible to compare their effectiveness or performance for same freestream conditions with the help of existing performance estimation parameters like percentage drag reduction. Further, it needs to account multiple and mixed governing parameters while working with jet and spike combination for drag reduction. This fact demands a common performance parameter to be thought for, which is based upon elementary underlying principles. Exergy is such a fundamental quantity and percentage exergy destruction is a standard performance parameter adopted for various flow processes. It should be noted that, exergy destruction has never been considered as a tool for the analysis of drag reduction techniques. Therfore percentage exergy destruction is considered herein for the first time to examine the drag reduction techniques for their performance and to compare various drag reduction techniques. Further, most of the computational studies for spike or jet based drag reduction assume perfect gas flow. Hence the current inves-

tigation is centered on the real gas effects while considering exergy destruction from the computational results obtained using reacting solver.

It can be noted from the literature that various parameters like injection pressure ratio, injection gas, jet to base area ratio are studied by the researchers while understanding the performance of counter flowing jets. Most of these computational or experimental studies are conducted at lower total temperature conditions of the freestream flow. Hence the current investigations are performed to explore real gas effects for the accurate solution of the flow field and better prediction of drag reduction for low as well as high enthalpy flows. Such study is expected to reveal the effect of various freestream and jet flow parameters on wall pressure, wall heat flux and wave drag in the presence of reacting hypersonic flow over the hemisphere with counter flow injection from stagnation point. Initially, flow features like shock stand-off distance, Mach disk parameters are analysed for sonic injection for the perfect gas assumption. Then the real gas flow solver is employed to assess the alteration in these flow features in the presence of real gas effects.

Open literature suggests that researchers have performed computations and experiments to achieve better reduction in drag force and surface heat load with counter-jet injection. Specifically most of the computations dealt with freestream and jet parameters separately for their influence on the performance. Researchers carried out simulations for drag reduction with opposing jet technique and a new parameter R_{PA} was introduced which is the combinination of jet pressure ratio and area ratio. Same wave drag coefficient can be obtained with same R_{PA}. So it was proposed to represent the intensity of opposing jet and access it's performance on flow field and drag foces. Influence of momentum ratio (ratio of jet momentum to the freestream momentum) on counterflowing jet based drag reduction technique was also examined for supersonic flows. It was proved that momentum ratio has a vital role in shock restructring and hence drag reduction for wide range of freestream and jet parameters. It was recommended that momentum ratio was a unique governing parameter for counter flow injection technique. However this universal parameter was tesed only for supersonic flows. Moreover it is also desirable to understand it's universality in the presence of real gas effects. Therfore in the current study, thermodynamic analysis of the opposing jet based drag reduction technique is carried out considering real gas effects at elevated freestream stagnation enthalpy. In this context, hypersonic flow over hemispherical object is considered and the effect of momentum ratio is analysed by altering various governing parameters. Results are analysed for the wave drag, entropy generation rate and exergy destruction.

It is evident from the given literature that most of the computational studies for opposing jet or combination of jet and cavity based drag reduction technique are conducted with perfect gas assumption. Hence the current investigation is centered on the real gas effects on the flow field alterations and surface pressure distribution obtained from the computational results for the combination technique of opposing jet and forward facing cavity. Further, the effect of gas reactions is also observed on drag force and newly proposed thermodynamic parameter named entropy generation rate which can be used as a tool along with coefficient of drag to access the performance of opposing jet, forward facing cavity and combination of jet with cavity techniques.

Based on the above discussion, following objectives are described set for the current investigations.

1. Development of an unstructured Navier-Stokes non-equilibrium compressible flow solver based on finite volume method which includes five species and eleven elementary chemical reactions of atmospheric air.
2. Validation of the current solver with available experimental literature test cases for two-dimensional axi-symmetric flows.
3. Comparison of active and passive drag reduction techniques based on newly proposed thermodynamic parameter named exergy destruction.
4. Analysing the influence of elevated stagnation enthalpy hypersonic flows on surface heat flux and wave drag of the object.
5. Thermodynamic analysis of opposing jet drag reduction technique for various freestream and jet conditions.
6. Understanding flow field and associated drag variations for opposing jet and cavity combinatorial technique considering real gas effects.

1.8 Organisation of thesis

The thesis is arranged in following chapters:-

Chapter 1 discusses about introduction of hypersonic flows, various reacting flow models used to study such flows and different drag reduction techniques. It also presents literature review for all these techniques.

Chapter 2 deals with mathematical formulation of the in-house developed non-equilibrium and perfect compressible flow solvers. It also explains simulation methodol-

ogy used to carry out present studies.

Chapter 3 presents exergy destruction and drag reduction analysis of active and passive techniques. Various active and passive techniques are compared based on common parameter named exergy destruction.

Chapter 4 deals with analysis of counter flow injection technique at elevated enthalpy hypersonic reacting flows. Effect of various freestream and jet flow parameters on wall pressure, wall heat flux and wave drag in the presence of reacting hypersonic flow over the hemisphere with counter flow injection from stagnation point are explained in details.

Chapter 5 explains thermodynamic and drag force analysis for opposing jet technique in hypersonic reacting flows. Effects of various flow and geometrical parameters of freestream and jet on flow field and associated drag reduction is studied.

Chapter 6 describes drag and entropy generation analysis for opposing jet and forward facing cavity combinatorial technique in presence of real gas reactions. Effects of reacting flow is examined on flow field, entropy generation rate and surface properties for jet and cavity combinatorial technique.

Chapter 7 provides useful conclusions drawn from the current analysis and future scope of the present work.

CHAPTER 2

NUMERICAL METHODOLOGY

This chapter describes the numerical methods used to investigate the low and high enthalpy compressible reacting flows. Cell-centred finite volume formulation is employed for discretization of basic governing equations and the same is explained in the current chapter. The scheme to calculate viscous and convective fluxes and the incorporation of different boundary conditions are also part of this chapter. Further, full details of temporal discretization method along with source term implicit discretization procedure are also mentioned. Then, various gas models considered for computational investigations are presented in this chapter.

2.1 Governing equations

Computational Fluid Dynamics (CFD) is a modern tool to solve the basic conservation equations for various fluid flow problems using suitable numerical algorithm. It is relatively cheap way to analyse different compressible flows as compared to expensive experimental methods. Many researchers now-a-days are using CFD method to solve various problems for efficient design of high speed aircraft so that they can be operated at its optimum condition for long duration of time. For the simulations at low enthalpy flows, Navier-stokes equation is solved with mass conservation and energy conservation equations but during high enthalpy flows, species continuity equations must be solved simultaneously for the accurate solution of flow field. All the basic governing equations coupled with species continuity equations for laminar viscous two-dimensional axisymmetric compressible flows are given as follows:

$$\frac{\partial X}{\partial t} + \frac{\partial E_I}{\partial x} + \frac{\partial F_I}{\partial y} + \alpha(G_I - G_v) - S = \frac{\partial E_v}{\partial x} + \frac{\partial F_v}{\partial y} \tag{2.1}$$

Here, X is the conservative variables vector, E_I and F_I are the convective/inviscid fluxes in x and y direction respectively, α is constant which is one for axisymmetric cases and zero for the non-axisymmetric cases and G_I is source term incorporated for the inviscid cases. Further, E_v and F_v are the viscous fluxes in the x and y directions and G_v is the source term considered for the viscous cases. Consideration of non-equilibrium effect introduces an extra source term which is represented as S. These terms are given as follows,

$$X = \begin{bmatrix} \rho \\ \rho u \\ \rho v \\ \rho E \\ m_1 \\ m_2 \\ . \\ . \\ m_{N-1} \end{bmatrix}, E_I = \begin{bmatrix} \rho u \\ \rho u^2 + p \\ \rho uv \\ (\rho E + p)u \\ m_1 u \\ m_2 u \\ . \\ . \\ m_{N-1} u \end{bmatrix},$$

$$F_I = \begin{bmatrix} \rho v \\ \rho uv \\ \rho v^2 + p \\ (\rho E + p)v \\ m_1 v \\ m_2 v \\ . \\ . \\ m_{N-1} v \end{bmatrix}, E_v = \begin{bmatrix} 0 \\ \tau_{11} \\ \tau_{12} \\ \sigma_x \\ -m_1 u_{d1} \\ -m_2 u_{d2} \\ . \\ . \\ -m_{N-1} u_{dN-1} \end{bmatrix}$$

$$F_v = \begin{bmatrix} 0 \\ \tau_{12} \\ \tau_{22} \\ \sigma_y \\ -m_1 v_{d1} \\ -m_2 v_{d2} \\ . \\ . \\ -m_{N-1} v_{dN-1} \end{bmatrix}, G_I = \frac{1}{y} \begin{bmatrix} \rho v \\ \rho uv \\ \rho v^2 \\ (\rho E + p)v \\ v m_1 \\ v m_2 \\ . \\ . \\ v m_{N-1} \end{bmatrix}$$

$$G_v = \frac{1}{y}\begin{bmatrix} 0 \\ \tau_{12} - \frac{2}{3}y\frac{\partial(\mu v/y)}{\partial x} \\ \tau_{22} - \tau_{33} - \frac{2}{3}\mu\left(\frac{v}{y}\right) - \frac{2}{3}y\frac{\partial(\mu v/y)}{\partial y} \\ \sigma_y - \frac{2}{3}\mu\frac{v^2}{y} - \frac{2}{3}y\frac{\partial(\mu v^2/y)}{\partial y} - \frac{2}{3}y\frac{\partial(\mu uv/y)}{\partial x} \\ -m_1 v_{d1} \\ -m_2 v_{d2} \\ . \\ . \\ -m_{N-1} v_{dN-1} \end{bmatrix}, S = \begin{bmatrix} 0 \\ 0 \\ 0 \\ 0 \\ S_1 \\ S_2 \\ . \\ . \\ S_{N-1} \end{bmatrix}$$

Here $\sigma_x = u\tau_{11} + v\tau_{12} + k\frac{\partial T}{\partial x} - \sum_{i=1}^{N} h_i m_i u_{di}$ and $\sigma_y = u\tau_{12} + v\tau_{22} + k\frac{\partial T}{\partial y} - \sum_{i=1}^{N} h_i m_i v_{di}$. The terms h_i is the molar specific enthalpy of i^{th} species. Here, the state variables are density (ρ), pressure (p), temperature (T), total internal energy (E) and internal energy (e). $E = e + \frac{1}{2}(u^2 + v^2)$ where $e = \sum_{i=1}^{N} e_i \frac{C_i}{\rho MW_i}$ and $e_i = h^0_{fi} + \int_{T_R}^{T} C_{pi} dT - R_u T$ where i represents i^{th} species.

Pressure is taken as sum of partial pressures of each species as calculated from following equation.

$$p = R_u T \sum_{i=1}^{N} \frac{m_i}{MW_i} \tag{2.2}$$

Temperature is obtained from total energy iteratively using Newton-Raphson method by following equation.

$$\rho e = \sum_{i=1}^{N} [\frac{m_i}{MW_i} \int_{T_R}^{T} C_{pi} dT + h^o_{fi}] - p \tag{2.3}$$

Components of shear stress ($\tau_{11}, \tau_{12}, \tau_{22}, \tau_{33}$) are calculated as [117].

$$\tau_{11} = \mu(\frac{4}{3}\frac{\partial u}{\partial x} - \frac{2}{3}\frac{\partial v}{\partial y}), \tau_{12} = \mu(\frac{\partial u}{\partial y} + \frac{\partial v}{\partial x}), \tau_{22} = \mu(\frac{4}{3}\frac{\partial v}{\partial y} - \frac{2}{3}\frac{\partial u}{\partial x}), \tau_{33} = \mu(-\frac{2}{3}(\frac{\partial u}{\partial y} + \frac{\partial v}{\partial x}) + \frac{4}{3}\frac{v}{y}) \tag{2.4}$$

Here, m_i, MW_i, h^0_{fi} and C_{pi} are the mass concentration, molecular weight, heat of formation and molar specific heat at constant pressure for given species i respectively. Reference temperature (T_R) is considered as 298.5 K.

In the current work, dynamic viscosity (μ), conductivity (k), and specific heats (C_p, C_v) are taken as the expression of polynomial fit of temperature as given in the literature Gordan and McBridge [118]. Heat flux has two components namely q_x and q_y, as mentioned in column E_v and F_v, are calculated by the expression given by $k\frac{\partial T}{\partial x}$ and $k\frac{\partial T}{\partial y}$ respectively. The mass diffusion velocity in x direction (u_{di}) and in y direction (v_{di}) are

calculated from Fick's law as

$$u_{di} = -\frac{D_m}{Y_i}\frac{\partial Y_i}{\partial x}, v_{di} = -\frac{D_m}{Y_i}\frac{\partial Y_i}{\partial y} \tag{2.5}$$

Here, Diffusion coefficient (D_m) is taken as $5 \times 10^{-5} m^2/s$ which is constant for all species and Y_i is the mass fraction of the i_{th} species. As the diffusion coefficient depends on the species size but the value of diffusion coefficient of N_2 species is $5 \times 10^{-5} m^2/s$ which is considered as the diffusion coefficient of the air because N_2 is the major component of air as it is present in large amount. This assumption reduces computational time and complexity of the study. Same assumption was also considered by [67] for high speed flow over spiked configuration.

2.2 Chemical reactions

A set of elementary reversible reactions involving N species can be represented as,

$$\sum_{j=1}^{N} d'_{ij} n_j \rightleftharpoons \sum_{j=1}^{N} d''_{ij} n_j \tag{2.6}$$

where $n_j = \frac{m_j}{MW_j}$
The chemical reactions shown in the source term (S) is represented in eq2.7.

$$S_j = MW_j \sum_{i=1}^{N_R} \left[\left(d''_{ij} - d'_{ij} \right) \left(k_{fi} \prod_{l=1}^{N} n_l^{d'_{il}} - k_{bi} \prod_{l=1}^{N} n_l^{d''_{il}} \right) \right] \tag{2.7}$$

Here, N_R is number of reactions, d'_{ij} and d''_{ij} are the stoichiometric coefficients for species j, where j^{th} component appears as a reactant in the i^{th} forward and backward reactions respectively and n_j is the molar concentration for species j. Further, k_{fi} and k_{bi} are the forward and backward reaction rate constants evaluated using the Arrhenius rate expression

$$k_i = B_i T^m e^{\frac{-A_i}{R_u T}} \tag{2.8}$$

where A_i represents the activation energy, B_i and m are constants. These reaction rates are dependent on temperature and are calculated as given in literature (Shuen et al [119]).

The reactions and its corresponding rate constants are given in Table 2.1

Table 2.1: Chemical reactions and specific reaction-rate constants in the chemical non-equilibrium calculations

No.	Forward reaction	k_{fi} (cm^3/mole sec)	k_{bi} (cm^3/mole sec)
1	$O_2 + M -> 2O + M(N)$	$3.6 \times 10^{18} T^{-1.0} e^{-5.95\times10^4/T}$	$3.0 \times 10^{15} T^{-0.5}$
2	$N_2 + M -> 2N + M(O)$	$1.9 \times 10^{17} T^{-0.5} e^{-1.13\times10^5/T}$	$1.1 \times 10^{16} T^{-0.5}$
3	$NO + M -> N + O + M(O_2)$	$3.9 \times 10^{20} T^{-1.5} e^{-7.55\times10^4/T}$	$1 \times 10^{20} T^{-1.5}$
4	$O + NO -> N + O_2$	$3.2 \times 10^{9} T^{1} e^{-1.97\times10^4/T}$	$1.3\times10^{10} T^{1.0} e^{-3.58\times10^3/T}$
5	$O + N_2 -> N + NO$	$7.0 \times 10^{13} e^{-3.8\times10^4/T}$	1.56×10^{3}
6	$N + N_2 -> N + N + N$	$4.085 \times 10^{22} T^{-1.5} e^{-1.13\times10^5/T}$	$2.27 \times 10^{21} T^{-1.5}$
7	$O_2 + O -> 2O + O$	$9.0 \times 10^{19} T^{-1.0} e^{-5.95\times10^4/T}$	$7.5 \times 10^{16} T^{-0.5}$
8	$O_2 + O_2 -> 2O + O_2$	$3.24 \times 10^{19} T^{-1.0} e^{-5.95\times10^4/T}$	$2.7 \times 10^{16} T^{-0.5}$
9	$O_2 + N_2 -> 2O + N_2$	$7.2 \times 10^{18} T^{-1.0} e^{-5.95\times10^4/T}$	$6 \times 10^{15} T^{-0.5}$
10	$N_2 + N_2 -> 2N + N_2$	$4.7 \times 10^{18} T^{-0.5} e^{-1.13\times10^5/T}$	$2.72 \times 10^{16} T^{-0.5}$
11	$NO + M -> N + O + M(O)$	$7.8 \times 10^{22} T^{-1.5} e^{-7.55\times10^4/T}$	$2.0 \times 10^{20} T^{-1.5}$

2.3 Finite volume method

Finite volume method is a discretization technique as shown in Fig 2.1. Here computational domain is divided into a number of sub domain called control volume with a finite number of grid points). Then various numerical schemes are applied to accurately solve the Navier-stokes equation and other conservation equations in each control volume. All governing equations are integrated over each control volume in order to solve the whole flow field.

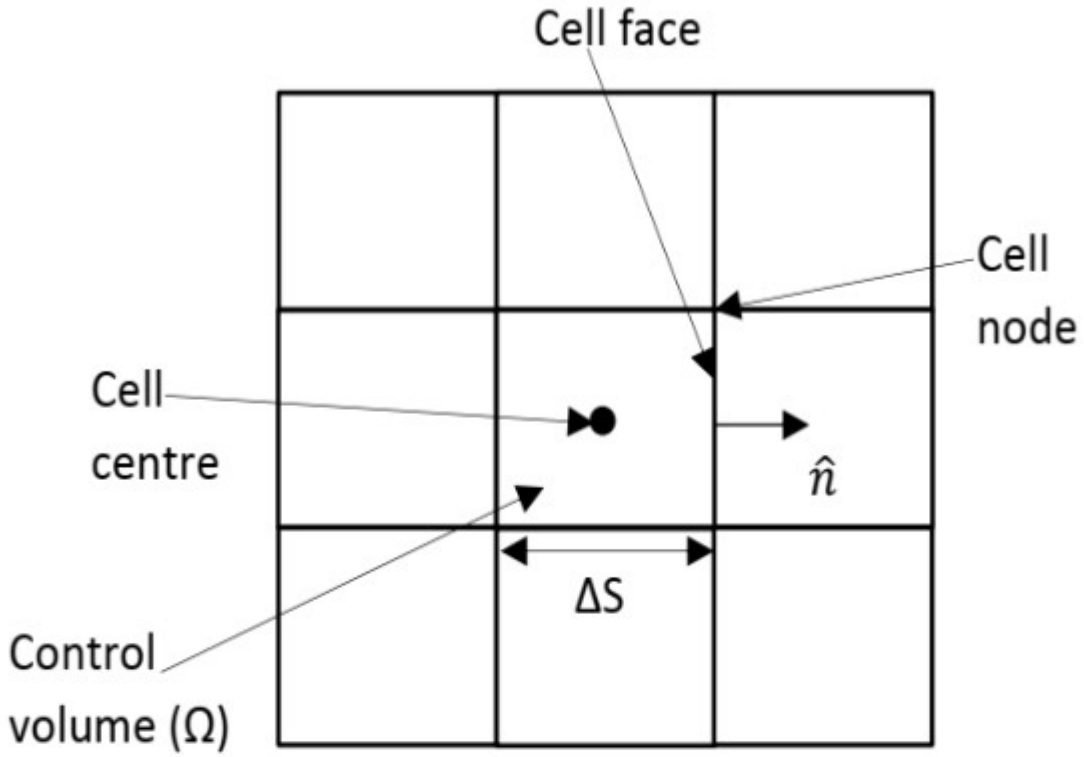

Figure 2.1: Diagram of Cell centred FVM scheme

2.4 Theoretical formulation of cell centered FVM

The governing equations for reacting flow as mentioned in Eq 2.1 can be re-written as,

$$\frac{\partial X}{\partial t} = -[\frac{\partial(E_I - E_v)}{\partial x} + \frac{\partial(F_I - F_v)}{\partial y} + \alpha(G_I - G_v) - S] \tag{2.9}$$

Integrating the above equation,

$$\int_\Omega \frac{\partial X}{\partial t} d\Omega = -\int_\Omega [\frac{\partial(E_I - E_v)}{\partial x} + \frac{\partial(F_I - F_v)}{\partial y} + \alpha(G_I - G_v) - S] d\Omega \tag{2.10}$$

Considering the left hand side of Eq 2.10,

$$LHS = \frac{\partial}{\partial t}\int_\Omega X d\Omega = \frac{d}{dt}(\bar{X}\Omega) = \Omega\frac{d}{dt}\bar{X} \tag{2.11}$$

Here, $\bar{X} = \frac{\int_\Omega X d\Omega}{\int_\Omega d\Omega}$

Considering the right hand side of Eq 2.10,

$$RHS = \int_\Omega [\frac{\partial(E_I - E_v)}{\partial x} + \frac{\partial(F_I - F_v)}{\partial y} + \alpha(G_I - G_v) - S] d\Omega \tag{2.12}$$

Re-writing the above equation in divergence form,

$$RHS = \int_{\Omega}[\nabla \cdot (H_I - H_v) + \alpha(G_I - G_v) - S]d\Omega \tag{2.13}$$

Here, $H_I = [E_I F_I], H_v = [E_v F_v], \nabla = [\frac{\partial}{\partial x}\frac{\partial}{\partial y}]$

Applying gauss-divergence theorem, we get

$$\int_{\Omega} \nabla \cdot (H_I - H_v)d\Omega = \int_{s}(H_I - H_v) \cdot \vec{n}ds \tag{2.14}$$

$$\int_{s}(H_I - H_v) \cdot \vec{n}ds = \sum_{J=1}^{n_f}(H_I - H_v) \cdot \vec{n}\Delta S_J = \sum_{J=1}^{n_f}(H_{I\perp} - H_{v\perp})\Delta S_J \tag{2.15}$$

Here, $\vec{n} = [n_x n_y]$

Where, $\vec{n}$ is the unit normal vector pointing outward of the face of given control volume. n_x and n_y are the x and y direction components of the $\vec{n}$. Here, ΔS_J is taken as the length of the face of control volume while $H_{I\perp}$ and $H_{v\perp}$ are the inviscid and viscous normal fluxes crossing the faces of control volume. These terms can be represented as:

$$H_{I\perp} = \begin{bmatrix} \rho u_\perp \\ \rho u u_\perp + p n_x \\ \rho v u_\perp + p n_y \\ (\rho E + p)u_\perp \\ m_1 u_\perp \\ m_2 u_\perp \\ . \\ . \\ m_{N-1} u_\perp \end{bmatrix}, H_{v\perp} = \begin{bmatrix} 0 \\ \tau_{11} n_x + \tau_{12} n_y \\ \tau_{12} n_x + \tau_{22} n_y \\ \sigma_x n_x + \sigma_y n_y \\ 0 \\ 0 \\ . \\ . \\ 0 \end{bmatrix} \tag{2.16}$$

The contravariant velocity ($u_\perp$) can be written as,

$$u_\perp = u n_x + v n_y \tag{2.17}$$

The source terms in the Eq 2.12 can be treated as,

$$\int_{\Omega}[\alpha(G_I - G_v) - S]d\Omega = \alpha\Omega\bar{G} - \Omega\bar{S} \tag{2.18}$$

Here, $\bar{G} = \bar{G}_I - \bar{G}_V$

Hence, the final integral form of governing equation becomes,

$$\Omega_i \frac{d\bar{X}_i}{dt} + \sum_{J=1}^{n_f} (H_{I\perp} - H_{v\perp}) \Delta S_J + \Omega_i \bar{S}_i + \alpha \Omega_i \bar{G}_i = 0 \tag{2.19}$$

$$\frac{d\bar{X}_i}{dt} = -\frac{1}{\Omega_i} \sum_{J=1}^{n_f} (H_{I\perp} - H_{v\perp}) \Delta S_J - \bar{S}_i - \alpha \bar{G}_i = R(\bar{X}_i) \tag{2.20}$$

2.5 Spatial discretization

Thus, we arrive at the semi-desretized form of the reacting comppressible flow solver equations as represented in Eq 2.20. This equation requires solution of residual term R(X_i). This can be acheived by evaluating the inviscid and viscous fluxes at the face of the each control volume. The accuracy of present solver mainly depends on the flux computation scheme. Different flux computation schemes included in the present solver are explained in the following subsections.

2.5.1 Inviscid flux computational scheme

Present discretized equations are non-linear and hyperbolic in nature. Thus, the flux calculation schemes should have good accuracy to capture the correct flow properties in the flow field. In the current finite volume cell centered discretization, inviscid fluxes are calculated using various highly accurate schemes and the formulation of each scheme used in current work is given in the Appendix. The schemes for flux computation chosen here are Van Leer [120], AUSM [121], AUSM+ [122] and Rusanov [123]. Incorporating various chemical reactions leads to alterations of mass concentration of various species during flow. Thus, given schemes take into account these alterations for both reacting as well as perfect gas flows.

2.5.2 Solution reconstruction for spatial accuracy

The flow variables need to be assigned on right and left sides of the faces of control volume for flux calculation in the upwind scheme. To obtain first order spatial accurate solution, these flow variables values are assigned by simply providing left and right side flow quantities of the face. But, first order accurate solution may lead to unphysical results which may give incorrect shock structure and flow features. Thus, higher order spatial discretization is the requirement to improve the accuracy of the solutions. Herein, second-order accurate results are obtained through piece-wise linear reconstruction method as employed by Barth and Jespersen [124]. This method incorporates piece-wise linearly

distributed flow variables over the control volume. Thus left and right variables are computed as follows,

$$X_L = X_{Icell} + \psi(\nabla X_{Icell} \cdot \vec{n}_L), X_R = X_{Jcell} + \psi(\nabla X_{Jcell} \cdot \vec{n}_R) \tag{2.21}$$

Here, X_L and X_R are the values of variables at left and right side of the face respectively while X_{Icell} is state variable at cell center. ψ is a limiter function, and ∇X_{Icell} is the derivative of the state variable at the cell centroid, which is calculated as

$$\nabla X_{Icell} = [\frac{\partial X}{\partial x}, \frac{\partial X}{\partial y}]^T \tag{2.22}$$

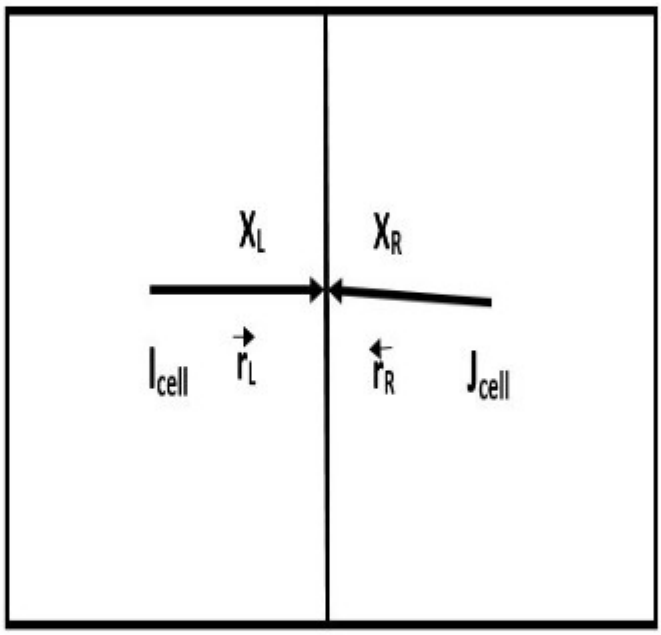

Figure 2.2: Solution reconstruction of cell centered scheme

In the expression, $\vec{n}_L$ and $\vec{n}_R$ represents the vectors pointing from the cell-center towards the face center as shown in the Fig 2.2. Consideration of limiter function (ψ) reduces the monotonicity loss caused by second order accurate solutions at the vicinity of high gradient regions like shock or near the body wall. This limiter function generates non-increasing maxima and non-decreasing minima to ensure that newly calculated left and right flow variables do not exceed the maximum and minimum of the respective cell center values. In the current solver, Venkatakrishnan's limiter is incorporated for faster and better convergence towards exact solutions. According to this methodology

the limiter function is computed as,

$$\psi = \begin{cases} \frac{(\Delta^2_{1,max}+\epsilon^2)\Delta_2+2\Delta^2_2\Delta_{1,max}}{\Delta^2_{1,max}+2\Delta^2_2+\Delta_{1,max}\Delta_2+\epsilon^2} & if \Delta_2 > 0 \\ \frac{(\Delta^2_{1,min}+\epsilon^2)\Delta_2+2\Delta^2_2\Delta_{1,max}}{\Delta^2_{1,max}+2\Delta^2_2+\Delta_{1,max}\Delta_2+\epsilon^2} & if \Delta_2 < 0 \\ 1 & if \Delta_2 = 0 \end{cases} \tag{2.23}$$

Where, $\Delta_{1,max} = X_{max} - X_{Icell}, \Delta_{1,min} = X_{min} - X_{Icell}$. Here, X_{max} and X_{min} are the maximum and minimum values of state variables at all surrounding cells (J), including the cell (I) itself, and are given as:

$$X_{max} = max(X_{Icell}, max_J X_{Jcell}) \tag{2.24}$$

$$X_{min} = min(X_{Icell}, min_J X_{Jcell}) \tag{2.25}$$

The term Δ^2 is represented as $\Delta_2 = \nabla X_{Jcell} \cdot \vec{n}_L$. Further, the quantity ϵ^2 is defined as $\epsilon^2 = (K\Delta h)^3$. Here, K is a constant of order one (generally taken as 2) and Δh is square root of area for 2-D and cube root of volume for 3-D flows.

2.5.3 Calculation of viscous fluxes

Complete evaluation of residual term demands the accurate calculation of viscous fluxes. The calculation of viscous fluxes on the face of a control volume requires the information of the flow variables and their derivative at that location. Consistency and simplicity in spatial discretization is acheived by the assumption that control volume considered for viscous flux calculation is same as in case of inviscid flux calculation. Flow variables at cell faces are calculated by simply taking average of right and left cell values which are represented as,

$$X_{IJface} = \frac{1}{2}(X_{Icell} + X_{Jcell}) \tag{2.26}$$

Here, the gradient of flow variables are calculated at the cell centre using Gauss divergence theorem [125]. All dervatives are first calculated at the cell center and by using area-weighted average method. Afterwards, the node values are calculated by simply averaging the gradient at the corresponing faces. This methodology is mandatory to overcome the demerit of decoupling of calculated gradients at the face boundaries as it generally happens in the simple cell averaging method.

2.6 Boundary conditions

The correct implementation of boundary conditions is important in any solution methodology as improper incorporation of boundary conditions may lead to inconsistent and unphysical computational results. Thus, utmost care is essential for handling of boundary conditions to certain that given problem is well-posed. In the current work, different boundary conditions which are considered, are explained in the following subsections,

2.6.1 Supersonic inlet

As per characteristics theory [126], all eigenvalues must have the same sign for the supersonic inlet boundary condition. To save computational time, the inlet conditions should be chosen as close as possible to final converged values but due to different discontinuities (shock waves) present in flow field it is impossible to have accurate guess. Therefore, all state variables in the inlet are taken as freestream primitive variables, as the high speed freestream is entering the computational domain.

2.6.2 Supersonic outlet

This boundary condition also considers the same sign of eigenvalues. According to this method, it is assumed that the flow leaves the computational domain at supersonic speed and hence it has no upstream impact. Thus, flow variables at the boundary faces are directly assigned from the neighbouring interior cell values using zeroth order extrapolation.

2.6.3 Wall boundary

In the current investigations, both isothermal and adiabatic wall boundary conditions are considered. For these cases, no-slip and impermeable condition are considered at the wall by assigning zero normal and tangential velocity relative at the wall surface. Also, temperature and species mass fractions are fixed at wall for isothermal condition while for an adiabatic cases, temperature gradient and species concentration gradient are forcefully kept zero at the wall. The pressure at the wall faces is obtained from the immediate neighbouring interior cell.

2.6.4 Axi-Symmetry

In this boundary condition, viscous effects near to wall are neglected and the fluid is assumed to slip freely over the surface. The normal component of velocity is zero while

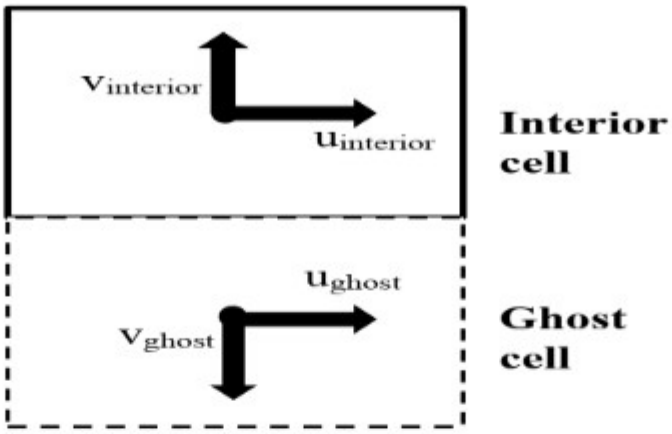

Figure 2.3: Mirror or Ghost cell approach

its tangential component is non-zero. All the fluxes are considered to be zero across the symmetry boundary condition. Thus the inviscid wall and symmetry boundary conditons are similar altough their physical significance is different. To calculate the conservative variables at this boundary, mirror or ghost cell method is adopted as shown in Fig 2.3.

$$u_{interior} = u_{ghost}$$
$$v_{interior} = -v_{ghost}$$
$$p_{interior} = p_{ghost}$$
$$\rho_{interior} = \rho_{ghost}$$

2.7 Temporal discretization

Temporal discretization methodology is important to obtain converged and stable solutions. This method converts the ordinary differential equations into system of algebraic equations. Generally, there are two types of time discretization techniques for time marching problems: one is an explicit method and other is an implicit method but these methods have their own merits and demerits. Among these, explicit method is relatively easy to apply but Courant-Friedrichs-Levy (CFL) criteria gives restriction to the magnitude of the time step. On the other hand, implicit methods are unconditionally stable to give larger time step which reduces the overall computational time. Combination of these two methods, known as semi-implicit method, can also be used for the faster convergence and accurate solutions. The present solver uses semi-implicit approach in which only source term is treated implicitly. Time step in the current solver is calculated as follows,

$$\Delta t = \frac{\kappa\sqrt{A_i}}{[\sqrt{(u_i^2 + v_i^2)} + a_i]} \tag{2.27}$$

Here, κ is CFL number while A_i , a_i , u_i and v_i are area, sound velocity, flow velocities in x and y direction for every i_{th} cell. The constant value of CFL number is chosen as less than one for each and every simulations. In reacting flows, the time scale of chemical reactions is very low as compared to the flow time scale. Thus, to capture flow information accurately, very tiny time steps are required in the discretization methodology which increase convergence time to steady flow solutions. Thus, only source term is discretized implicitly as given by Bussing and Murman [127] in order to increase the time step. To explain this recalling the Eq 2.20

$$\frac{d\bar{X}_i}{dt} = -\frac{1}{\Omega_i}\sum_{J=1}^{n_f} F_{\perp J}\Delta S_J - \bar{S}_i - \alpha\bar{G}_i = R(\bar{X}_i) \tag{2.28}$$

It can be re-written as

$$\frac{X_i^{n+1} - X_i^n}{\Delta t} = -\frac{1}{\Omega_i}(\sum_{J=1}^{n_f} F_{\perp J}\Delta S_J)^n - \bar{S}_i^{n+1} - \alpha\bar{G}_i^n \tag{2.29}$$

The source term $\bar{S}_i$, which is introduced due to chemical reactions, is further decomposed using Newton's method as

$$\bar{S}_i^{n+1} = S_i^n + (\frac{\partial S_i}{\partial X})^n\Delta X + O(\Delta X)^2 \tag{2.30}$$

Putting this value of S_i^{n+1} in Eq 2.10

$$\frac{X_i^{n+1} - X_i^n}{\Delta t} = -\frac{1}{\Omega_i}(\sum_{J=1}^{n_f} F_{\perp J}\Delta S_J)^n - [S_i^n + (\frac{\partial S_i}{\partial X})^n\Delta X + O(\Delta X)^2] - \alpha\bar{G}_i^n \tag{2.31}$$

$$\frac{X_i^{n+1} - X_i^n}{\Delta t} - (\frac{\partial S_i}{\partial X})^n\Delta X = -\frac{1}{\Omega_i}(\sum_{J=1}^{n_f} F_{\perp J}\Delta S_J)^n - S_i^n - \alpha\bar{G}_i^n \tag{2.32}$$

$$\frac{X_i^{n+1} - X_i^n}{\Delta t} - (\frac{\partial S_i}{\partial X})^n(X_i^{n+1} - X_i^n) = -\frac{1}{\Omega_i}(\sum_{J=1}^{n_f} F_{\perp J}\Delta S_J)^n - S_i^n - \alpha\bar{G}_i^n \tag{2.33}$$

$$\frac{X_i^{n+1} - X_i^n}{\Delta t}[I - \Delta t(\frac{\partial S_i}{\partial X})^n] = -\frac{1}{\Omega_i}(\sum_{J=1}^{n_f} F_{\perp J}\Delta S_J)^n - S_i^n - \alpha\bar{G}_i^n \tag{2.34}$$

Here, I is the identity matrix and $\frac{\partial S_i}{\partial X}$ is the jacobian matrix which is calculated by following formula,

$$\frac{\partial S_i}{\partial X} = \begin{bmatrix} 0 & 0 & 0 & 0 & 0 & \cdot & \cdot & 0 \\ 0 & 0 & 0 & 0 & 0 & \cdot & \cdot & 0 \\ 0 & 0 & 0 & 0 & 0 & \cdot & \cdot & 0 \\ 0 & 0 & 0 & 0 & 0 & \cdot & \cdot & 0 \\ \frac{\partial S_1}{\partial \rho} & \frac{\partial S_1}{\partial \rho u} & \frac{\partial S_1}{\partial \rho v} & \frac{\partial S_1}{\partial \rho E} & \frac{\partial S_1}{\partial C_1} & \cdot & \cdot & \frac{\partial S_1}{\partial C_{N-1}} \\ \frac{\partial (\cdot)}{\partial \rho} & \frac{\partial (\cdot)}{\partial \rho u} & \frac{\partial (\cdot)}{\partial \rho v} & \frac{\partial (\cdot)}{\partial \rho E} & \frac{\partial (\cdot)}{\partial C_1} & \cdot & \cdot & \frac{\partial (\cdot)}{\partial C_{N-1}} \\ \frac{\partial (\cdot)}{\partial \rho} & \frac{\partial (\cdot)}{\partial \rho u} & \frac{\partial (\cdot)}{\partial \rho v} & \frac{\partial (\cdot)}{\partial \rho E} & \frac{\partial (\cdot)}{\partial C_1} & \cdot & \cdot & \frac{\partial (\cdot)}{\partial C_{N-1}} \\ \frac{\partial S_{N-1}}{\partial \rho} & \frac{\partial S_{N-1}}{\partial \rho u} & \frac{\partial S_{N-1}}{\partial \rho v} & \frac{\partial S_{N-1}}{\partial \rho E} & \frac{\partial S_{N-1}}{\partial C_1} & \cdot & \cdot & \frac{\partial S_{N-1}}{\partial C_{N-1}} \end{bmatrix}$$

Here, only diagonal terms of matrix $\frac{\partial S_i}{\partial X}$ are considered to make easy to inverse the matrix and save computational time. The elements in the Jacobian matrix, can be evaluated by chain rule of differentiation as follows,

$$\frac{\partial S_j}{\partial T}|_{C_i, i=1,\cdot,\cdot,N-1} = W_j \sum_{i=1}^{N_R} (d''_{ij} - d'_{ij}) [\frac{K_{fi}}{T}(m_{fi} + \frac{E_{fi}}{R_u T}) \prod_{l=1}^{N} n_l^{d'_{il}} - \frac{K_{bi}}{T}(m_{bi} + \frac{E_{bi}}{R_u T}) \prod_{l=1}^{N} n_l^{d''_{il}}] \tag{2.35}$$

$$\frac{\partial S_j}{\partial \rho u}|_{\rho, \rho E, C_i, i=1,\cdot,\cdot,N-1} = -\frac{u}{\rho C_v} \frac{\partial S_j}{\partial T}|_{C_i, i=1,\cdot,\cdot,N-1} \tag{2.36}$$

$$\frac{\partial S_j}{\partial \rho E}|_{\rho, \rho E, C_i, i=1,\cdot,\cdot,N-1} = \frac{1}{\rho C_v} \frac{\partial S_j}{\partial T}|_{C_i, i=1,\cdot,\cdot,N-1} \tag{2.37}$$

$$\frac{\partial S_j}{\partial C_i}|_{C_i, i=1,\cdot,\cdot,N-1} = W_j \sum_{k=1}^{N_R} (d''_{ki} - d'_{ki}) [\frac{d'_{ki} K_{fk}}{C_i} \prod_{l=1}^{N} n_l^{d'_{kl}} - \frac{d''_{ki} K_{bk}}{C_i} \prod_{l=1}^{N} n_l^{d''_{kl}}] - \frac{(e_i - e_N)}{\rho C_v} \frac{\partial S_j}{\partial T}|_{C_i, i=1,\cdot,\cdot,N-1} \tag{2.38}$$

At last, if all the flow variables are known at n^{th} time instant, then their respective values can be evaluated at $(n+1)^{th}$ time instant with successive time marching from Eq 2.34.

2.8 Gas models

Choice of the gas model to be used in supersonic/hypersonic flow regimes is very important to accurately predict flow field. In the current study, both low as well as high enthalpy flows are examined to explore the real gas effect. In context of this, different gas models are incorporated in the present solver and are successfully employed. The full details of these gas models with their application are explained in the following sections,

2.8.1 Perfect gas model

Perfect gas model assumes intermolecular forces between the molecules to be negligible. In this model, specific heat at constant pressure (C_p), specific heat at constant volume (C_v) are considerd as constants. Ideal gas eqation as given in Eq. 2.39 can be used for the calculations of the transport properties. Researchers [128] have used this model to analyse the non-reacting flows.

$$pv = mRT \tag{2.39}$$

Here, p is pressure, v is volume of gas, m is mass of gas, T is temperature and R is specifc gas constant. Further, this model incorporates specific internal energy (e), sound speed (a) and static enthalpy of gas (h) as given by following formula,

$$e = \frac{RT}{\gamma - 1}, a = \sqrt{\gamma RT}, h = \frac{\gamma p}{\rho(\gamma - 1)} \tag{2.40}$$

Here, ρ is the gas density. Sutherland's viscosity law [129] is employed for the determination of the gas viscosity (μ) in present solver. The dimensionless form of the gas viscosity according to this law is given as,

$$\frac{\mu}{\mu_{ref}} = (\frac{T}{T_{ref}})^{\frac{3}{2}}(\frac{T_{ref} + S}{T + S}) \tag{2.41}$$

Here,μ_{ref} is reference abolute viscosity of air at given temperature which is equal to $17.16 \times 10^6 Ns/m^2$, T_{ref} is the reference temperature which is taken as 273.15 K and S is a constant which is taken as 110.56.

2.8.2 Non-equilibrium gas model

As it is well understood that hypersonic vehicles often encounter high temperature regions at post-shock locations where calorically perfect gas assumption remains no longer valid and non-equilibrium consideration becomes dominating. Thus, the perfect gas model is inappropriate to employ for computations and hence non-equilibrium gas model must be used to accurately capture the high speed and high enthalpy flow-field. This model solves coupled Navier-Stokes along with species continuity equations simultaneously. Further, the thermophysical properties and flow variables are calculated as given in section 2.1.

2.8.3 Frozen gas model

In this gas model, thermo-physical properties are calculated exactly as mentioned in non-equilibrium gas models while the chemical reactions of gas species are neglected. Hence, only Navier-Stokes equations are solved for effective numerical simulation of hypersonic flows. However, if the inlet freestream flow is chemically decomposed then this model includes solution of all the equations of species continuity without considering their source term. This gas model is also an integral part of the current solver.

2.9 Data Reduction

Various paremetres such as Coefficient of drag (C_d), Coefficient of pressure (C_p) and Stanton number (St) are calculated using the following equations.

$$C_d = \frac{F_d}{\frac{1}{2}\rho_\infty u_\infty^2 A_p}, Where A_p = \frac{\pi D^2}{4}. \tag{2.42}$$

$$C_p = \frac{2(p - p_\infty)}{\rho_\infty u_\infty^2} \tag{2.43}$$

$$St = \frac{q_w}{\rho_\infty C_{p\infty} u_\infty (T_{aw} - T_w)} \tag{2.44}$$

Where $T_{aw} = T_\infty(1 + \frac{\gamma-1}{2} M_\infty^2 Pr^{\frac{1}{3}})$

Jet pressure ratio (PR) is defined by Eq. 2.45

$$PR = \frac{P_{oj}}{P_{o\infty}} \tag{2.45}$$

Where P_{oj} and $P_{o\infty}$ are jet total pressure and total pressure of freestream respectively.

Exergy destruction value (E_d) and percentage exergy destruction (E_o) is calculated from Eq 2.46 and Eq 2.47 as defined in [117]. The first two terms represent exergy destruction due to heat and work transfer at the wall, rest of the terms gives exergy of freestream, jet and outlet flows respectively.

$$\begin{aligned} E_d = [1 - \frac{T_o}{T_w}]\dot{Q}_w - \frac{C_f \rho_\infty u_\infty^3 A_s}{2} + \dot{m}_1[(h_1 - T_o s_1) + \frac{u_\infty^2}{2}] \\ + \dot{m}_2[(h_2 - T_o s_2) + \frac{u_j^2}{2}] - (\dot{m}_1 + \dot{m}_2)[(h_3 - T_o s_3) + \frac{u_o^2}{2}] \end{aligned} \tag{2.46}$$

$$E_o = \frac{E_d}{E_i} \times 100 \tag{2.47}$$

Entropy generation rate ($\dot{S}_g$) is calculated from Eq 2.48 as defined in [130]. The first three terms on left hand side of this equation represent entropy of freestream, jet and outlet flows respectively. The fourth term gives entropy change due to heat transfer at the wall while right hand side gives entropy change of the system.

$$\dot{m}_1 s_1 + \dot{m}_2 s_2 - (\dot{m}_1 + \dot{m}_2) s_3 - \frac{\dot{Q}_w}{T_w} + \dot{S}_g = \frac{\Delta S}{\Delta t} \tag{2.48}$$

In case of drag reduction using counter flow jet, momentum ratio of the jet is calculated as follows [131],

$$R_{ma} = \frac{\rho_j u_j^2 d_j^2}{\rho_\infty u_\infty^2 d_b^2} \tag{2.49}$$

This parameter can be further decomposed as,

$$\begin{aligned} R_{ma} = & \frac{\rho_j u_j^2 d_j^2}{\rho_\infty u_\infty^2 d_b^2} = \frac{p_j M_j^2 \gamma_j d_j^2}{p_\infty M_\infty^2 \gamma_\infty d_b^2} \\ & = \frac{p_j}{p_\infty} \frac{M_j^2}{M_\infty^2} A = \frac{p_j}{p_{oj}} \frac{p_{o\infty}}{p_\infty} \frac{M_j^2}{M_\infty^2} (PR) A \end{aligned} \tag{2.50}$$

The performance parameters for drag reduction techniques viz. percentage drag reduction and injection effectiveness, are calcuated using Eq. 2.51 and Eq. 2.52 respectively.

$$\%DR = \frac{(CD_o - CD)}{CD_o} \times 100 \tag{2.51}$$

$$\eta = \frac{(F_{do} - F_d) u_\infty}{\frac{1}{2} \rho_j u_j^3 A_j} \tag{2.52}$$

2.10 OP2 formulation

For the accurate and quick solution of unstructured or structured mesh related problems, OP2 can be used as an active framework [132]. OP2 incorporates source-to-source translation which converts an application code running on single core into various parallel computations running on multi core by writing the serial code using the OP2 framework. This conversion results in almost optimal performance of multi core systems. This parallel execution of many core processor significantly reduces the computational time resulting in quick and accurate solution of unstructured mesh based areas. By choosing correct thread and partition configuration, factors reducing the GPU performance can be overcome for optimal performance of systems. Thus, the current investigations also incorporates this OP2 based framework to significantly lower the runtime of the developed solver.

2.11 Validation test cases

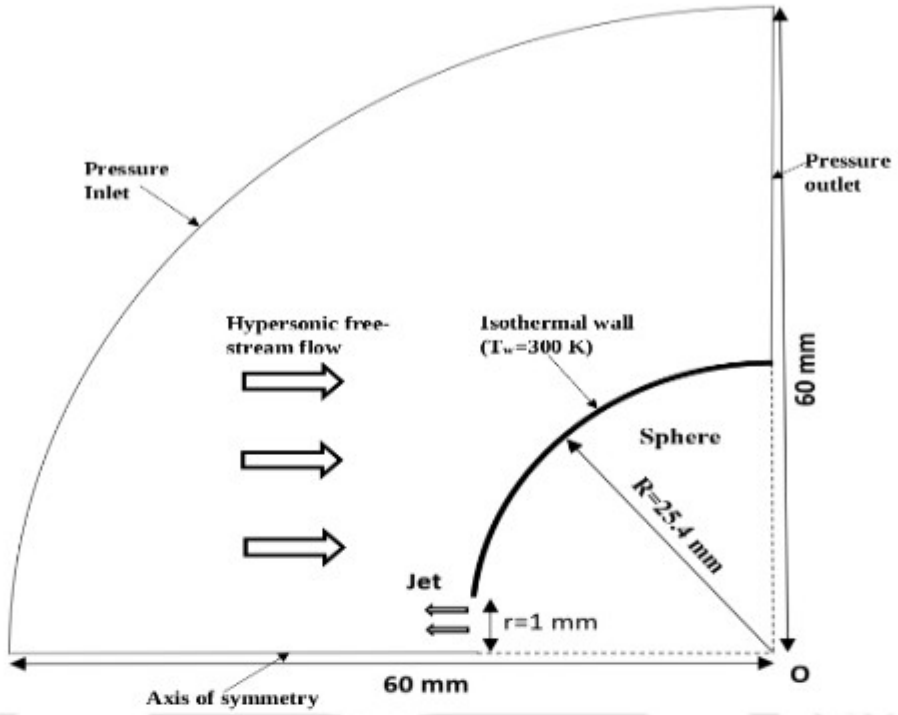

Figure 2.4: Model geometry with its boundary conditions

The geometry for the validation of surface pressure computed from the present solver is taken as the hemi-sphere of diameter 50.8 mm. Every detail and dimension of this model with its boundary conditions is presented in Fig 2.4. The freestream static pressure and Mach number are taken as the 16146.9 Pa and 2.5 respectively as experimentally suggested by Finley [7]. Exit of the counter-jet is situated at stagnation point (as shown in Fig. 2.4). The diameter of the jet is kept constant as 6.68 mm. Air is taken as working fluid for freestream and opposing jet respectively. No−slip, viscous and isothermal wall (T_w=300 K) boundary condition is given at the body surface. Singular axis or axisymmetric boundary condition is used at the axis. Thus only half portion of the domain is considered for computations as it also decreases the computational time of the solver. The solution is considered to be converged when the residual reaches a minimum value of order of five. Similar computational strategy has been employed for the viscous non−equilibrium hypersonic flows [133] [67]. Table 2.2 shows flow details of freestream and jet for validation case. Non-dimensional surface pressure computed from current solver for jet pressure ratio (PR) of 2.23 and 2.08 are plotted and compared with corresponding experimental results [7] in Fig 2.5(a) and Fig 2.5(b) respectively. The experimental measured surface pressure is in good agreement with the numerically computed surface pressure of present reacting solver. Figure 2.5(b) also shows good

agreement of computed surface pressure with modified Newtonian theory for the no jet case where modified Newtonian theory based surface pressure is given as,

$$\frac{p}{p_{of}} = cos^2\theta + sin^2\theta \frac{p_\infty}{p_{of}} \tag{2.53}$$

Table 2.2: Flow conditions of free−stream and opposing jet for validation

Properties	Freestream (Air)	Opposing jet (Air)
Mach Number	2.5	1
Static Pressure (Pa)	16147	16147,151522,122383
Static Temperature (K)	131	245

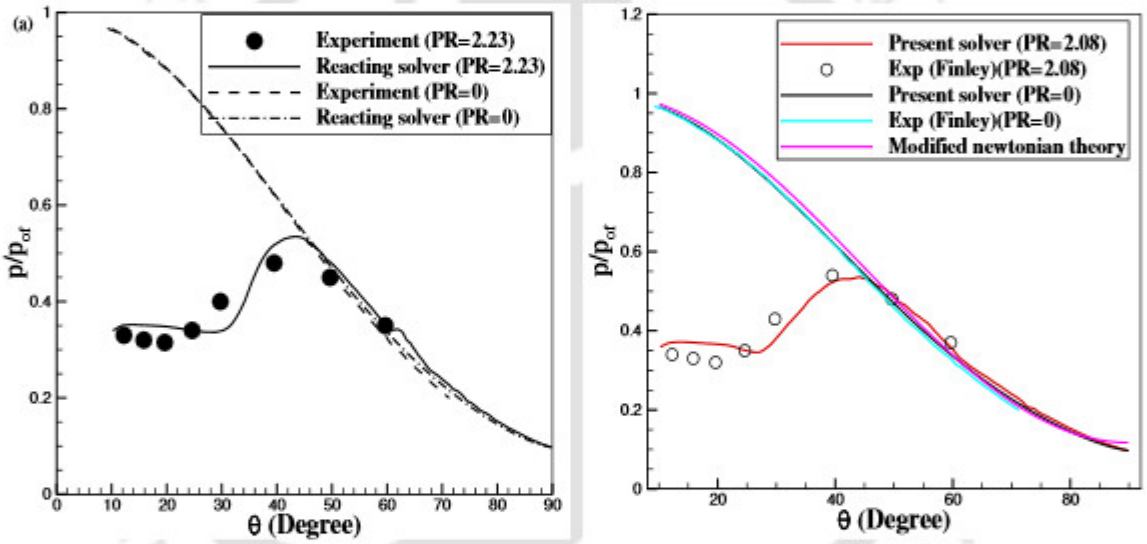

(a) PR=2.23 (b) PR=2.08

Figure 2.5: Comparison of non−dimensional surface pressure of current computation with experimental results

Non-dimensional surface pressure computed from current solver for jet pressure ratio (PR) of 1.68 and 2.84 are plotted and compared with corresponding experimental results [7] in Fig 2.6 and Fig 2.7 respectively. Figure 2.7 depicts surface pressure variation obtained from current solver for three different grid sizes as well. Results of fine mesh with 100K cells match closely with the experimental data of Finley [7] and such fine mesh is used for all the cases in this work. Surface pressure obtained from the present solver is in good agreement with experimental data of Finley [7] for both pressure ratios and Modified newtonian theory for no-jet condition. Comparison of surface pressure obtained from the present laminar flow solver is also done with counter-jet turbulent case

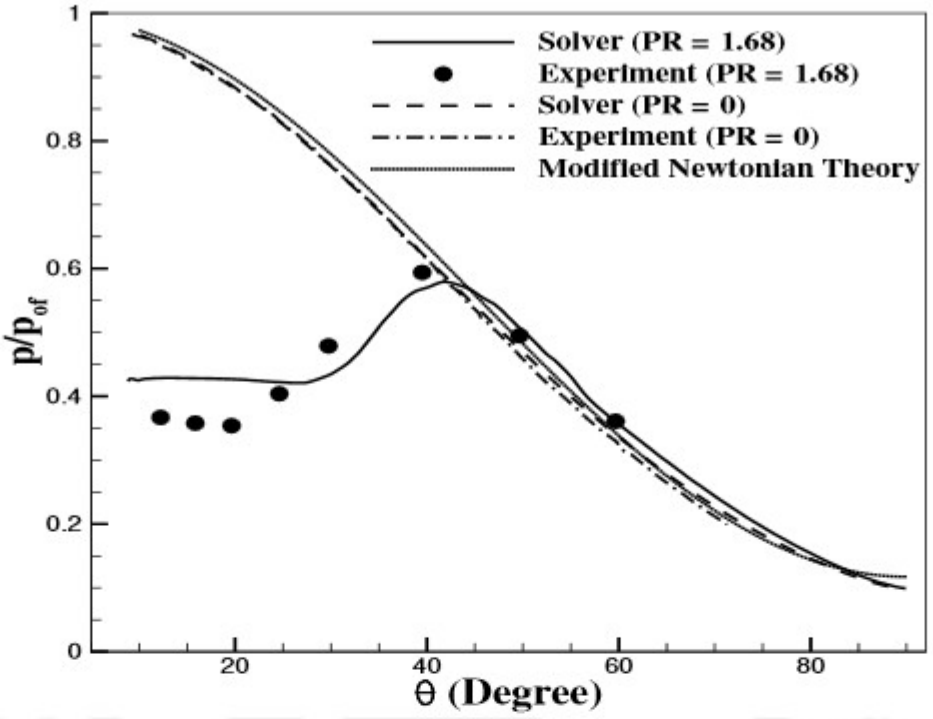

Figure 2.6: Comparison of surface pressure with experimental results for jet PR=1.68

of Chen et al [134] and experimental case of Karashima and Sato [25] and shown in Fig 2.7 to explain the insignificance of turbulence effects on the prediction of surface pressure. Details of the freestream and jet conditions for above mentioned numerical and experimental literature are given in Table 2.3. Figure 2.7 clearly depicts good agreement of predicted surface pressure of the present laminar flow solver with turbulent numerical simulations (Chen et al [134]) and experimental (Karashima and Sato [25]) results. Similar computational solver was used by (Desai et al [135] and Kumar and Kulkarni [117]) for non-equilibrium viscous flows. This justifies the use of present laminar solver for counter-jet flow investigations.

Table 2.3: Flow conditions for validation

Case	$\frac{d_m}{d_j}$	M_∞	T_∞(K)	$P = \frac{P_{oj}}{P_{of}}$
1) Karashima and Sato [25], Chen et al [134]	10	2.5	130.86	1.6
2) Finley [7]	7.6	2.5	130.86	2.84

Validation studies are also extended for the comparison of shock shape using the Billig's correlation [136]. The computed shock shape and shock stand-off distance for no injection case are in good agreement with the Billig's correlations as shown in Fig 2.8.

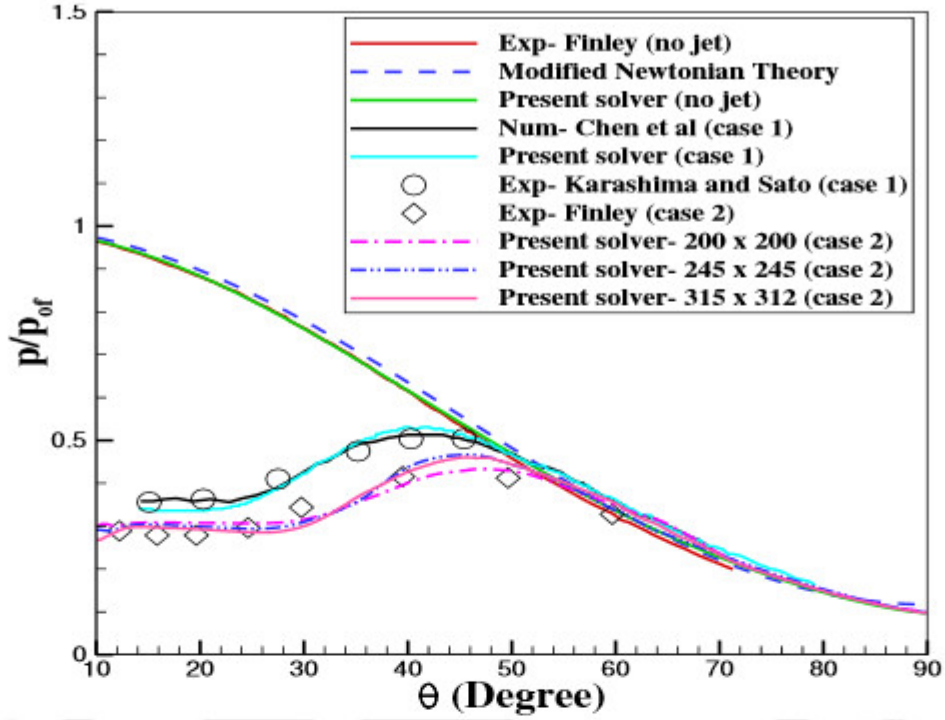

Figure 2.7: Non-dimensional wall pressure comparison with experimental results from literature at various grid sizes

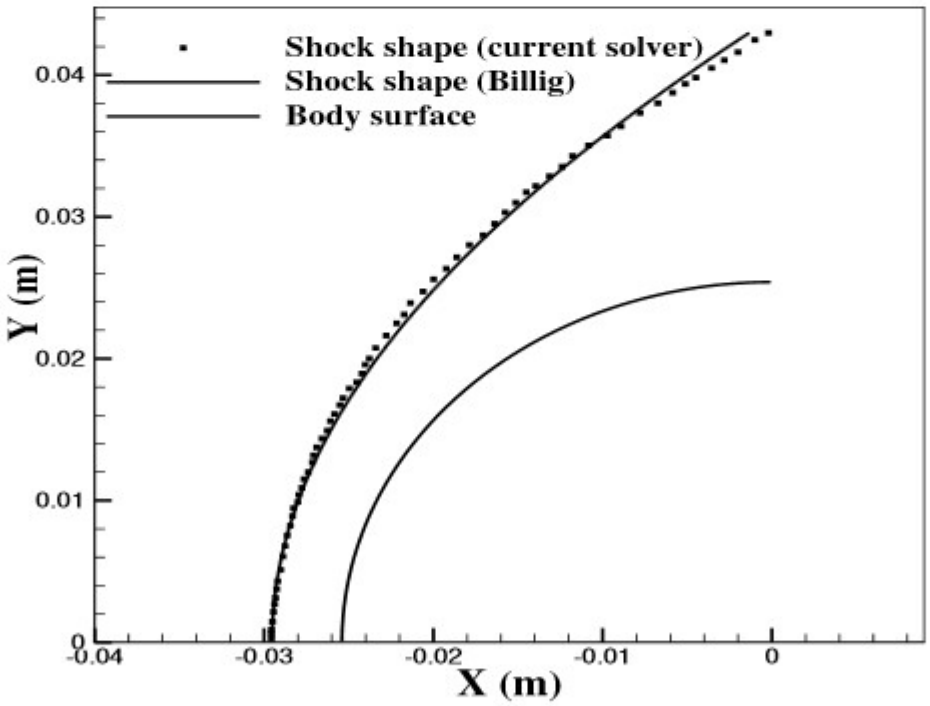

Figure 2.8: Comparison of shock shape with Billig correlation

2.12 Conclusions

In this chapter, we discussed about the governing equations related to high speed aerodynamic flows and their discretization using finite volume method. Various chemical reactions are also taken into account which should be considered at elevated temperatures for accurate solution of the flow field. Different convective flux computational schemes are also presented in this chapter. Boundary conditions and their implications at inlet, wall and outlet are also discussed. Various fluid flow models included in the solver are represented and incorporation of OP2 framework in the solver is also presented which significantly reduces the computational runtime of the developed solver. Lastly, developed real gas flow solver is simulated for numerous experimental test cases available in the literature and validation results are depicted to demonstrate solver reliability for the calculations of different flow parameters.

CHAPTER 3

EXERGY DESTRUCTION AND DRAG REDUCTION ANALYSIS OF ACTIVE AND PASSIVE TECHNIQUES

Counter-flowing jet and aero-spike are quite effective and widely employed drag reduction techniques. These techniques, being constitutionally different, are governed by different governing parameters but are assessed by percentage drag reduction. This assessment parameter is not suitable to compare two techniques of different kind as one of them is active and other is passive drag reduction technique. Therefore, thermodynamic parameter named "exergy destruction" is proposed as a unified performance assessment parameter. Test case of supersonic flow over hemisphere, provided with counterflow injection is simulated which portrayed monotonic variation for percentage drag reduction and percentage exergy destruction for increase in injection pressure ratio, since decreased shock strength reduces the wave drag and also the exergy destruction. However, injection effectiveness, a suitable assessment parameter for counterflow injection, shows inversion characteristics with a peak at specific injection pressure ratio for given freestream Mach number. Mounting of a spike has also been assessed for different lengths and here as well percentage drag reduction and percentage exergy destruction showed similar trend with inverse relation among them. Hybrid drag reduction technique or a combination of spike and jet has also been considered to highlight the importance of percentage exergy destruction as a performance assessment parameter. Present investigations recommend percentage exergy destruction as a unified performance assessment parameter for passive, active and combination drag reduction techniques.

3.1 Introduction

Many researchers have examined the various drag reduction techniques for hypersonic flows over blunt objects. Different active and passive techniques are available to reduce this drag force. Passive techniques used for this objective include a retractable aero-spike [67] and forward facing cavity [89]; whereas active techniques use injection of opposing jets [137] from stagnation point or upstream energy deposition [70]. Combination of active and passive techniques [138] are also studied for high speed flows.

The counter flow jet alters the flow field in the vicinity of stagnation point and helps to reduce the wave drag. Hence it has been extensively investigated by researchers in the past few decades. It is evident that the major governing parameters considered by the researchers while understanding the performance of counter-flowing sonic or supersonic jets are injection pressure ratio, opposing jet species, jet diameter and jet Mach number. Similarly, spike dimensions and shapes were studied and their effects are reported in the literature for the spike based drag reduction technique. Alteration of drag or surface heat flux should be expected with alteration in these parameters. Since both techniques are constitutionally different, they have different performance parameters. Hence it is not possible to compare their effectiveness or performance for same freestream conditions with the help of existing performance estimation parameters like percentage drag reduction. Further, it needs to account multiple and mixed governing parameters while working with jet and spike combination for drag reduction. This fact demands a common performance parameter to be thought for, which is based upon elementary underlying principles. Exergy is such a fundamental quantity and percentage exergy destruction is a standard performance parameter adopted for various flow processes. It should be noted that, exergy destruction has never been considered as a tool for the analysis of drag reduction techniques. Therfore percentage exergy destruction is considered herein for the first time to examine the drag reduction techniques for their performance and to compare various drag reduction techniques. Further, most of the computational studies for spike or jet based drag reduction assume perfect gas flow. Hence the current investigation is centered on the real gas effects while considering exergy destruction from the computational results obtained for opposing jet, spike and combination cases. Findings of the current study along with simulation results are explained in the following sections.

3.2 Model description and flow conditions

The geometry with its boundary conditions used for counter-jet based technique is depicted in Fig 3.1(a). During the simulation for counter-jet case, diameter of hemi-sphere

is taken as 50.8 mm and jet inlet diameter as 2 mm. This test model along with freestream conditions as freestream total enthalpy of 0.3 MJ/kg, freestream total pressure of 0.27 MPa and Mach number of 2.5 were considered by Finley [7] during counter-flow injection experiment for unit jet Mach number. The geometry with its boundary conditions used for spike based technique is depicted in Fig 3.1(b). The diameter of the body is 72 mm, while the spike diameter is 2 mm. Here the object experiences hypersonic flow of Mach number 8.2, freestream stagnation pressure of 10.9 MPa and freestream stagnation enthalpy of 0.97 MJ/kg.

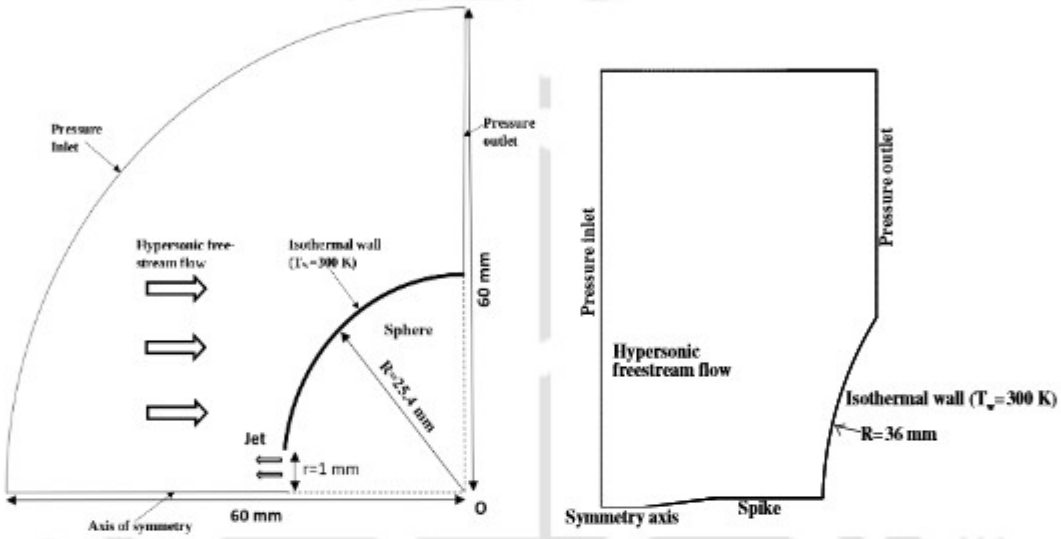

(a) Model for the counter-flowing jet (b) Model for the spike body

Figure 3.1: Model geometry with its computational domain and boundary conditions

One of the simulations is also performed to demonstrate the effects of wake region on the flow field and surface pressure prediction. Figure 3.2(a) shows Mach contour comparison while Fig 3.2(b) shows surface pressure comparison for the cases with and without simulation of wake region. It is clearly observed that there is almost no difference in shock shape and shock location for both the cases and surface pressure distribution on the body is also same for these cases. Also there is negligible variation in drag coefficient for the case without wake (C_d=0.84) as compared to with wake case (C_d=0.86). Thus, inclusion of wake region does not alter the drag force and flow features significantly.

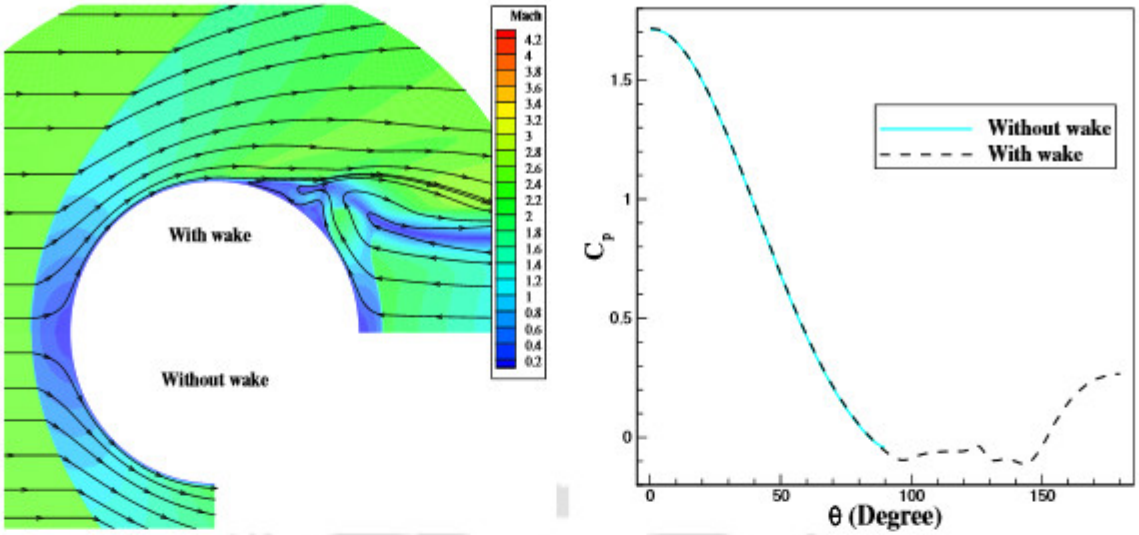

(a) Mach contour comparison with and without wake region

(b) corresponding surface pressure variation

Figure 3.2: Comparison of with and without wake region

3.3 Spiked body validation

The geometry adopted for given validation purpose is a spherical object of 36 mm radius. Spike of 2 mm diameter is attached at its nose creating an vertex angle of 66 deg and the total projected diameter of 39 mm as mentioned in [65]. Hypersonic freestream of Mach number 8.2 is allowed to flow over given object with static pressure of 950 Pa and static temperature of 89.3 K. Figure 3.3 depicts comparison of non-dimensional drag coefficient with experimental data [65] for various L/D ratio of spike attached configuration. Excellent consistency is observed between measured and computed drag values. This justifies the use of present reacting solver for investigation of hypersonic flow over spiked object.

To find the optimum number of processors to be used for the simulations, the case without injection is taken and is run with different number of threads using OpenMP. The simulation runtime is compared with the sequential version to find the optimum number of threads to be used. A workstation of 16 processors and 64 GB RAM is employed for these simulations. Table 3.1 shows the computational time taken by the solver for 500 iterations using optimum sequential, and OpenMP using four and eight threads for the no−injection case of Finley [7]. The OpenMP version with four threads is found to be optimal for the current mesh size. Therefore all the simulations in the current work are performed using four processors in OpenMP.

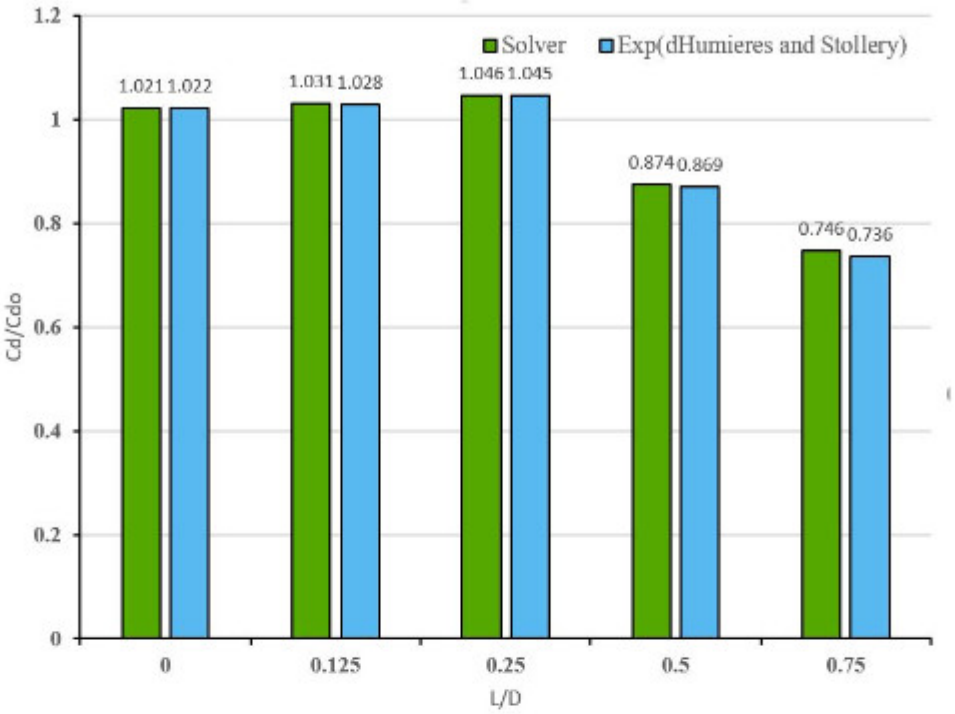

Figure 3.3: Drag coefficient comparison for various L/D ratio

Table 3.1: Computational time (sec) for 500 iterations of no−jet case of Finley, using sequential and OpenMP versions

Method	Optimal sequential	OpenMP (4 threads)	OpenMP (8 threads)
Computational time (sec)	1530.33	397.14	398.9

3.4 Results and discussion

3.4.1 Assessment of counter flow injection technique

Possibility of having a jet from the orifice exists, if the total pressure of the jet is more than the total pressure of the flow behind the bow shock. Increase in injection pressure ratio increases the jet momentum and pushes the forebody bow shock away from it. But, the multiple cell structure of the jet, for these low injection pressure ratios, make the flow unsteady. Counter jet based flow field becomes steady when the injection pressure ratio crosses a critical value. For the pressure ratios, beyond the critical value, single cell structure is present in the jet. Simulations for injection cases are performed for freestream Mach number of 2.5 and 3.5 while injection pressure ratios (PR) are taken as 1.45, 1.52, 1.68, 2.08, 2.23, 2.84, 3.73 and 4.7. The same test model as considered by Finley [7] is adopted herein along with the freestream and jet conditions. Figure 3.4 shows computed

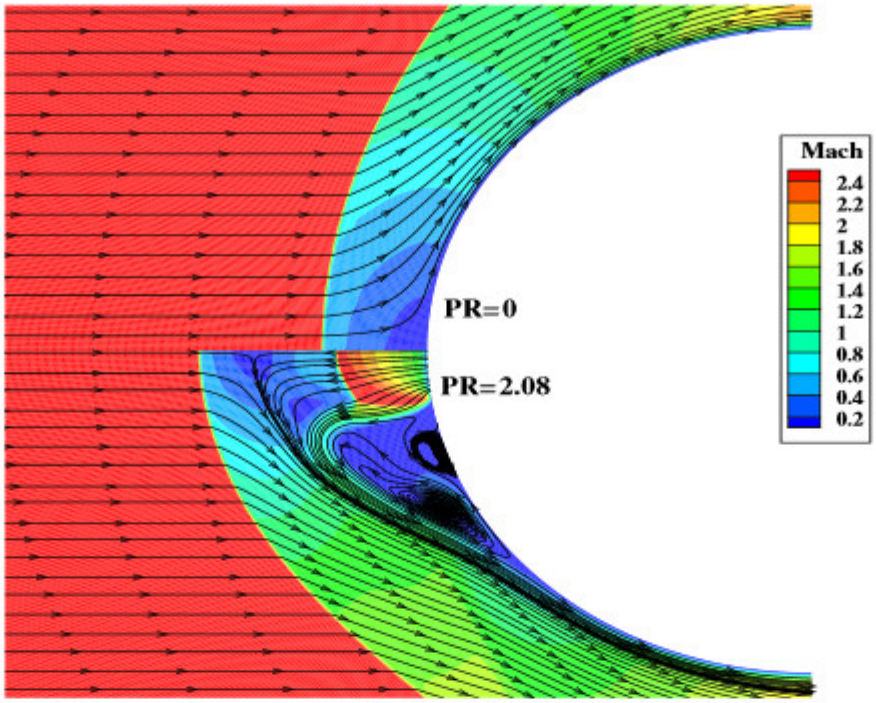

Figure 3.4: Mach contour comparison for PR=0 and PR=2.08 cases

flow field with and without counter flow injection. Presence of strong bow shock is evident for no injection case and is responsible for the large exergy destruction. But the flow field and shock structure are different with injection of counter jet. It is evident from the figure that the underexpanded jet comes out of the orifice and expands till it encounters the Mach disc in the axial direction. This expansion is limited by the barrel shock in transverse direction. Thus the single jet cell is bounded by the Mach disc and barrel shock. Upon crossing the Mach disc, jet flow meets the oncoming high speed flow behind the bow shock at the interface or at the floating stagnation point. Then the jet fluid gets convected downstream in the shock layer and reattaches on the body. This flow reversal of the injected fluid forms a recirculation region ahead of the object. Such low pressure region and the original blunt object constitute the new obstacle to supersonic/hypersonic flow which in turn alters the shock structure and help to reduce the drag force. In general, percentage drag reduction is an obvious measure of effectiveness of any drag reduction technique. The required drag reduction percentage is evaluated as given in Eq.(2.51).

It is expected that the shock restructuring would lead to less exergy destruction in the presence of injection and it can be one of the measures of performance estimation of the drag reduction technique. Such exergy destruction is calculated using Eq.(2.47). Further, increase in injection pressure ratio would increase the cell length and size of the recirculation zone, which in turn pushes the fore body shock further away from the body. Interestingly, increased jet pressure ratio gives larger shock stand-off distance which

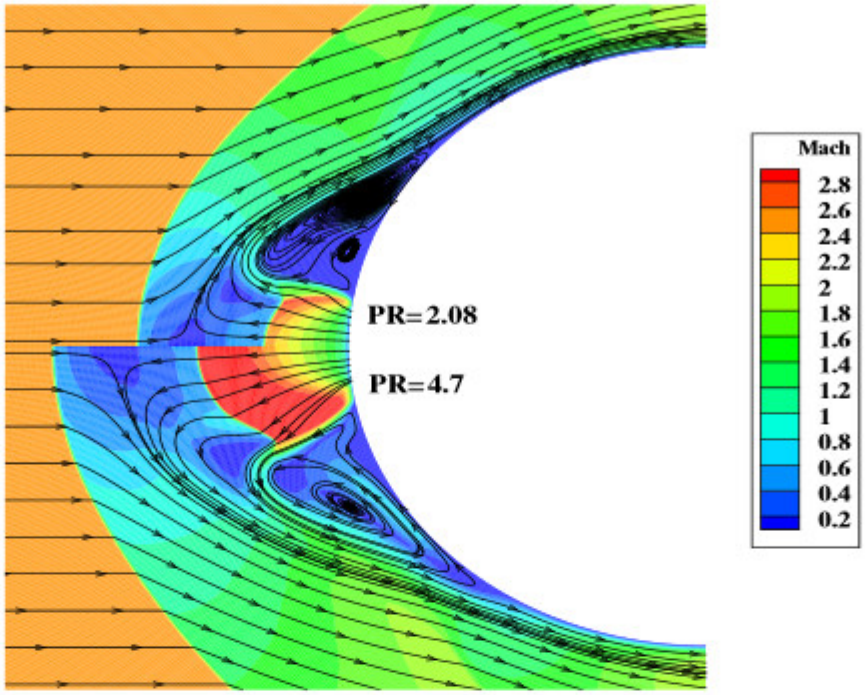

Figure 3.5: Mach contour comparison for PR=2.08 and PR=4.7 cases

forms a relatively weaker shock structure shown in Fig 3.5. Therefore, higher reduction in incurred drag force and lower exergy destruction are obvious with the increase in injection pressure ratio. It should be noted that, in this kind of active drag reduction technique, higher injection pressure ratio demands higher energy input. Therefore the effectiveness of the injection should also be considered while evaluating the performance of this technique. Here, injection effectiveness is defined as the ratio of energy saved because of drag reduction to the input kinetic energy of the jet. Expression for the injection effectiveness is given by Eq.2.52. Alteration in the performance parameters like percentage drag reduction, percentage exergy destruction and injection effectiveness are plotted with injection pressure ratio in Fig 3.6 where M_∞ and H_o are kept constant as 2.5 and 0.3 MJ/kg respectively. Here, percentage drag reduction and percentage exergy destruction show monotonic change with increase in injection pressure ratio. The maximum drag reduction of 54.24 % is noticed for injection pressure ratio of 4.7 where percentage exergy destruction is 2.35 %. Thus these two parameters are relevant with each other for the reason that the exergy destruction decreases with increase in drag reduction. More streamlining of the flow and presence of weaker shocks are the reasons for both the trends with injection pressure ratio. However, the special parameter, injection effectiveness, defined for this drag reduction technique, shows inversion with injection pressure ratio. It suggests that, injection of counterjet is very effective for lower pressure ratios since the rate of drag reduction with initial increment in injection pressure ratio is

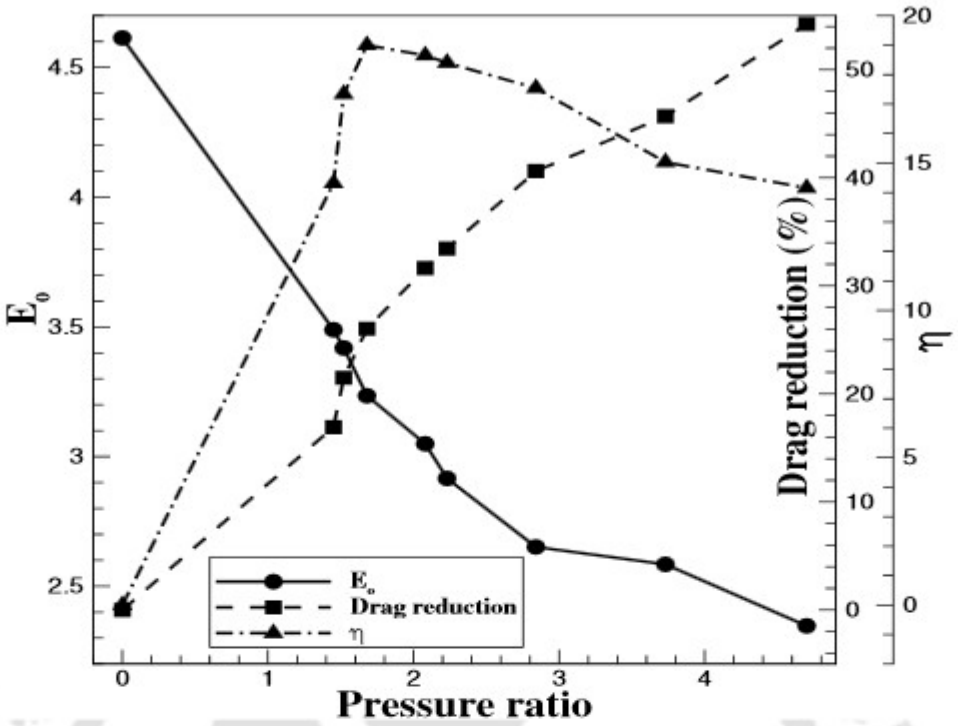

Figure 3.6: Variation of percentage exergy destruction, percentage drag reduction and injection effectiveness (η) with pressure ratio for M_∞=2.5 and H_o=0.3 MJ/Kg

high. But for higher injection pressure ratios, the rate of drag reduction is lower, due to which there is decrease in the effectiveness of injection technique.

Simulations are then performed to understand the effect of Mach number on the dynamics of counter flow injection. Therefore, supersonic flow of Mach number 3.5 is simulated over the same hemi-sphere and with same boundary conditions. Injection pressure ratios, considered earlier, are used here as well to indentify the alteration in assessement paramters with change in Mach number. Typical contour depicting the influence of Mach number on counter flow based injection technique is as shown in Fig 3.7(a). As per this figure, the length of jet−cell is seen to be lowered which in turn brings the Mach disc and the interface closer to the wall for this freestream Mach number of 3.5. Decrease in total pressure behind the strong bow shock and hence the associated decrease in jet total pressure for the same injection pressure ratio are accounted for this alteration in flow field. Therefore, comparatively compact recirculation zone spreads over the sphere. Effect of this flow field on the drag coefficient is shown in Fig 3.7(b). There is small variation in drag coefficient with change in Mach number from 2 to 3.5 for all non−zero injection pressure ratios. However, at higher Mach number of 3.5, the wall pressure remains higher without injection and is responsible for higher value of the incurred drag force when compared to the no injection case at Mach number of 2.5. Therefore percentage drag reduction, at higher Mach number, for the same injection pressure ratio, is

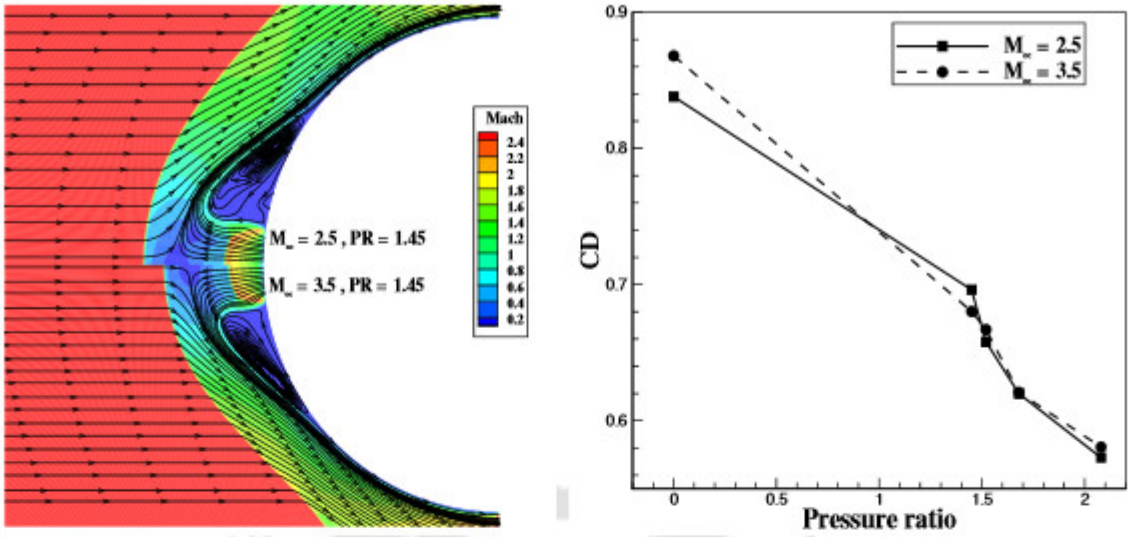

(a) Mach contors for various M_∞ at PR=1.45 (b) Drag variation with pressure ratios

Figure 3.7: Effect of M_∞ on flow field and drag coeifficient

higher. It has been noted that, the percentage drag reduction for injection pressure ratio of 2.08, is 31.63 % for Mach number 2.5 and 33.11 % for Mach number 3.5. Further, the percentage exergy destruction shows that the stronger shock for higher Mach number, with or without injection, leads to higher percentage change in exergy. Moreover, the exergy destruction decreases with increase in injection pressure ratio, for both the freestream Mach numbers and shows monotonic variation as seen in case of pecentage drag reduction as depicted in Fig 3.8. Here, percentage exergy destruction is 3.23 % for Mach number of 2.5 and 3.6 % for Mach number of 3.5. Regarding injection effectiveness, it portrays an inversion at higher Mach number as well. But there is an amplification in this assessement parameter due to increment in free stream Mach number for the same injection pressure ratio. For example, the peak effectiveness corresponding to injection pressure ratio of 1.68, which is 19% for Mach 2.5, increases to 30.92% for Mach 3.5. The mathematical expression of this parameter can be reconsidered to justify this amplification. The freestream velocity from the numerator increases with increase in Mach number while the jet mass flux decreases for the same injection pressure ratio. Hence, the numerator in the expression of effectiveness increases and its denominator decreases, which introduces an amplification in the effectiveness with increase in Mach number for same injection pressure ratio.

3.4.2 Assessment of spike mounting for drag reduction

Figure 3.9(a) shows the comparison of important flow features for spike−based passive drag reduction technique for a spike having a length to diameter ratio of 0.5 and without

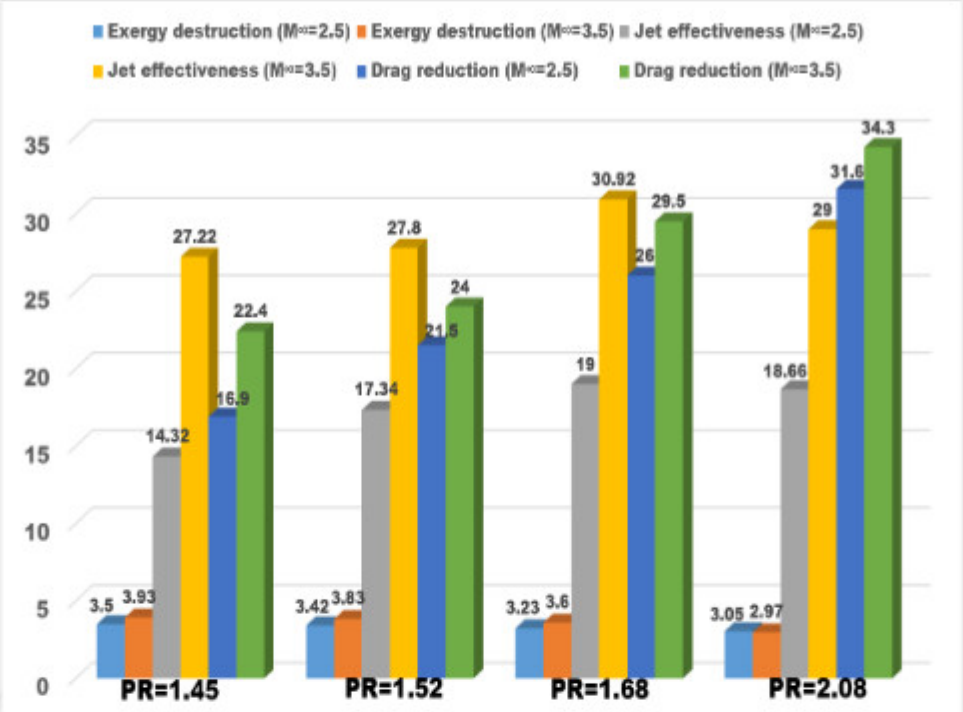

Figure 3.8: Variation of exergy destruction, drag reduction and jet effectiveness with pressure ratio at M_∞=2.5 and M_∞=3.5

spike. The diameter of the body is 72 mm, while the spike diameter is 2 mm [65]. Here the object experiences hypersonic flow of Mach number 8.2, freestream stagnation pressure of 10.9 MPa and freestream stagnation enthalpy of 0.97 MJ/kg. The simulation based surface pressure variation is shown in Fig 3.9(b). For high speed flow over blunt body without spike mounting, strong bow shock would be standing upstream of the body which imposes high pressure on the wall. This bow shock is the major reason for higher exergy destruction in case of high speed flows, hence it is desirable to reduce the strength of this shock. With mounting of an aerospike, at the nose of blunt body, the strong bow shock is seen to be replaced by weak conical shocks and also a low pressure recirculation zone near the nose. This separation bubble acts as a blanket for the blunt body for heat load and also streamlines the flow. Hence mounting of the spike reduces the wall pressure and hence the drag force experienced by the original blunt body. Further, the replacement of strong bow shock by weak conical shocks reduces the exergy destruction. Hence this low cost passive drag reduction technique is many a times favored. It must be noted that, spike mounting being a passive technique, unlike counter flow injection, it is not possible to judge the spike effectiveness. Therefore, assessment of this technique is generally carried out through percentage drag reduction only. Hence it has been attempted herein to estimate the performance of a mounted spike through percentage exergy destruction. In view of this, simulations are performed for different spike lengths attached to the same

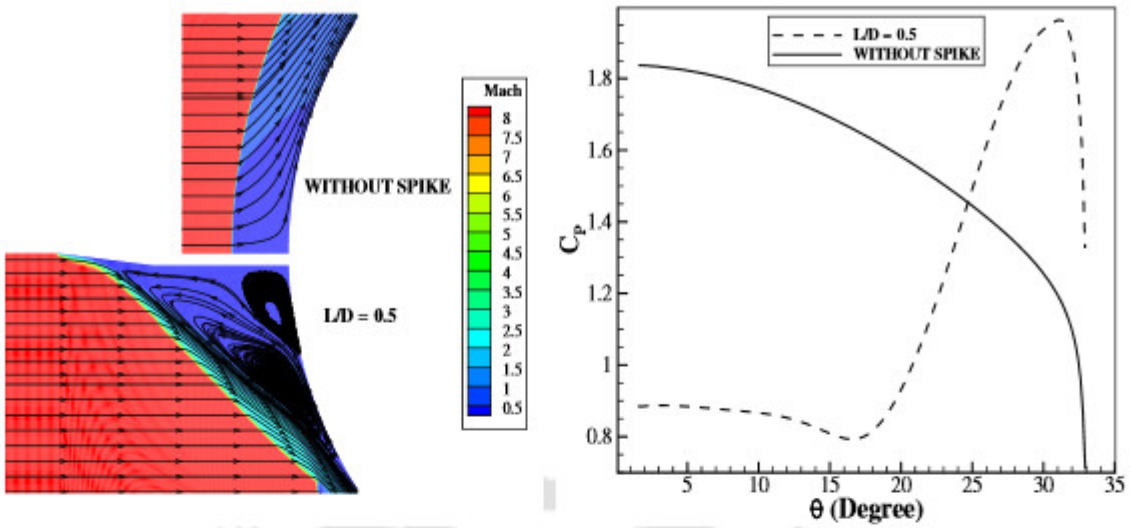

(a) Mach contour comparison for L/D=0 and L/D=0.5 cases

(b) corresponding surface pressure variation

Figure 3.9: Comparison of spiked and unspiked cases

base configuration for the above mentioned freestream conditions. Both the parameters, percentage drag reduction and percentage exergy destruction, show monotonic variation with spike length where percentage drag reduction increases and exergy destruction decreases with the increase in spike length as shown in Fig 3.10. Here, smaller spike of L/D=0.5 has potential of 11.57 % drag reduction with 42.48 % exergy destruction while the longer spike of L/D=1.5 bears higher potential of 61.62% drag reduction with 7.25% exergy destruction. Thus the drag reduction associated with weakening of shock strength is seen again to have relevance with lowering of exergy destruction or losses.

3.4.3 Discussion on performance assessment

It has been noted that, counter flow injection, being active drag reduction technique, can be assessed using injection effectiveness along with percentage drag reduction. But, mounting of spike at the stagnation point is a passive drag reduction technique and it cannot be assessed with the same effectiveness formula. Further, exergy as a thermodynamic parameter has a common trait for either injection techniques. Hence it has been adopted for evaluating the performance of these drag reduction techniques. For M_∞=2.5 and $H_{o\infty}$=0.3 MJ/Kg, counter−jet injection technique gives 2.58 % exergy destruction which corresponds to 45.7 % drag reduction for injection pressure ratio of 3.73 and for the M_∞=8.2 and $H_{o\infty}$=0.97 MJ/Kg, spike technique gives 20 % exergy destruction which corresponds to 48 % drag reduction for L/D ratio of 0.75. For same amount of drag reduction, injection technique proves to be superior since it corresponds to lower exergy

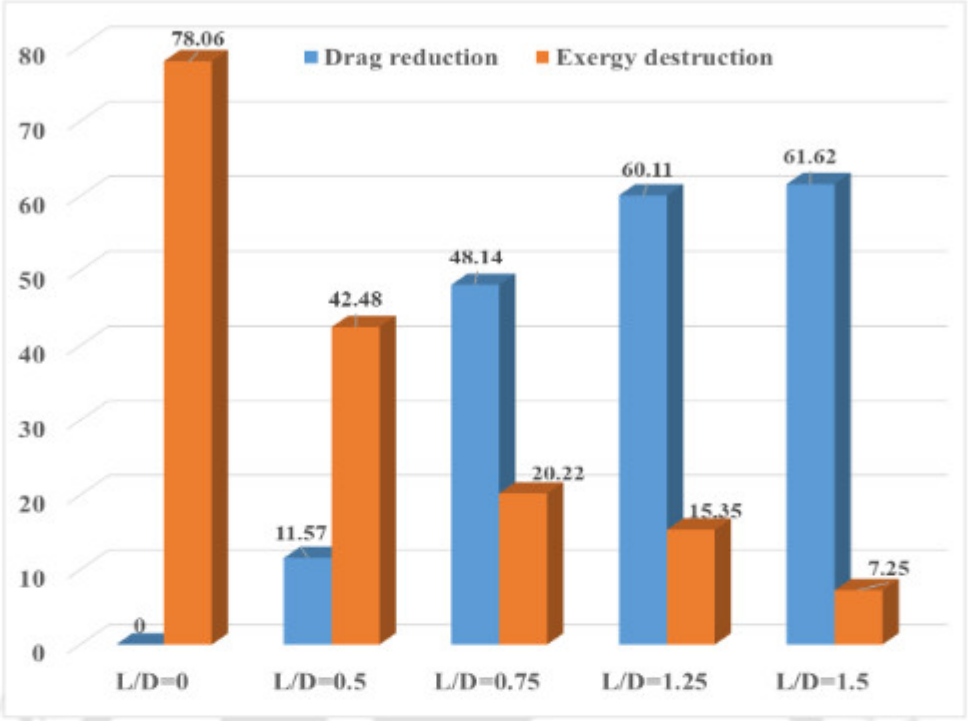

Figure 3.10: Variation of exergy destruction and drag reduction with spike length

destruction than the spike based technique. Moreover, this thermodynamic parameter would also be helpful to test the combination effect of spike and injection. Therefore, simulations are performed for the same test model and the same freestream conditions as the spike case for L/D ratio of 0.5. Here the spike tip is used as the source of counter jet for injection pressure ratio of 5 and combination case gives 1.8% exergy destruction which corresponds to 32% drag reduction (C_d=1.02) while only spike case gives 13% drag reduction (C_d=0.77) and 42% exergy destruction. Mach contours for the spiked object and spike−jet combination are shown in Fig 3.11(a). Here, the freestream conditions are same as the above mentioned case of only spike. Further wall pressure in this case is also compared in the Fig 3.11(b). Jet expanding from the tip of spike pushes the bow shock more away from the body as compared to simple spike case and this increases the recirculation area due to stretching of vortex in vertical direction which results in reduction in surface pressure. Consequently, drag reduction further increases with lesser loss in exergy. Figure 3.12 shows comparison of percentage exergy destruction for similar drag reduction values for various techniques. It is clearly evident that for given drag reduction, opposing jet technique proves to be better than spiked body technique in terms of least percentage exergy destruction.

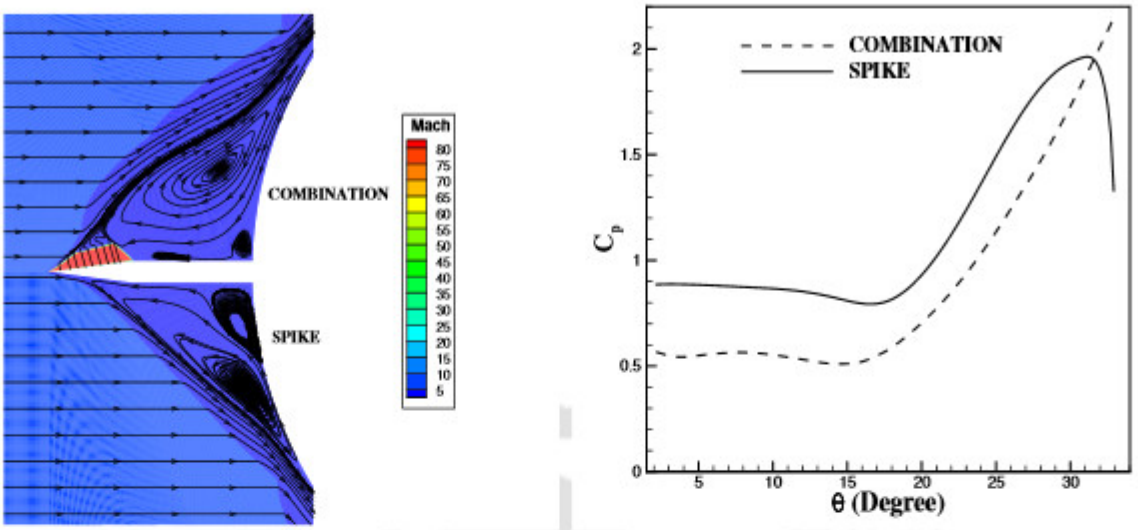

(a) Mach contour comparison for spike and combination case for L/D=0.5

(b) corresponding surface pressure variation

Figure 3.11: Comparison of spiked and combination cases

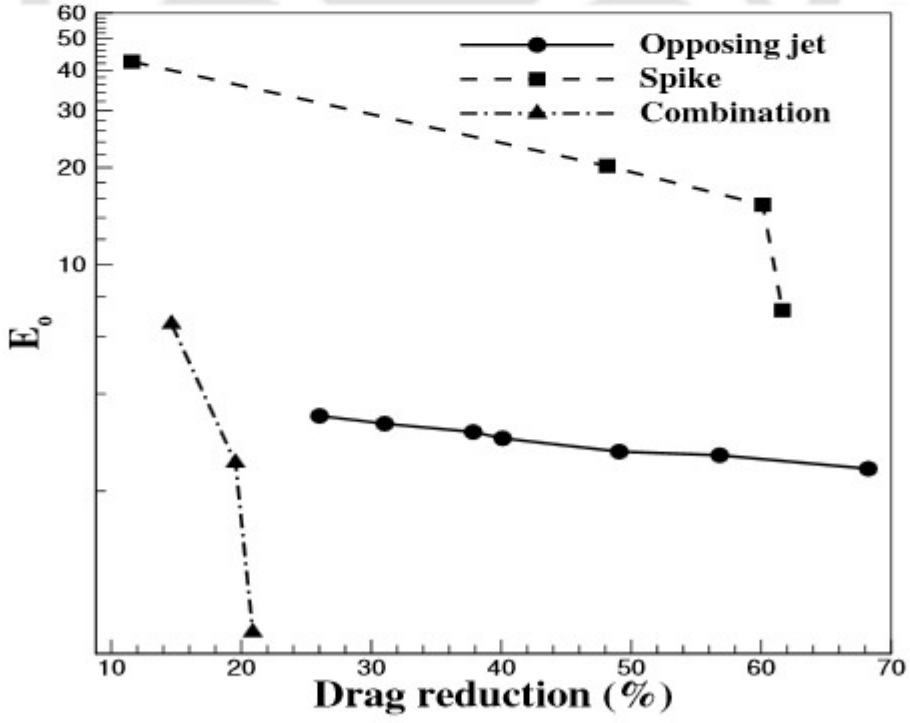

Figure 3.12: Exergy destruction comparison for various techniques

3.5 Conclusions

In view of different drag reduction techniques and their different governing variables, percentage exergy destruction is proposed as a fundamental performance assessment parameter unlike conventional percentage drag reduction or presently proposed injection effectiveness. In case of supersonic flow over a hemisphere with counterflow injection, monotonic variation has been noticed for percentage drag reduction and percentage exergy destruction with increase in injection pressure ratio. It has been noticed that higher injection pressures lead to higher drag reduction and it is mainly due to presence of weaker shock structure at higher injection pressure. Therefore, reduced shock strength leads to lower exergy destruction and higher drag reduction. Hence, percentage drag reduction and percentage exergy destruction are seen to have monotonic variation with injection pressure ratio unlike injection effectiveness which portrays inversion with peak effectiveness. The passive technique, mounting of spike, has also been assessed for its performance using percentage drag reduction and percentage exergy destruction. Here as well both parameters portrayed inverse relation with each other but the spike mounting is found to be responsible for higher percentage exergy destruction than the counter flow injection. Thus, current investigations recommend the use of percentage exergy destruction as a common performance assessment parameter for passive, active and combination drag reduction techniques.

CHAPTER 4

ANALYSIS OF COUNTER FLOW INJECTION TECHNIQUE AT ELEVATED ENTHALPY HYPERSONIC REACTING FLOWS

The current investigations reveals the effect of higher freestream stagnation enthalpy on flow field alteration and wave drag for counter−jet drag reduction technique for a hemispherical object. Results also include the real gas effects on flow field, wave drag and wall heat flux. Further the effect of various flow parameters is observed on surface pressure distribution, surface heat flux and drag force for the hypersonic flow over the hemisphere, using the in house developed perfect gas and non−equilibrium N−S flow solvers. Results revealed that the perfect gas assumption overestimates surface properties and wave drag value. Drag coefficient reduces with freestream total enthalpy (H_o) in the presence of real gas effects. Around 30% drag reduction is observed at H_o=1 MJ/kg for Mach number 5 as compared to no−jet case and this reduction increases at higher freestream total enthalpy for same injection pressure ratio. Higher pressure ratio of the jet results in lower surface pressure and Stanton number on the object which gives lower wave drag.

4.1 Introduction

Various parameters like injection pressure ratio, injection gas, jet to base area ratio are studied by the researchers while understanding the performance of counter flow sonic or supersonic injection. Most of these computational or experimental studies are conducted at lower total temperature conditions of the freestream flow or with perfect gas assumption (constant specific heats with temperature) but space vehicles may encounter relatively higher stagnation enthalpy flows since they cruise at elevated altitude. Hence the current investigations are performed with in house developed perfect gas solver and

non−equilibrium N−S flow solver to explore real gas effects for the accurate solution of the flow field and better prediction of drag reduction for low as well as high enthalpy flows. Such study is expected to reveal the effect of various freestream and jet flow parameters on wall pressure, wall heat flux and wave drag in the presence of reacting hypersonic flow over the hemisphere with counter flow injection from stagnation point. Detalied analysis of the current investigation is presented in the following sections.

4.2 Geometry details and flow conditions

The geometry employed in the current study with its corresponding boundary conditions is same as depicted in Fig 2.4. Details of different variables of freestream and opposing jet, used in the current study, are shown in Table 4.1.

Table 4.1: Different variables of free−stream and opposing jet

Properties	Freestream	Opposing jet
Mach number	5,6	1
Total Pressure (Pa)	275790	275790
Total Enthalpy (MJ/kg)	1,2,4	0.3

4.3 Grid sensitivity test

The sensitivity of present results for same conditions is checked by considering various mesh sizes as mentioned in Table 4.2. Three different grid sizes such as coarse, moderate and fine are selected for the grid independence study. The plots of surface pressure for all grids are shown in Fig 4.1 which shows that the moderate grid (120k cells) has a similar pressure distribution on the body surface as the fine grid (180k cells). Moreover, the wave drag obtained by moderate and fine mesh is almost the same in magnitude (Table 4.2). Hence, moderate mesh size (120k cells) is chosen to carry out all numerical investigations.

Table 4.2: Details of grid size used for grid independence study

Grid	C_d	Difference (%)
Coarse (60k)	0.8950841	0.7
Moderate (120k)	0.887853	0.093
Fine (180k)	0.887963	-

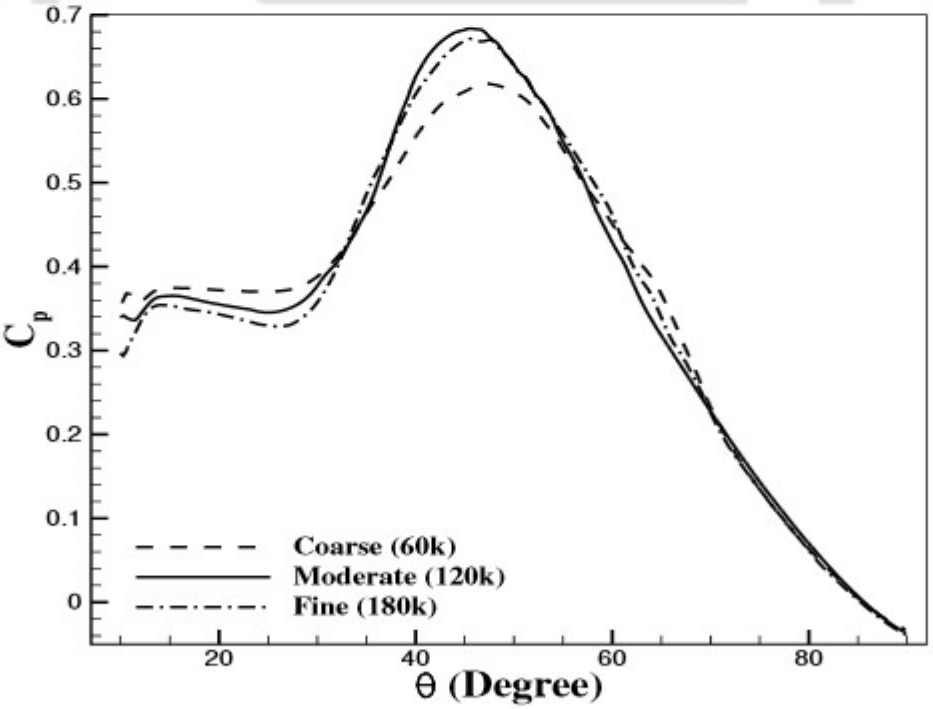

Figure 4.1: Grid Independence Results for different mesh size

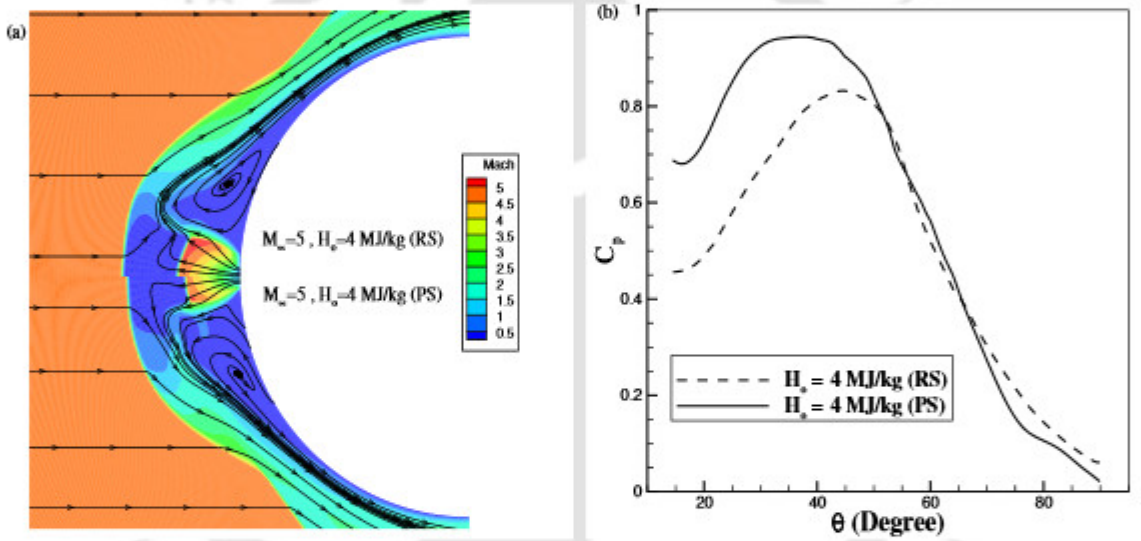

(a) Mach contour of Reacting and Perfect solver for M_∞=5 and H_o=4 MJ/Kg case

(b) Real gas effects on surface pressure variation at M_∞=5 for Reacting and Perfect solver

Figure 4.2: Comparison of reacting and perfect solver

4.4 Results and discussion

4.4.1 Comparison between perfect and real gas models

Initial investigations are performed to study the effect of reacting gas flow over the perfect gas flow. Freestream conditions for this are taken as the hypersonic flow of Mach number 5.0 and freestream static pressure is 521.433 Pa for flow over a hemispherical object of radius $r_b = 25.4$ mm. The freestream stagnation enthalpy (H_0) is considered as 4 MJ/kg for this study. Air having mass fractions of 0.765 and 0.235 for N_2 and O_2 respectively is the working fluid for freestream and jet. Further, the opposing jet diameter ($d_j = 2r_j$) is selected as 2 mm and the pressure ratio (PR) is kept as 1.0 for both perfect and reacting gas conditions. Comparison of the Mach contour for reacting gas solver (RS) and perfect gas solver (PS) is shown in Fig 4.2(a). The reacting condition pushes the bow shock in the upstream direction which leads to the larger shock stand−off distance for reacting solver as compared to the perfect gas solver. These alterations in the flow field reduce the shock angle and make it weaker for the reacting gas case. The Mach disk diameter as well as its shock stand-off distance also increases for the reacting condition as shown in Fig 4.2(a). It is observed that there is 55% increase in the size of Mach disk and 2.54% shift in the location of the Mach disk for the reacting condition. For the same injection pressure ratio (PR), jet expands more due to lower post shock pressure. These flow field alterations along with the shock reconstruction are sufficient to change the predicted pressure on the body for the real gas solver. The comparison of coefficient of pressure (C_p) for the reacting and perfect gas solvers is shown in Fig 4.2(b). The predicted surface pressure for reacting gas is lower due to higher shock stand-off distance and weaker shock as compared to the perfect gas solver. Further, there is a considerable downstream movement of peak pressure location on the surface with reacting flow solver. The calculated wave drag coefficients (C_d) by perfect and reacting gas solvers are 0.66 and 0.54 respectively. Thus, 21.13% higher wave drag is observed by the consideration of the perfect gas model as compared to the reacting gas model. Present non-equilibrium solver handles various dissociation and recombination chemical reactions for the realization of the real gas effect. Since dissociation reactions are endothermic, they lead to decrease in the temperature in the flow field. Thus the calculation of the non-dimensional number such as Stanton number (St), which addresses the surface heat flux, is also part of the present investigations.

The comparison of Stanton number obtained from both solvers is shown in Fig 4.3 for the freestream stagnation enthalpy of 4 MJ/kg. It can be marked that reacting gas solver predicts lower Stanton number at all locations on the object surface as compared to perfect gas results. Trigger of chemical reaction in the flowfield depends on the tem-

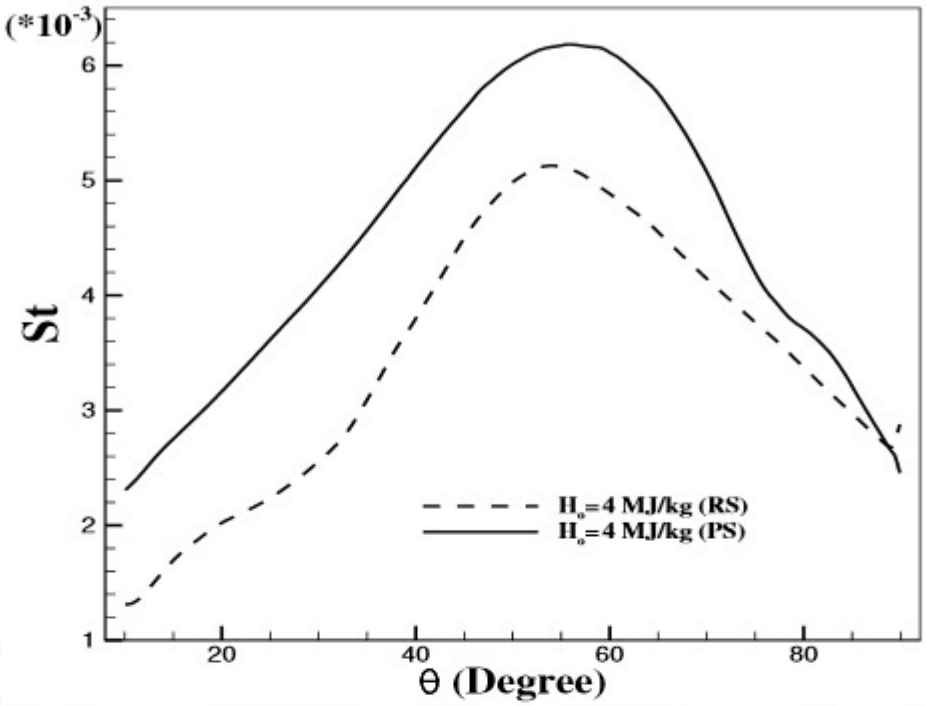

Figure 4.3: Real gas effects on Stanton number variation at M_∞=5 for Reacting and Perfect solver

perature attained by the flow [139]. The molecule of Oxygen gets dissociated when flow field temperature is around 2000 K and for Nitrogen it is 4000 K [140], [141]. In present investigations, comparison between perfect and reacting solver is done for freestream stagnation enthalpy of 4 MJ/kg. This enthalpy corresponds to the freestream total temperature of 4000 K and static temperature of 666.67 K for freestream Mach number of 5. In this temperature range, there is large variation of specific heats and transport properties. Further, this temperature is sufficient to trigger the chemical reactions which has also been observed through simulations [142]. Hence, the predicted results for reacting solver are different than the perfect gas solver for the same freestream conditions. Thus it is essential to account the real gas effects for prediction of wall heat flux and wave drag.

4.4.2 Effect of free−stream stagnation enthalpy

According to the above discussion, it can be found that the consideration of real gas effects leads to the significant alteration on the surface pressure as well as the predicted heat flux as compared to the perfect gas solver. Therfore, it is necessary to study the dynamics of the counter flow jet for various freestream stagnation enthalpy conditions in hypersonic flow regimes using real gas solver. For this, three different stagnation enthalpies (H_o)

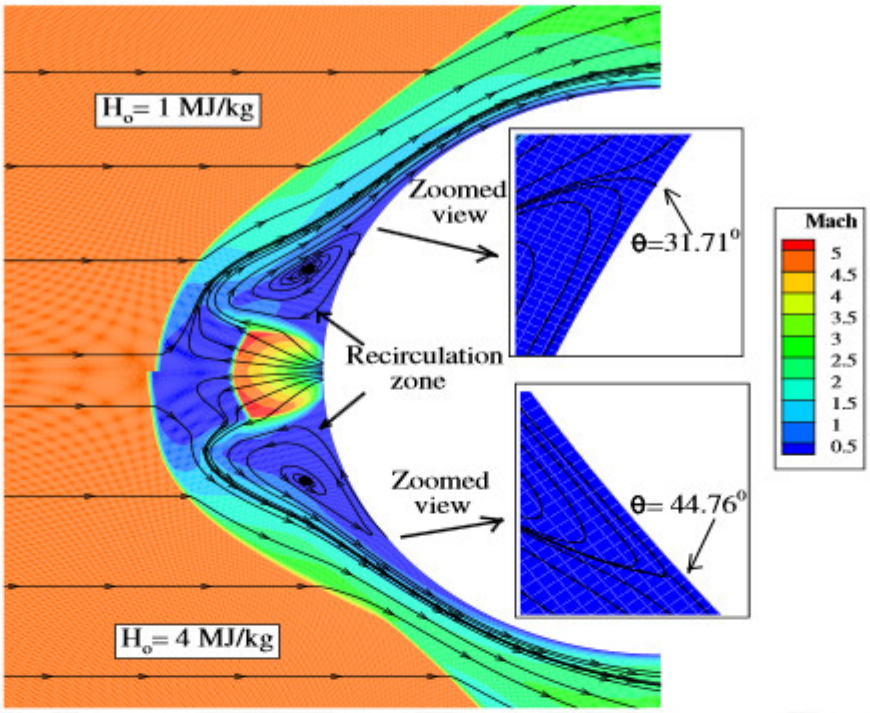

Figure 4.4: Mach contour comparison at various H_o for reacting solver

namely 1 MJ/kg, 2 MJ/kg and 4 MJ/kg, for freestream Mach numbers 5 and 6, are considered for the same geometry. The choice of stagnation enthalpies can be justified from the fact that, H_0 = 1 MJ/kg corresponds to the minor variation in the specific heats and transport properties with no chemical reactions, H_0 = 2 MJ/kg correspond to the strong variation of specific heats and transport properties with no chemical reactions and H_0 = 4 MJ/kg corresponds to the strong temperature dependent properties as well as the chemical reactions. In all these simulations, freestream static pressure is taken as 521.433 Pa which corresponds to high speed flight at around 28 Km altitude. The conditions of the opposing jet such as jet diameter and pressure ratio are kept same as discussed in the above section. Figure 4.4 depicts Mach contour comparison with streamlines for various H_o. The shock stand-off distance for H_o=4 MJ/kg case (38.65 mm) is slightly more as compared to H_o=1 MJ/kg case (38.0 mm) while the Mach disk parameters such as its size and location are almost the same for both conditions. It can be seen in the Mach contours that the streamlines are quite close to each other when the flow crosses the forebody shock in case of 4 MJ/kg simulation. The extension of the recirculation zone is observed for the higher freestream enthalpy case. This extension or size of bubble can be predicted by the flow reattachment point on the blunt surface, as shown in the Fig 4.4, which is migrated in the downstream direction of flow and thus increases the size of the recirculation at H_o= 4 MJ/kg case as compared to the H_0 = 1 MJ/Kg case. However, these alterations in the flow reattachment location are more

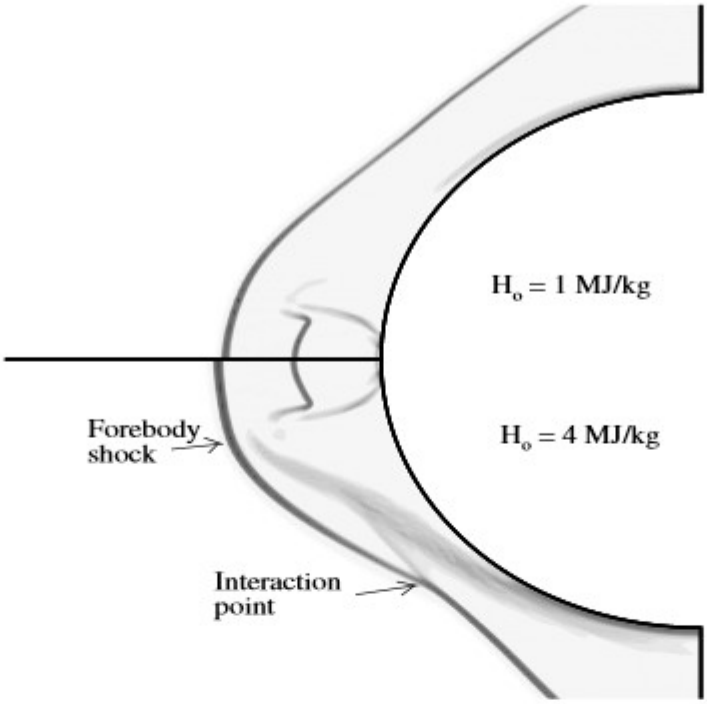

Figure 4.5: Numerical schlieren for $M_\infty = 5$ for reacting solver

clear from schlieren images. Hence, the comparison of numerical schlieren is purposely presented in Fig 4.5 to get better insights of the shock structure. It shows the interaction of forebody shock and reattachment shock. It can be observed, that this shock-shock interaction shows significant variation with increase in H_o as it moves closer to body surface at higher freestream stagnation enthalpy. This shock structure compresses the flow towards body surface resulting in increased surface pressure after flow reattachment location as shown in Fig 4.7(a). It is evident that surface pressure till the reattachment point decreases consistently as we increase the freestream stagnation enthalpy but after the reattachment of the flow, this trend is reversed. Flow reattaches on the surface at around 31^o for H_o=1 MJ/kg case and at 44^o for H_o=4 MJ/kg case. These alterations support larger recirculation zone at higher enthalpy case of 4 MJ/kg. This increased size of the recirculation zone wets extra surface resulting in lower surface pressure upstream of flow reattachment. Surface pressure is also predicted for all enthalpy cases at freestream Mach number of 6 as shown in Fig 4.7(b). But the magnitude of the surface pressure is found to be lowered at every location of the object for the Mach number 6 as compared to the Mach number 5. It can be noted that, there is a significant shift of the peak pressure location in the downstream direction, with the freestream stagnation enthalpy, for the Mach number of 5 while this shift is negligible for M_∞=6. This fact is evident from Fig 4.6 which illustrates similarity in the flow field at higher Mach number. Figure 4.8(a) and Figure 4.8(b) depict Stanton number distribution for various H_o at M_∞=5 and M_∞=6

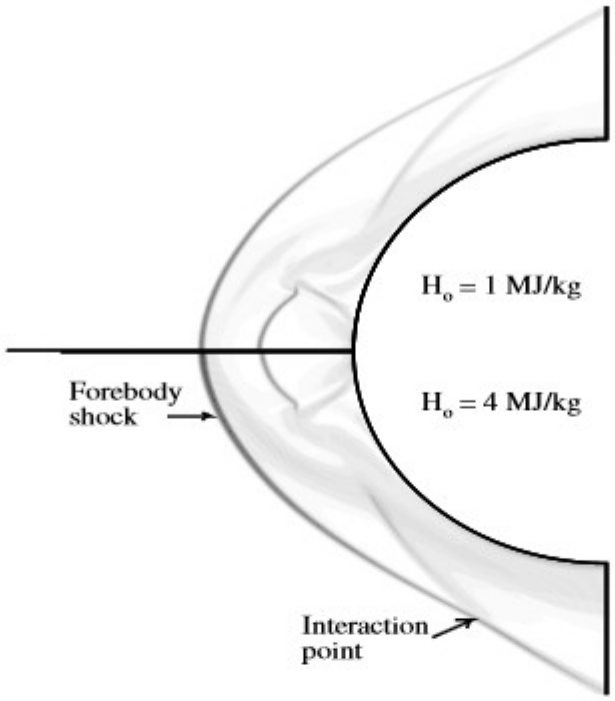

Figure 4.6: Numerical schlieren for $M_\infty = 6$ for reacting solver

respectively. There is reduction in the Stanton number with the freestream stagnation enthalpy for both Mach numbers. However magnitude of this reduction becomes smaller at higher freestream enthalpy conditions. The location of peak Stanton number shifts downstream on the surface for higher H_o. Further, the evaluation of the shock stand-off distance and drag is carried out for all freestream enthalpy conditions as shown in Fig 4.9. It is evident from the figure that there is uniform increment in the shock stand-off distance with the freestream stagnation enthalpy at given freestream Mach number of 5 and injection pressure ratio of PR=1. This leads to a consistent decrease in the computed wave drag. It is observed that there is 1.58% increase in the shock stand-off distance which leads to the 13.17% decrease in the computed drag at higher enthalpy of 4 MJ/Kg as compared to lower enthalpy (1 MJ/Kg). Further investigation at a fixed freestream Mach number of 6 shows that there is minor increase in the shock stand-off distance with freestream stagnation enthalpy. Thus, the magnitude of the predicted drag reduction is also small for this test case as shown in Fig 4.9. Moreover, 0.12% increment in the shock stand-off distance is responsible for 2.81% reduction in the wave drag at freestream Mach number of 6. Details of Mach number effect on the performance of counter jet injection are given in the following subsection.

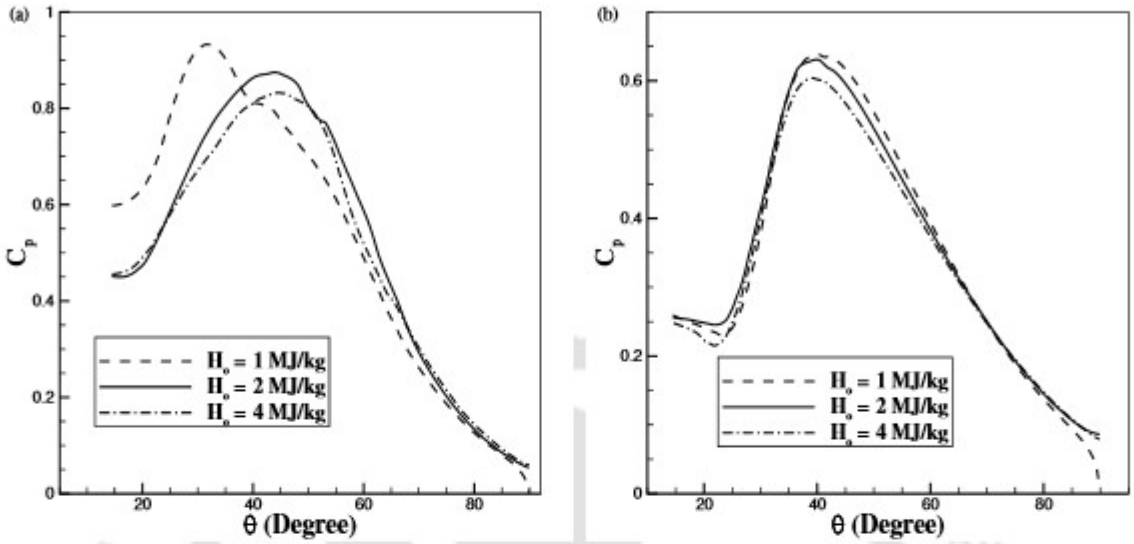

(a) M_∞=5 (b) M_∞=6

Figure 4.7: Effect of H_o on surface pressure variation

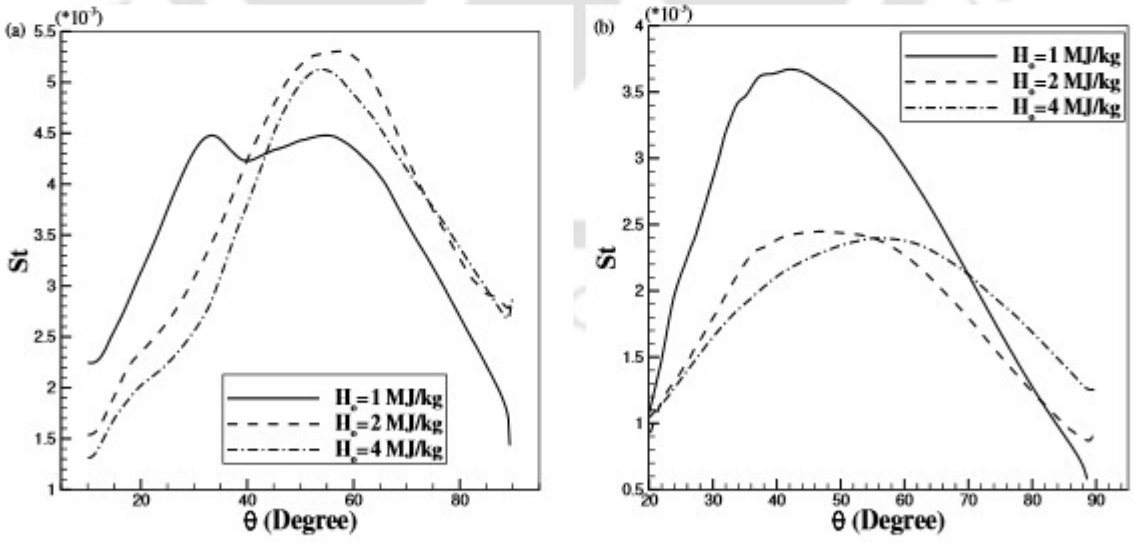

(a) M_∞=5 (b) M_∞=6

Figure 4.8: Effect of H_o on Stanton number variation

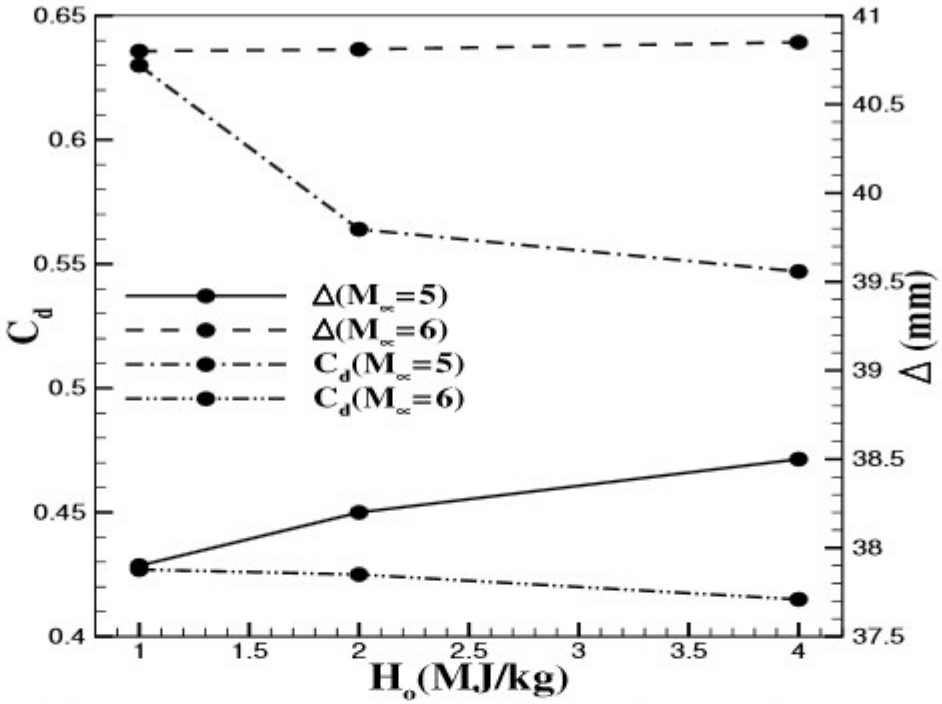

Figure 4.9: Effect of H_o on Drag coefficient and Shock stand-off distance for PR=1

4.4.3 Effect of free−stream Mach number

Freestream Mach number can also have a considerable impact on the flow field alteration and shock reconstruction while using the counter jet drag reduction technique. Because of this, two different freestream Mach number such as M_∞=5 and M_∞=6 are considered herein. The diameter and pressure ratio (PR) of the opposing jet are kept constant as 2 mm and 1 respectively while the freestream stagnation enthalpy is kept constant as 1.0 MJ/kg. Initially, simulations are carried out to compare the flow field alterations due to these Mach number which is shown in Fig 4.10(a). It can be noted that the shock stand-off distance is higher for the higher freestream Mach number at the same freestream enthalpy and injection conditions. There is 7.65% increment in the shock stand-off distance for unit increment in the freestream Mach number. As the jet expands more in the low-pressure region, for M_∞=6 case, the reattachment point shifts more in the downstream direction and as a result, the size of the recirculation zone is increased. For M_∞=6, Mach disk diameter gets enhanced by 94.4% while the location of Mach disk gets amplified by 8% as compared to M_∞=5 case. Surface pressure distribution for various freestream Mach numbers for no opposing jet or jet-OFF (PR=0) and with opposing jet or jet-ON (PR=1) is depicted in Fig 4.10(b) for fixed freestream enthalpy of 1.0 MJ/kg. It can be seen that the magnitude of surface pressure, for the jet-OFF case, is almost same for any freestream Mach number. However, the magnitude of surface pressure on

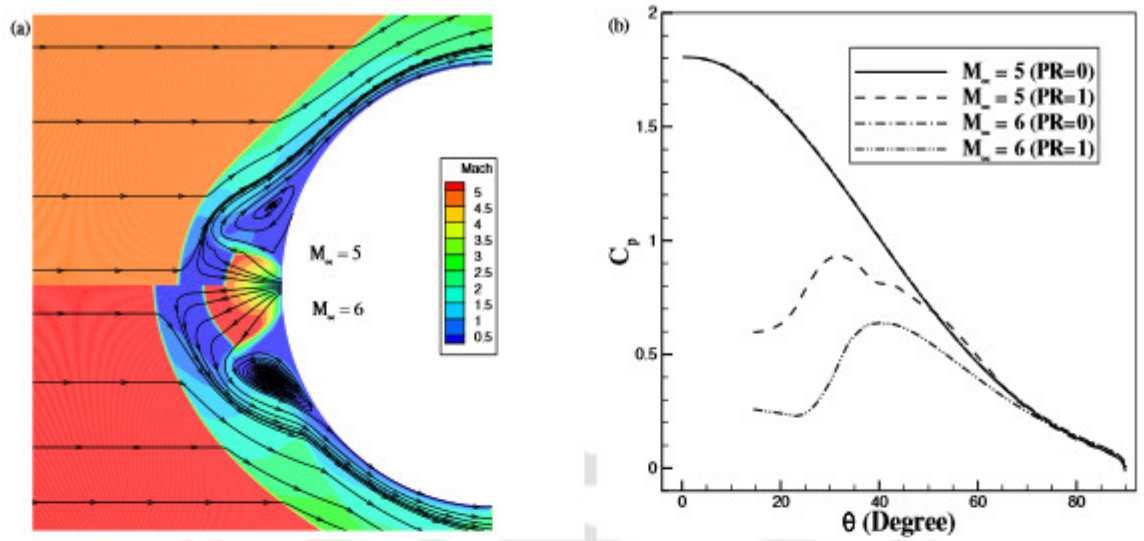

(a) Mach contour comparison for H_o=1 MJ/kg cases

(b) Surface pressure variation for no−jet and PR=1 cases

Figure 4.10: Effect of M_∞

the body is lower at higher Mach number (M_∞=6) as compared to lower Mach number (M_∞=5) for the jet with PR=1. Here, rapid increase in the surface pressure is observed till the reattachment location and after this reduction is followed. Around 33% reduction in the peak value of the surface pressure is noted for higher freestream Mach number as compared to lower Mach number. Also, the location of peak surface pressure shifts in the downstream direction of the flow field at a higher Mach number. The location of maximum or peak pressure, for M_∞=6 case, is found at 40^o while it is found at 30^o for M_∞=5 case. These alterations in surface pressure change the drag force on body. Figure 4.9 shows that the computed wave drag for higher Mach number is lower for given freestream stagnation enthalpy and vice-a-versa. There is 29.21% and 52.3% reduction in the wave drag at M_∞=5 and M_∞=6 for freestream stagnation enthalpy of 1.0 MJ/kg respectively. It can be concluded that counter flow injection at higher freestream Mach number is more efficient (32.22%) in wave drag reduction as compared to lower freestream Mach number. Further, the Stanton number is also computed for each case mentioned above which is shown in Fig 4.11. Here, the magnitude of heat flux on the object surface is higher at increased freestream Mach number for no injection condition (PR=0) while it reduces sharply when the opposing jet is turned on and this reduction becomes larger at higher freestream Mach number. The peak Stanton number is found at 30^o and 40^o for M_∞=5 and M_∞=6 respectively. Thus counter jet injection is more effective in reducing the surface heat flux also at higher freestream Mach numbers.

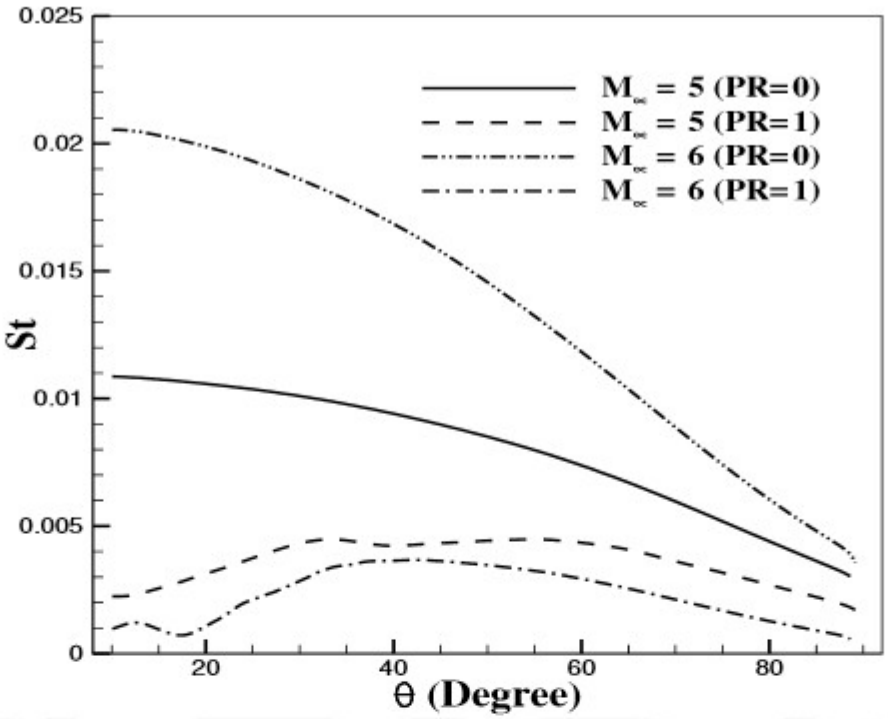

Figure 4.11: Effect of M_∞ on Stanton number variation for no−jet and PR=1 cases

4.4.4 Effect of jet pressure ratio

The parametric studies are further extended to examine the effect of jet pressure ratio on the wave drag and heat flux reduction on the object with in house reacting flow solver. Three different values of jet pressure ratio (PR) are considered here which are 1, 1.3 and 1.4 respectively. These pressure ratios are investigated for fixed Mach number (M_∞=5) and freestream stagnation enthalpy (H_o=1 MJ/kg). Simulations for various jet pressure ratios show that higher jet pressure makes the jet more under expanded which gives comparatively larger Mach disk height as shown in Fig 4.12(a). Further, the location of the triple point and Mach disk shift in the downstream direction of the flow field. For the same jet Mach number, higher jet pressure results in increased mass flow rate through the jet which pushes the detached shock wave away from the body surface. This phenomenon leads to higher shock stand-off distance for the increased pressure of the jet. This reconstruction leads to formation of a larger recirculation zone which is responsible for lower surface properties on the object. The computed surface pressure for all pressure ratios of the jet is shown in Fig 4.12(b). It can be seen that surface pressure decreases steeply when the jet pressure ratio rises from 1 to 1.3 while this reduction becomes smaller when the pressure ratio rises from 1.3 to 1.4. This alteration in the magnitude of surface pressure changes the computed drag on the object as shown in Fig 4.13. It is evident from the figure that there is a sharp decrement in the drag values when the opposing

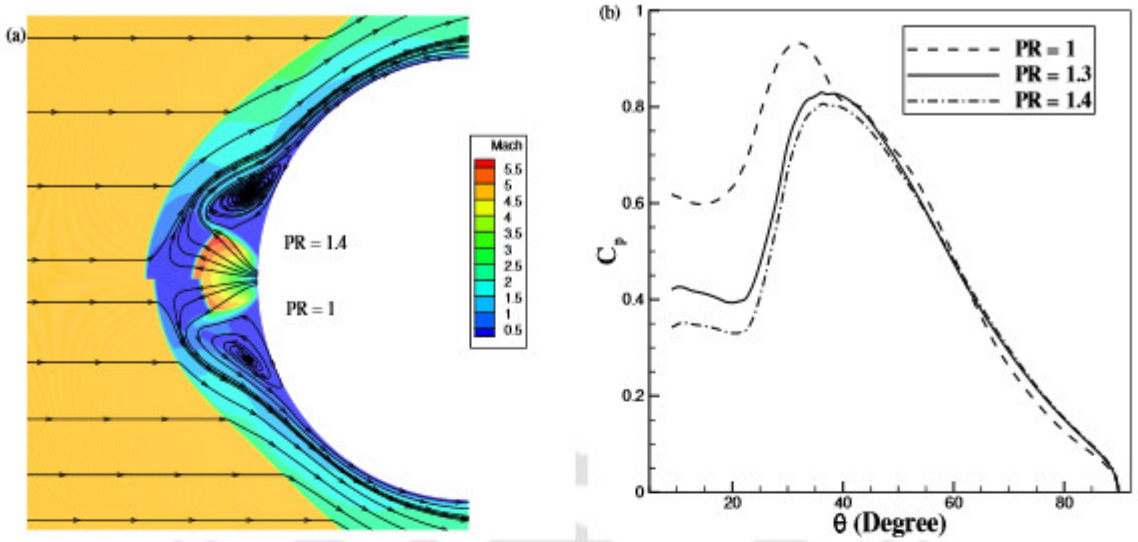

(a) Mach contour of M_∞=5 and H_o=1 MJ/Kg case for PR=1 and PR=1.4

(b) Effect of pressure ratio on surface pressure distribution at H_o=1 MJ/Kg

Figure 4.12: Effect of jet pressure ratio

jet is turned ON but this decrement becomes gradual at higher jet pressure ratio. It can be mentioned that there is 31.53% increment in the shock stand-off distance which is responsible for 39.32% reduction in the wave drag for higher pressure ratio of 1.4 at H_o=1 MJ/kg. Higher freestream stagnation enthalpy (4 MJ/kg) is also considered for the wave drag alteration with different pressure ratio conditions (Fig 4.13). The magnitude of drag force is lower at the higher stagnation enthalpy condition for same pressure ratio of the jet. Here, 34.07% increment in the shock stand-off distance is responsible for 61.21% reduction in the wave drag at H_o=4 MJ/kg for a jet pressure ratio of 1.4. Further, the Stanton number is also calculated and plotted as shown in Fig 4.14 for all pressure ratios at fixed freestream stagnation enthalpy of 1.0 MJ/kg. The Stanton number also reduces sharply with the jet pressure ratio but the magnitude of this reduction becomes smaller at higher jet pressure ratios. The position of the peak Stanton number also shifts in the downstream direction for higher jet pressure ratios.

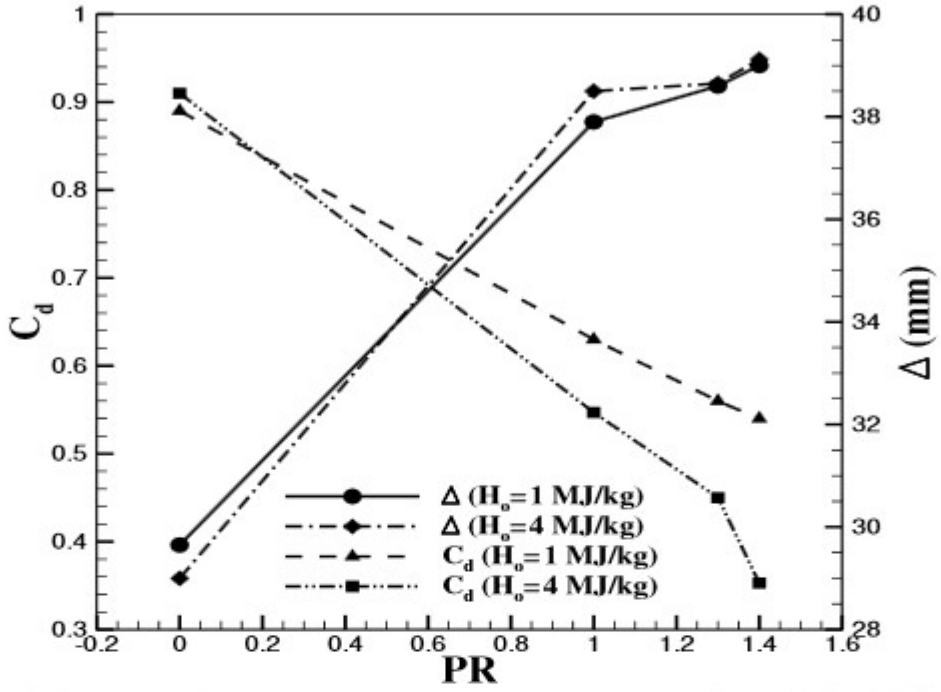

Figure 4.13: Effect of PR on Drag coefficient and Shock stand-off distance for M_∞=5

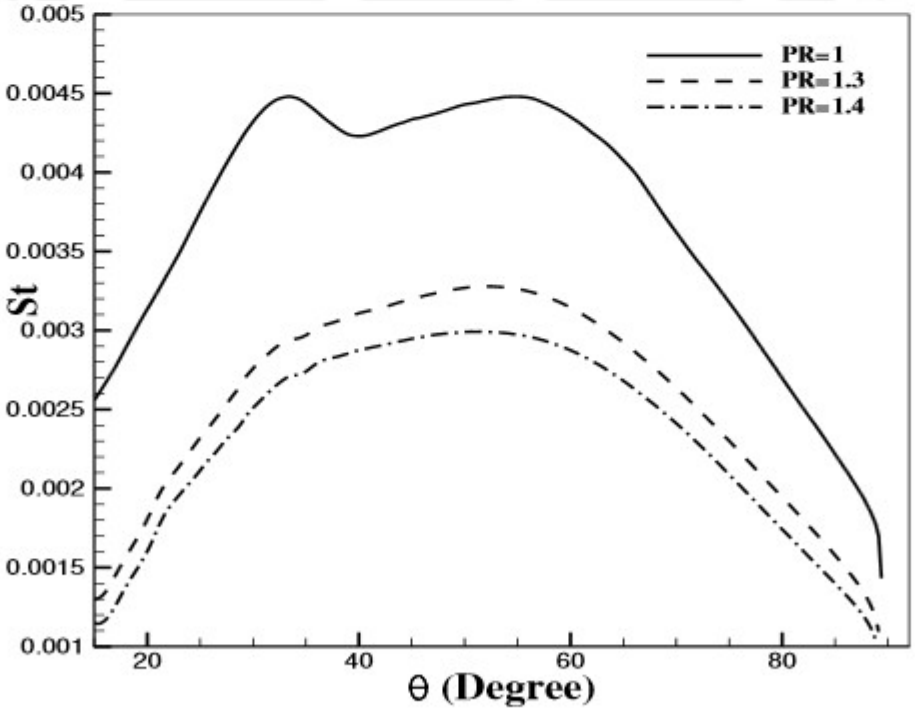

Figure 4.14: Effect of pressure ratio on Stanton number distribution at H_o=1 MJ/Kg

4.5 Conclusions

Present study is undertaken to demonstrate the flow field alterations and drag reduction phenomena using counter flowing jet in the reacting hypersonic flows. Perfect gas assumption is found to overestimate surface properties. Further the reacting gas model predicts higher shock stand-off distance and Mach disk parameters as compared to perfect gas model for same free-stream and jet conditions. Thus computed surface pressure, wave drag and heat flux are found to be lower for the reacting gas model as compared to the perfect gas model. Further, simulations with different freestream stagnation enthalpies show that the surface pressure continuously decreases with the freestream stagnation enthalpy for any freestream Mach number. This leads to decrease in the wave drag by 13.17% at higher free-stream stagnation enthalpy (4 MJ/kg) as compared to the lower one (1 MJ/kg). The computed Stanton number also decreases for higher inlet stagnation enthalpy cases. About 29% and 52% reduction in the wave drag is obtained for M_∞=5 and M_∞=6 at free-stream stagnation enthalpy of 1.0 MJ/kg respectively in the presence of real gas flow. For a given freestream Mach number, higher pressure ratio of the jet gives larger recirculation zone and lower surface pressure as compared to the lower pressure ratio for every fixed stagnation enthalpy condition. Therefore the wave drag force and surface heat flux reduction are higher at an elevated pressure ratio of the counter-jet. Further, the performance of the jet pressure is more effective at higher freestream stagnation enthalpy as compared to lower enthalpy conditions. Thus counter flow injection is found more effective at higher enthalpies in reducing the drag force and wall heat flux.

CHAPTER 5

THERMODYNAMIC ANALYSIS FOR OPPOSING JET TECHNIQUE IN HYPERSONIC REACTING FLOWS

In the current study, thermodynamic analysis which includes variation of entropy generation rate, exergy destruction and drag analysis for opposing jet technique considering real gas effects is examined. In this context, high entahlpy hypersonic flow over the hemispherical body in the presence of real gas reactions is studied. Numerical simulations are performed for different flow and geometrical parameters of jet and freestream to examine their impact on flow field, drag reduction, exergy destruction and entropy generation rate. Results revealed that freestream parameters have lesser effect on drag values and flow field but there is monotonic variation in entropy generation rate and exergy destruction for constant momentum ratio of the jet. For given momentum ratio, jet parameters give almost linear reduction in entropy generation rate and exergy destuction while minor alterations in flow field and drag values are observed. Linear reduction in drag force, sharp rise in entropy generation rate and exergy destruction are obtained with momentum ratio of the jet. Jet momentum ratio is only major governing parameter for the extent of jet penetration in the freestream flow which restructures the shock wave and recirculation zone resulting in significant drag reduction and flow field alterations for hypersonic flows.

5.1 Introduction

It can be noted from the literature that researchers have performed computations and experiments to achieve better reduction in drag force and surface heat load with counter-jet injection. Specifically most of the computations dealt with lower total temperature conditions of the freestream flow or with perfect gas assumption. Further, different

governing parameters of counter-jet injection like pressure ratio, jet Mach number, jet diameter etc. have been investigated separately for their influence on the performance. But, Yisheng [143] carried out simulations for drag reduction with opposing jet technique and a new parameter R_{PA} was introduced which is the combinination of jet pressure ratio and area ratio. Results showed that same shock wave position and wave drag coefficient can be obtained with same R_{PA}. So it was proposed to represent the intensity of opposing jet and access it's performance on flow field and drag foces. Desai et al [131] tested the effectiveness of momentum ratio (ratio of jet momentum to the freestream momentum) for counterflowing jet based drag reduction technique in supersonic flows. They proved that momentum ratio has a vital role in shock restructring and hence drag reduction for wide range of freestream and jet parameters. For constant momentum ratio, freestream and jet parameters were noted to have minor impact on drag coefficient values. Hence they recommended momentum ratio as a unique governing parameter for counter flow injection technique. However this universal parameter was tesed only for supersonic flows. Moreover it is also desirable to understand it's universality in the presence of real gas effects. Also, formation of shock during high speed flows ahead of the object can be viewed as highly irreversible process. Thus, it is important to determine the dependence of this irreversibility on different flow parameters so that the extent of this irreversibility can be minimized for optimum flow conditions. Therfore in the current study, thermodynamic analysis of the opposing jet based drag reduction technique is carried out considering real gas effects at elevated freestream stagnation enthalpy. In this context, hypersonic flow over hemispherical object is considered and the effect of momentum ratio is analysed by altering various governing parameters. Results are presented in terms of wave drag, entropy generation rate and exergy destruction as discussed in the following sections.

5.2 Geometry description and flow parameters

The model used in the current study is same as shown in Fig 5.1. Structred grid is used to discretize the computational domain for all the cases investigated with fine mesh near the wall to accurately capture the flow and wall properties. The number of grid points are 350 in the perpendicular direction of body surface and 345 along the body surface. Diameter of the hemispherical body (d_b) is 50.8 mm while opposing jet diameter (d_j) is varied as 2 mm, 4 mm, 6 mm respectively. Momentum ratio (R_{ma}) in the current study is varied as 0.0173, 0.052, 0.0866, 0.1213 respectively. Stagnation pressure of the freestream is kept constant as 275790 Pa. Air is used as working fluid for both freestream and opposing jet consisting 0.765 and 0.235 mass fractions of N_2 and O_2 respectively. Table 5.1 shows the values of different parameters of freestream and opposing jet used in the current study.

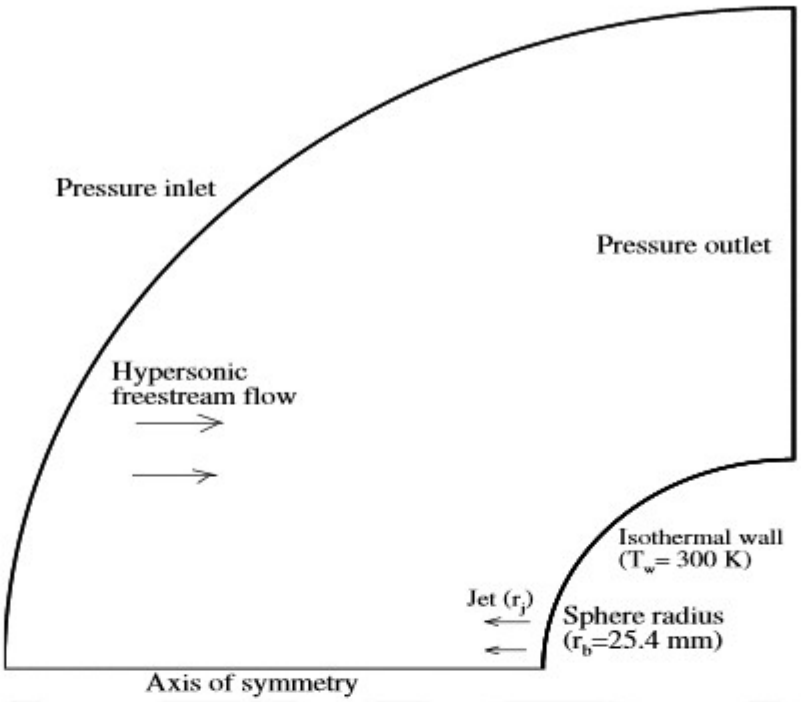

Figure 5.1: Model geometry with its computational domain and boundary conditions

Table 5.1: Different variables of free−stream and opposing jet

Properties	Freestream (Air)	Opposing jet (Air)
Mach Number	5,6,7,8	1,1.1,1.2,1.3
Stagnation enthalpy (MJ/kg)	1,2,3	0.3

5.3 Grid independence study

Different mesh sizes used for grid independence study are shown in Table 5.2. While discretizing the domain with these meshes, care has been taken to have sufficient refinement near the wall and also in the regions of shock. As a result, computationally obtained drag coefficients for all these grids are compared in Table 5.2. Difference in C_d value is less than 0.1% after the moderate grid size of 120k cells. So this mesh size (120k cells) is chosen to carry out all numerical investigations.

Table 5.2: C_d for various mesh size

Grid	Nodes in x and y direction	Cells	C_d	Difference(%)
Coarse	250×240	60k	0.8950841	0.7
Moderate	350×345	120k	0.8887853	0.093
Fine	430×420	180k	0.887963	-

5.4 Results and discussion

5.4.1 Effect of free−stream Mach number

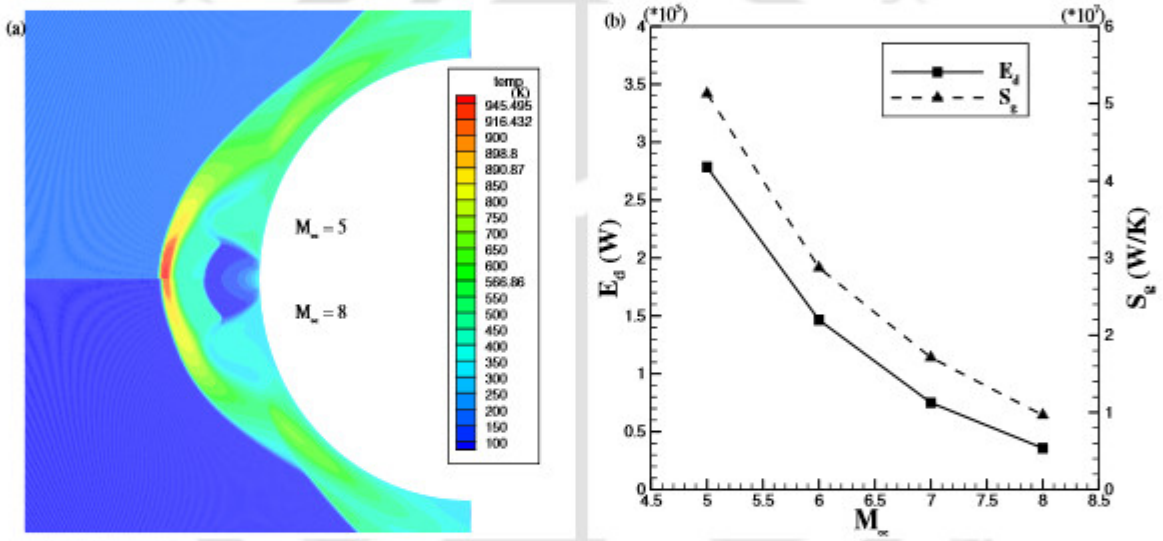

(a) Temperature contour comparison

(b) E_d and $\dot{S}_g$ variation

Figure 5.2: Effect of M_∞ on flow field and theromdynamic parameters

In the first set of simulations, effect of various free−stream Mach number on flow field and associated parameters for constant momentum ratio (R_{ma} = 0.01733) is studied. Figure 5.2(a) elucidates comparison of temperature field for M_∞=5 and M_∞=8 while exergy destruction and entropy generation changes are shown in Fig 5.2(b). It is evident that region of higher temperature at post shock location shrinks in size at higher M_∞ resulting in lowering of entropy increase of system which gives lower entropy generation rate and exergy destruction at higher M_∞. From the Table 5.3, it is evident that, for given momentum ratio, drag force doesn't vary much with freestream Mach number. Minor alterations in the flow field and bow shock structure are observed with the freestream Mach number. There is almost no change in shock stand-off distance and Mach disk location with the freestream Mach number as shown in pressure countour in Fig 5.3(a). As the shock stand-off distance is almost the same, there is not much difference in the

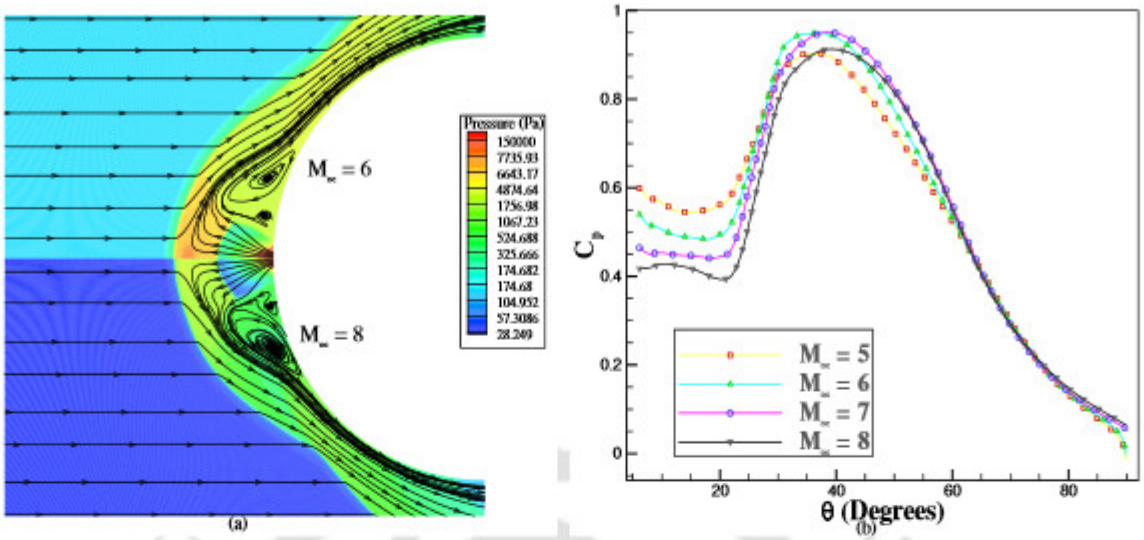

(a) Pressure contour comparison

(b) Surface pressure variation

Figure 5.3: Effect of freestream Mach number

bow shock strength and the shock structures is also identical. All these flow features result in almost same drag values. Maximum difference of only 3.57% is obtained in drag reduction when freestream Mach number is increased from 6 to 8. Corresponding surface pressure distribution for all M_∞ cases is shown in Fig 5.3(b) and it is found that surface pressure reduces with M_∞ upto peak pressure location after which there is not much difference in surface pressure distribution for all the cases. As indicated in Table 5.3, peak surface pressure location is found at almost 37^o for M_∞=6 while it is found at 40^o for M_∞=8. So there is small shift in peak surface pressure location resulting in comparetively enlarged recirculation zone which gives lower surface pressure on the body upto peak pressure point at higher M_∞.

Table 5.3: Drag variation with free−stream Mach number

$\mathbf{M_\infty}$	$\mathbf{C_d}$	$\frac{\Delta}{R}$	θ_{pmin}	θ_{pmax}	$\mathbf{l}_{md}(mm)$	$\mathbf{d}_{md}(mm)$
5	0.631	1.48	14.22	37.45	6.6	8
6	0.643	1.472	17.88	37	6.68	8
7	0.643	1.468	18.14	38.5	6.69	8.4
8	0.62	1.472	20.23	39.28	6.69	8.4

5.4.2 Effect of free−stream stagnation enthalpy

Through this set of simulations, flow field variation and associated drag, exergy and entropy changes with the freestream stagnation enthalpy for constant momentum ratio

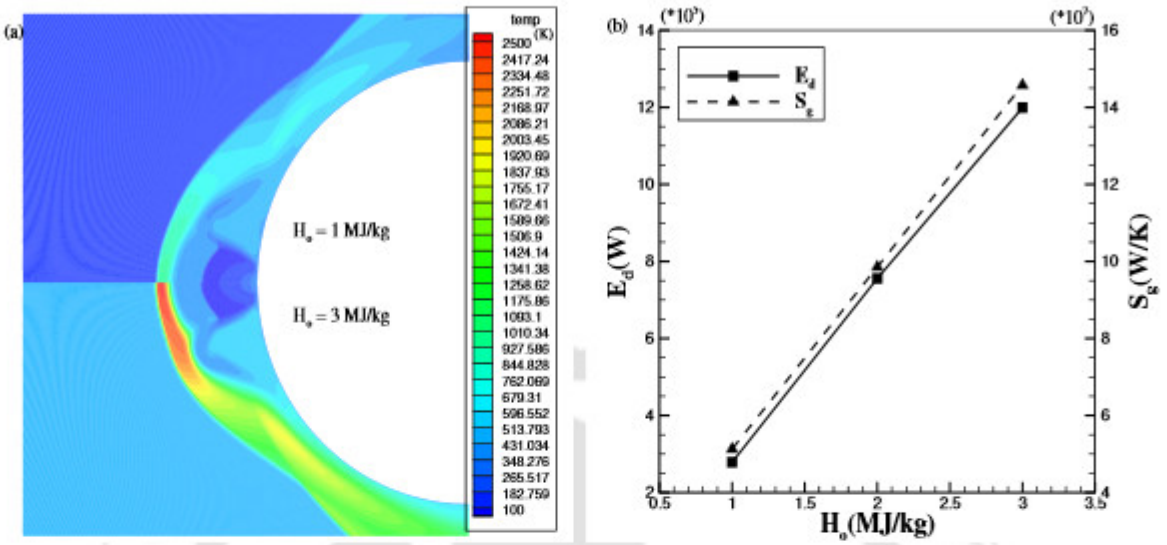

(a) Temperature contour comparison (b) E_d and $\dot{S}_g$ variation

Figure 5.4: Effect of freestream stagnation enthalpy on flow field and thermodynamic parameters

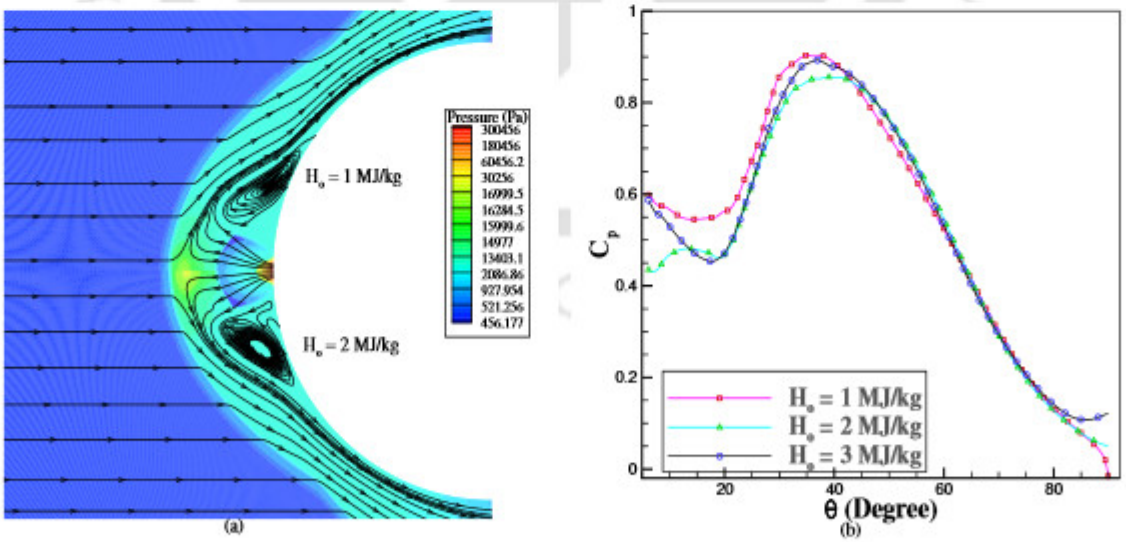

(a) Pressure contour comparison (b) Surface pressure variation

Figure 5.5: Effect of freestream stagnation enthalpy

(R_{ma} = 0.01733) is studied. Figure 5.4(a) depicts temperature contour comparison for H_o= 1 MJ/kg and H_o= 3 MJ/kg cases while exergy destruction and entropy generation changes are shown in Fig 5.4(b). It can be observed that there is a prominent higher temperature region at post shock location for higher H_o case which results in higher entropy rise. Thus, entropy generation rate and exergy destruction show significant increment at higher H_o. But for given momentum ratio (R_{ma} = 0.01733), drag values show minor variation with H_o as shown in Table 5.4. Only 1.74% drag reduction is observed when the freestream stagnation enthalpy is increased from 1 MJ/kg to 3 MJ/kg. There is almost no change in Mach disk parameters and shock stand-off distance with H_o as shown in Fig 5.5(a). Surface pressure distribution for all H_o cases is depicted in Fig 5.5(b).

Table 5.4: Drag variation with free−stream total enthalpy

$\mathbf{H}_o(MJ/kg)$	$\mathbf{C}_d$	$\frac{\Delta}{R}$	θ_{pmin}	θ_{pmax}	$\mathbf{l}_{md}(mm)$	$\mathbf{d}_{md}(mm)$
1	0.631	1.48	14.22	37.45	6.6	8
2	0.611	1.474	18.92	39.28	6.5	8
3	0.62	1.484	17.62	36.93	6.7	8

Basically, the minimum surface pressure point shifts 3.4^o downstream and peak surface pressure location shifts almost 0.52^o upstream resulting in smaller recirculation zone for H_o=3 MJ/kg case. There is small difference in surface pressure distribution upto 20^o location after which there is insignificant difference in surface pressure. Peak surface pressure point for H_o=1 MJ/kg case is found at 37.45^o while it is found at almost 40^o for H_o=2 MJ/kg case.

5.4.3 Effect of jet Mach number

Table 5.5: Drag variation with jet Mach number

$\mathbf{M}_j$	$\mathbf{C}_d$	$\frac{\Delta}{R}$	θ_{pmin}	θ_{pmax}	$\mathbf{l}_{md}(mm)$	$\mathbf{d}_{md}(mm)$
1	0.631	1.48	14.22	37.45	6.6	8
1.1	0.645	1.468	13.7	37.45	6.4	7.4
1.2	0.622	1.458	22.84	38.76	6.2	7.4
1.3	0.653	1.448	18.4	37.71	6.1	6.8

With one set of simulations, effect of various jet Mach number at given momentum ratio (R_{ma} = 0.01733) is studied on the flow field alterations and associated drag reduc-

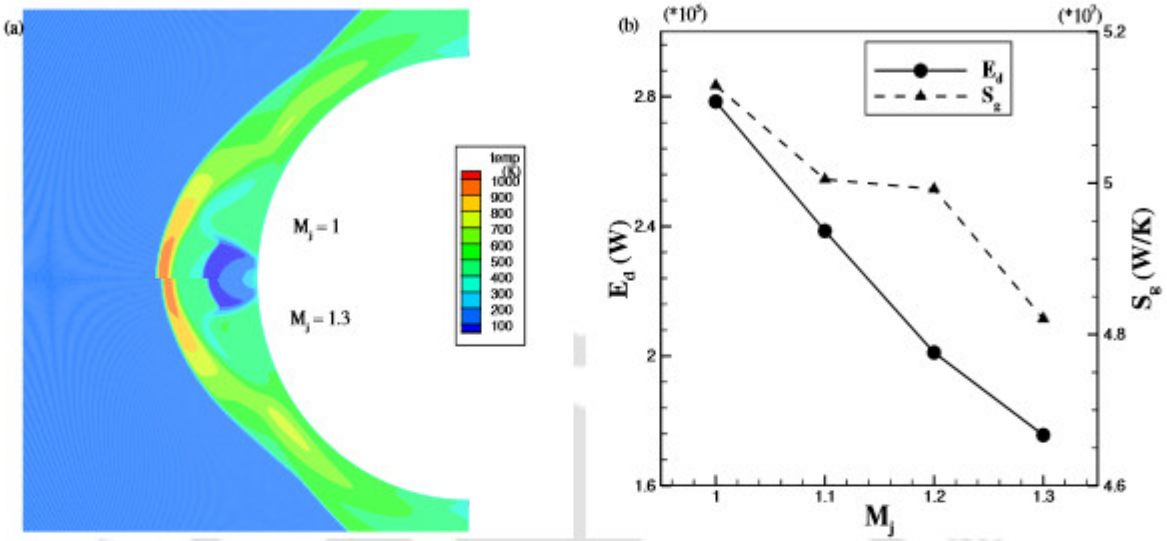

(a) Temperature contour comparison (b) E_d and $\dot{S}_g$ variation

Figure 5.6: Effect of jet Mach number on flow field and thermodynamic parameters

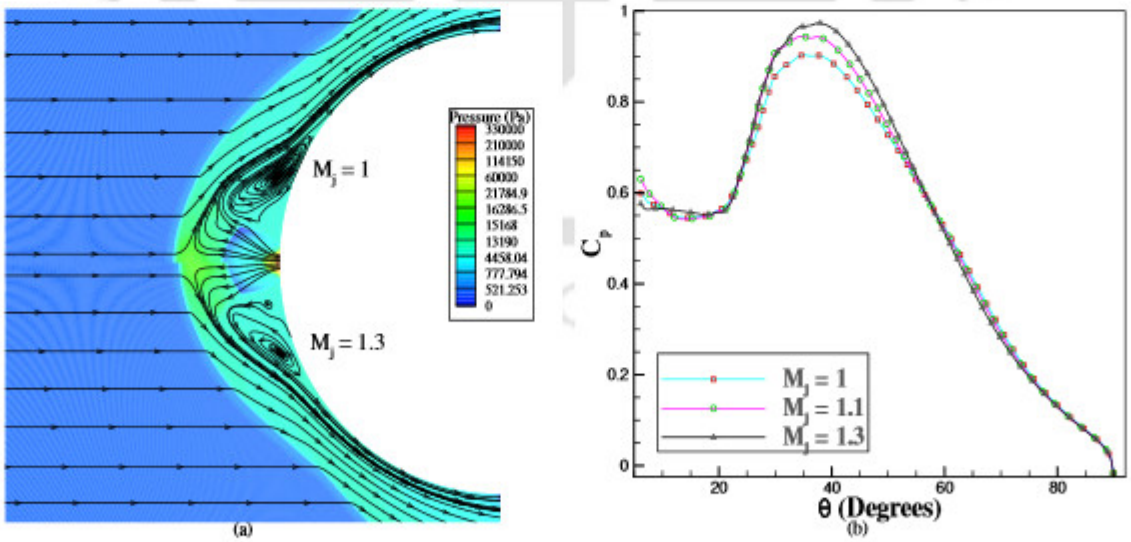

(a) Pressure contour comparison (b) Surface pressure variation

Figure 5.7: Effect of jet Mach number

tion, exergy and entropy variation are recorded. Figure 5.6(a) elucidates comparison of temperature field for M_j=1 and M_j=1.3 while exergy destruction and entropy generation changes are shown in Fig 5.6(b). It is seen that temperature field at post shock location is almost similar for both the cases resulting in minor reduction of entropy increase of system with M_j which gives slightly lower entropy generation rate and exergy destruction at higher jet Mach number. From the Table 5.5, it is seen that for given momentum ratio (R_{ma} = 0.01733), drag value shows minor variation with jet Mach number. Maximum of 5% drag increment is observed when the jet Mach number is increased from 1.2 to 1.3. Shock stand-off distance and Mach disk size for M_j=1 case is found to be only 2.21% and 1.7% larger as compared to M_j=1.3 case respectively. From Eq 2.48, increasing jet Mach number for constant jet momentum ratio results in lowering of jet pressure ratio which gives lesser shock stand-off distance for higher jet Mach number. This makes shock weaker for M_j=1 case as depicted in Fig 5.7(a). Thus, slightly higher surface pressure and drag value for M_j=1.3 case is obtained as compared to M_j=1 case. 3.48% drag increment is obtained when jet Mach number is increased from 1 to 1.3. Higher pressure area at post shock location for M_j=1.3 case is almost similar as comapared to M_j=1 case. Surface pressure distribution for M_j=1.3 is seen to be higher as compared to M_j=1 case near the peak surface pressure location while there is negligible change in surface pressure distribution at other locations on the body surface as shown in Fig 5.7(b). As indicated in Table 5.5, peak surface pressure location is found at almost 38^o for all the cases giving almost negligible change in recirculation zone for all the jet Mach number.

5.4.4 Effect of jet diameter

In the next set of simulations, the influence of jet diameter on drag reduction, exergy and entropy changes is observed for fixed momentum ratio (R_{ma} = 0.01733). Figure 5.8(a) depicts temperature contour comparison for d_j= 2 mm and d_j= 6 mm cases while exergy destruction and entropy generation changes are shown in Fig 5.8(b). It can be observed that higher temperature region at post shock location shows almost no variation with d_j resulting in minor reduction in entropy rise of system with d_j. Thus, entropy generation rate and exergy destruction shows decrement at higher d_j. From Table 5.6, it is observed that for fixed momentum ratio (R_{ma} = 0.01733), drag value shows slight changes with jet diameter. Maximum of 1.8% drag increment is observed when the jet diameter is increased from 2 mm to 4 mm. Pressure contours for d_j= 4 mm and d_j= 6 mm are compared in Fig 5.9(a). It is evident that shock stand-off distance and Mach disk location from the stagnation point for d_j=4 mm case are comparetively larger as compared to d_j=6 mm case. For constant jet momentum ratio, increasing jet diameter results in lowered jet pressure ratio as cleared from Eq 2.48 which gives shorter shock

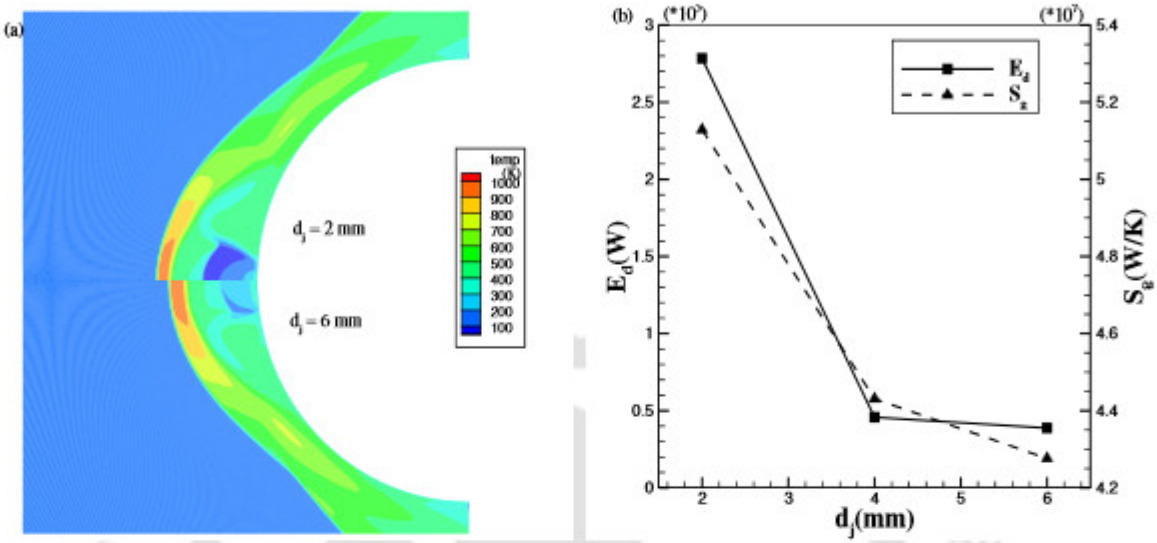

(a) Temperature contour comparison (b) E_d and $\dot{S}_g$ variation

Figure 5.8: Effect of jet diameter on flow field and thermodynamic parameters

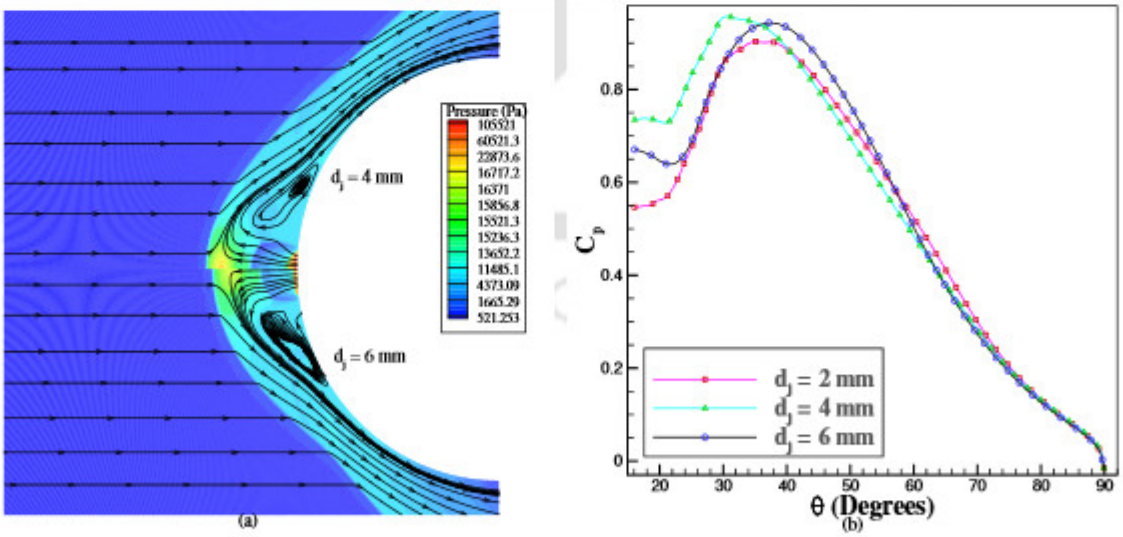

(a) Pressure contour comparison (b) Surface pressure variation

Figure 5.9: Effect of jet diameter

stand-off distance for higher jet diameter. Also, higher pressure zone after the shock is larger in size for d_j=4 mm case but this zone stands much away from the body surface as compared to d_j=6 mm case resulting in lower surface pressure and wave drag on the body for d_j=6 mm case. Surface pressure variation for d_j=6 mm is lower as compared to d_j=4 mm as depicted in Fig 5.9(b) upto reattachment point location after which the trend becomes reverse upto 60^o location while it is the same after that location. Peak surface pressure location shifts downstream on the body surface with the increase in jet diameter resulting in slightly larger recirculation area for higher jet diameter.

Table 5.6: Drag variation with jet diameter

$\mathbf{d}_j$	$\mathbf{C}_d$	$\frac{\Delta}{R}$	θ_{pmin}	θ_{pmax}	$\mathbf{l}_{md}(mm)$	$\mathbf{d}_{md}(mm)$
2	0.631	1.48	14.22	37.45	6.6	8
4	0.655	1.453	12.4	37.45	5.8	7.6
6	0.643	1.421	21.53	37.45	5.4	7.4

5.4.5 Effect of jet momentum ratio

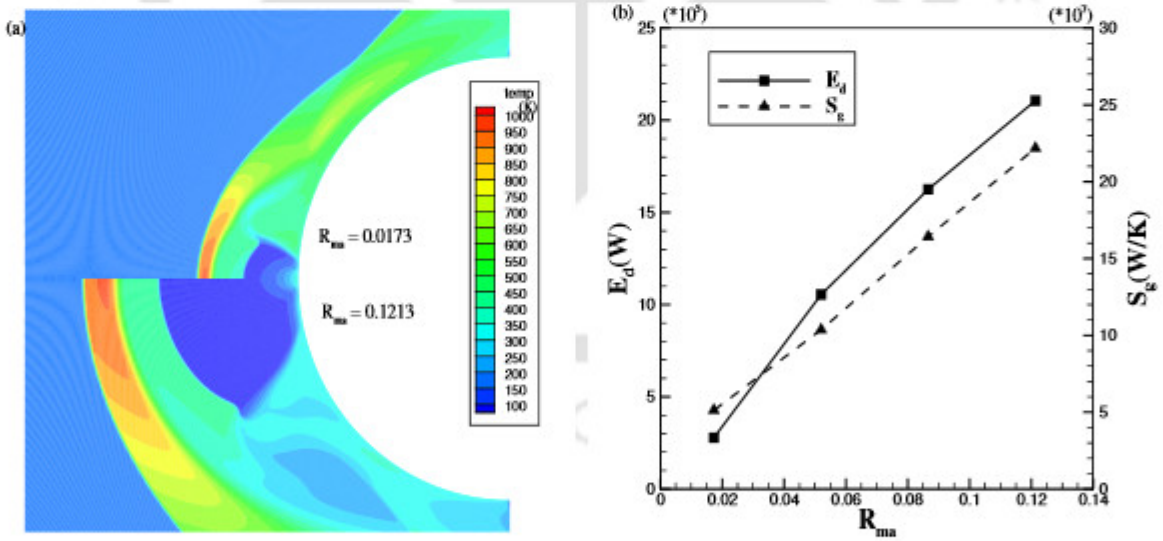

(a) Temperature contour comparison

(b) E_d and $\dot{S}_g$ variation

Figure 5.10: Effect of jet momentum ratio on flow field and thermodynamic parameters

In the final set of simulations, the effect of jet momentum ratio is studied on the flow field and shock alterations while its influence on exergy, entropy and drag reduction is observed. Figure 5.10(a) depicts temperature contour comparison for R_{ma}= 0.0173 and R_{ma}= 0.1213 cases while exergy destruction and entropy generation changes are shown

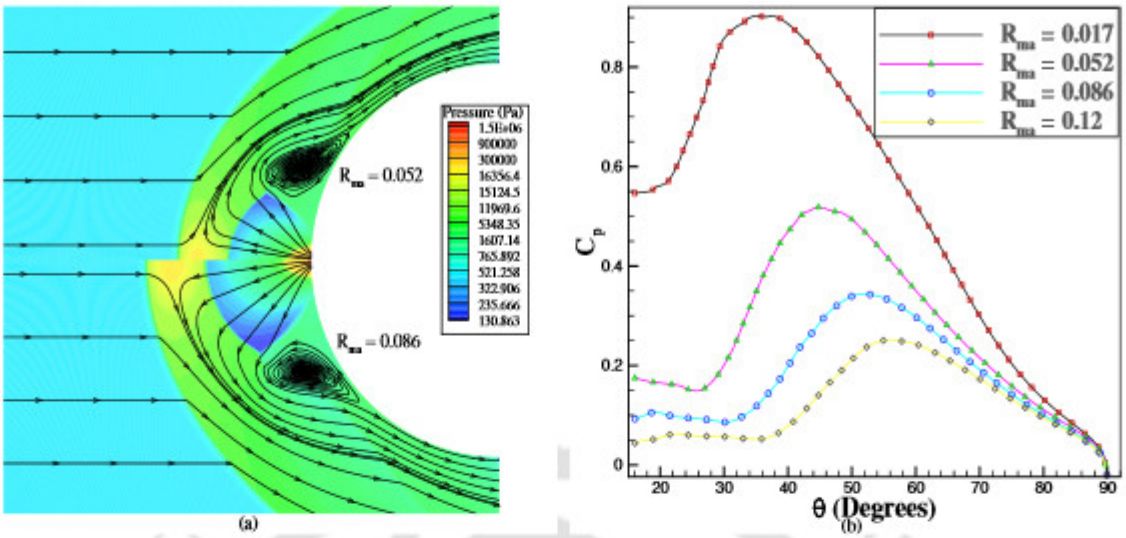

(a) Pressure contour comparison

(b) Surface pressure variation

Figure 5.11: Effect of jet momentum ratio

in Fig 5.10(b). It is seen that higher temperature region at post shock location grows in transverse direction significantly and the area covered by it increases in horizontal direction as well with R_{ma} resulting in huge increment in entropy rise of system which gives significant increase in entropy generation rate and exergy destruction at higher jet momentum ratio. Table 5.7 shows drag and flow field parameters variation with jet momentum ratio. Nearly 64% drag reduction is obtained when jet momentum ratio is increased from 0.0173 to 0.1213. Shock location and Mach disk parameters rises drastically with jet momentum ratio as shown in Fig 5.11(a) resulting in larger recirculation area and thus surface pressure on the body lowers and associated drag values also reduces for higher jet momentum ratio. From the Fig 5.11(b), it is observed that surface pressure sharply reduces with the increase in momentum ratio of jet and this reduction is seen throughout the whole surface of the body. Almost 36.54% reduction is seen in peak pressure value when the jet momentum ratio is increased from 0.052 to 0.086. Significant shift is observed in peak surface pressure location at higher jet momentum ratio. Peak surface pressure point shifts almost 20^o downstream on the body surface and 36.21% increment in shock stand-off distance is seen when jet momentum ratio is increased from 0.0173 to 0.1213.

Table 5.7: Drag variation with jet momentum ratio

$\mathbf{R}_{ma}$	$\mathbf{C}_d$	$\frac{\Delta}{R}$	θ_{pmin}	θ_{pmax}	$\mathbf{l}_{md}(mm)$	$\mathbf{d}_{md}(mm)$
0.0173	0.631	1.48	14.22	37.45	6.6	8
0.052	0.347	1.71	25.7	44.76	11.2	17.4
0.0866	0.262	1.874	29.88	52.07	14.28	24
0.1213	0.227	2.016	35.1	56	16.73	29.6

5.5 Conclusions

In the current study, detailed computational investigations of hypersonic flow over hemispherical body in the presence of real gas effects is considered. Also, the influence of various freestream and jet parameters is checked on the drag force of the body, exergy destruction and entropy generation rate across the shock wave. The major conclusions drawn from the current numerical study are summmarized as follows:

Exergy destruction and entropy generation rate show significant variation with freestream parameters while they gives linear reduction with jet parameters. Rapid increase in exergy destruction and entropy generation rate is seen with jet momentum ratio. It is observed that for constant jet momentum ratio, drag coefficient shows minor changes with freestream and jet parameters. Shock structure and Mach disk parameters also show negligible variation with freestream and jet parameters for given momentum ratio. Simulations revealed that for constant momentum ratio, the maximum difference obtained in drag values is only 3.76% when freestream Mach number is increased from 5 to 8 whereas for jet Mach number variation from 1 to 1.3, the largest difference in drag value observed is 4.8% but drag values gives almost 64% reduction when momentum ratio is increased from 0.0173 to 0.1213. Larger shock stand-off distance results in lower surface pressure and lower drag coefficient but on the other hand it gives increment in the region covered by higher temperature zone at post shock location resulting in higher exergy destruction and entropy generation rate, making the shock formation process much more irreversible. Moreover, the proposed thermodynamic parameters and drag coefficient show opposite variation with given freestream or jet parameter for constant jet momentum ratio. Thus, exergy destruction and entropy generation rate can be used as a performance accessing parameter along with drag coefficient for opposing jet technique. Shock structure, flow field and Mach disk parameters portras significant alterations with jet momentum ratio. Jet momentum ratio is found to be the only major governing parameter for the extent of jet penetration in the freestream flow which restructures the shock wave and recircula-

tion zone resulting in significant drag reduction and flow field alterations for hypersonic reacting flows as well.

CHAPTER 6

DRAG AND ENTROPY GENERATION ANALYSIS FOR OPPOSING JET AND FORWARD FACING CAVITY COMBINATORIAL TECHNIQUE IN PRESENCE OF REAL GAS REACTIONS

In the current study, real gas effects (non−equlibrium flow) on surface pressure and flow field are analysed for the combinatorial technique (opposing jet and cavity) for high enthalpy hypersonic flow over the blunt body by means of in house developed N−S flow solvers. A new thermodynamic parameter named entropy generation rate is proposed which can be used as a tool to analyze the performance of any drag reduction technique. Drag variation and entropy generation rate are also noted for different flow conditions and associated flow field alterations are examined. Results reveal that perfect gas assumption over−estimates the surface pressure and wave drag as the surface pressure is much lower when the real gas effects are considered. Significant flow field and shock alterations are observed when the real gas reactions are taken into consideration. Coefficient of drag and entropy generation rate vary in almost similar manner for different flow conditions. Introduction of cavity reduces the surface pressure, drag and entropy generation rate but significant reduction in these parameters is noted when the opposing jet is turned ON. For given jet pressure ratio, opposing jet technique predicts lower drag and entropy generation rate as compared to combinatorial technique.

6.1 Introduction

It is evident from the literature that most of the computational studies for opposing jet or combination of jet and cavity based drag reduction technique are conducted with perfect gas assumption. Moreover, it is essential to determine whether introduction of forward facing cavity in combination with opposing jet can effectively reduce wave drag as compared to only opposing jet case when real gas effects are taken into consideration. Hence the current investigation is centered on the real gas effects on the flow field alterations and surface pressure distribution obtained from the computational results for the opposing jet, forward facing cavity and their combination techniques. Further, the effect of real gas reactions are also observed on wave drag and newly proposed thermodynamic parameter named entropy generation rate which can be used as a tool along with coefficient of drag to access the performance of opposing jet, forward facing cavity and combination of jet with cavity techniques. Initially, flow features like shock stand-off distance, Mach disk parameters are analysed for sonic injection considering the perfect gas assumption. Then the real gas flow solver is employed to assess the alteration in these flow features in the presence of chemical reactions. Full detailed findings of the current study is explained in following sections.

6.2 Geometry details and flow conditions

Figure 6.1 shows the blunt body used in the current study with its appropriate boundary conditions and it also shows the counter−flowing jet originating from the cavity core opposing the primary hypersonic flow. Diameter of the blunt body (D_n=$2R_n$) and curvature radius (R) are 51 mm and 15 mm respectively. Length of cavity (L) and radius of cavity (r) are 24 mm and 6 mm respectively making L/D ratio of cavity as 4 while radius of jet (r_j) is 2 mm. Structred grid is used to discretize the computational domain for all the cases investigated with fine mesh near the wall to accurately capture the flow properties at the wall. Distance X is measured from the tip of the cavity (meeting point of the cavity and curved surface). Table 6.1 shows the values of different parameters of freestream and opposing jet used in the current study.

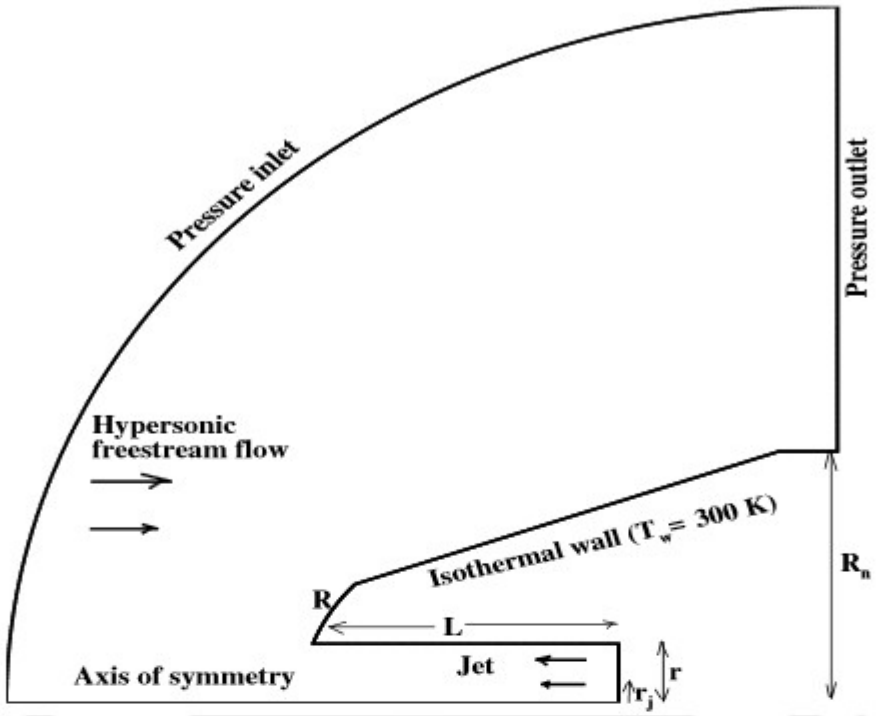

Figure 6.1: Model geometry with its computational domain and boundary conditions

Table 6.1: Flow conditions of free−stream and opposing jet

Properties	Freestream (Air)	Opposing jet (Air)
Mach Number	8	1
Static Pressure (kPa)	1940	194,388,776
Stagnation enthalpy (MJ/kg)	1,2	0.3

6.3 Validation for cavity based studies

The validation studies are carried out to compare the surface heat flux as predicted by present reacting solver with the experimental results of Saravanan [89]. The model used for this test case is a blunt nose shaped cylindrical object. It has bluntness radius of 15 mm and half cone angle of 20.5 degree [89]. The freestream static pressure, temperature and Mach number are taken as 205 Pa, 143 K and 8 respectively [89]. The obtained surface heat flux by present computations and corresponding experiment [89] are compared in Fig 6.2(a) and Fig 6.2(b) for cavity L/D ratio of 2 and 4 respectively. It can be observed that the Stanton number distribution over the surface from the present computation matches well with the measured experimental values for both L/D ratio. Same non-equilibrium computational solver was also validated by (Kumar et al [67] and Patil et al [144]) for the analysis of viscous hypersonic flows.

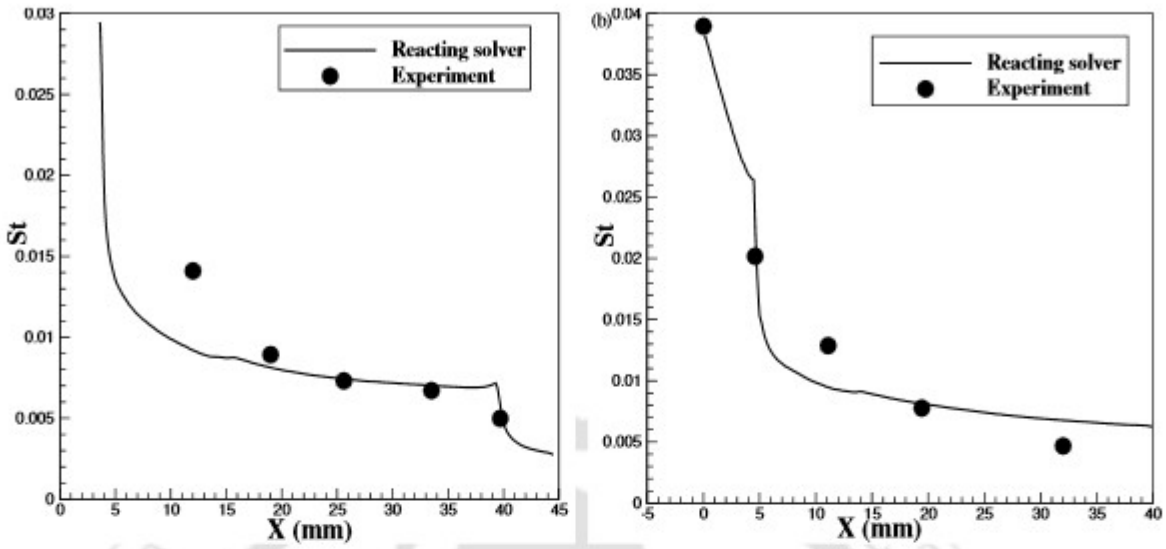

(a) L/D=2 (b) L/D=4

Figure 6.2: Comparison of non−dimensional surface heat flux of current computation with experimental results

6.4 Grid independence study

Different mesh sizes used for grid independence study of no-cavity case with their drag values is shown in Table 6.2. Variation in C_d value becomes less than 0.04% after 210k mesh size. So mesh size of 210k cells is chosen to carry out all numerical investigations for the current reacting and perfect solvers. Reacting solver (RS) calculates the inviscid flux considering the real gas reactions while perfect solver (PS) neglects the real gas reactions while calculating the inviscid flux. Measured experimental [89] drag coefficient for given case is C_d=0.41.

Table 6.2: C_d value for various mesh sizes

Grid	Cells	C_d	Difference(%)
1	70k	0.475	0.19
2	140k	0.4741	0.08
3	210k	0.4737	0.04
4	280k	0.4735	-

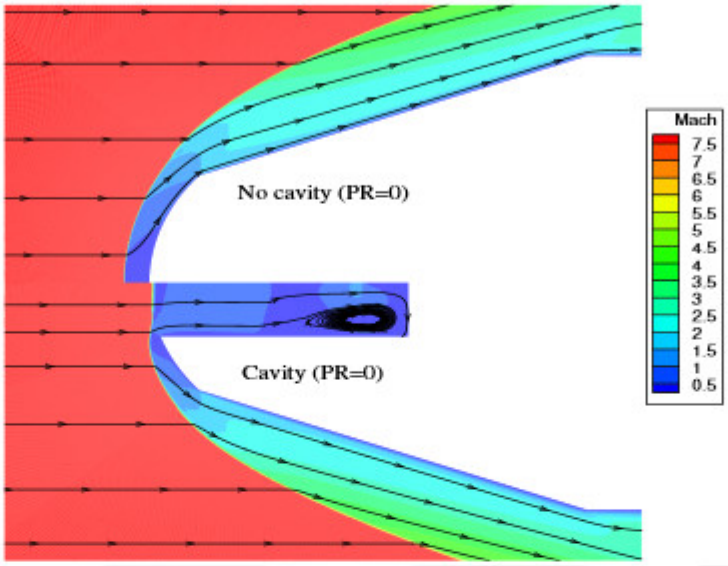

Figure 6.3: Comparison of Mach contour for cavity and no-cavity case at H_o=2 MJ/kg

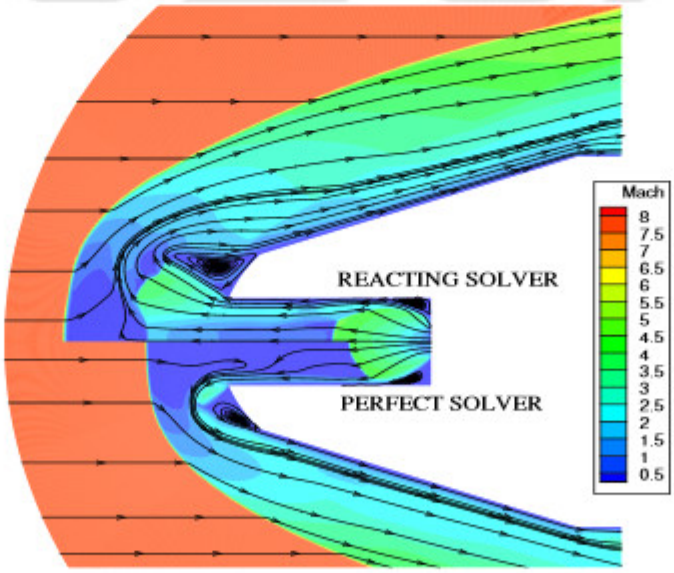

Figure 6.4: Comparison of Mach contour for reacting and perfect solver at H_o=1 MJ/kg

6.5 Results and discussion

6.5.1 Flow field

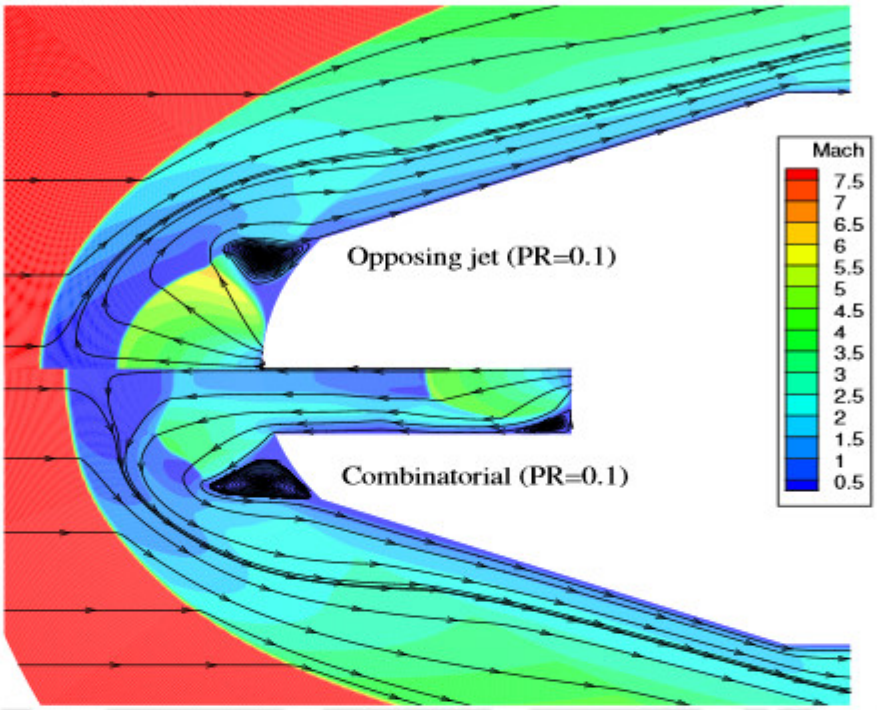

Figure 6.5: Comparison of Mach contour for opposing jet and combinatorial case at H_o=2 MJ/kg

Comparison of Mach contour for no-cavity and with cavity case is shown in Fig 6.3. Shock wave moves closer to the body with the introduction of cavity and small recirculation region is formed inside the cavity. Shock structure is almost similar for both the cases. Comparison of flow field with streamlines for reacting and perfect solver at H_o= 1 MJ/kg is depicted in Fig 6.4. Opposing jet originating from cavity core clearly forms two Mach disks for reacting solver while jet flow forms single Mach disk for perfect solver. Reacting conditions form one Mach disk at the jet origin and its size is larger as compared to Mach disk of perfect solver while other is formed at cavity lip in order to balance the pressure of jet and pressure of freestream flow at post shock location. Reacting solver predicts larger shock stand-off distance making the detached shock much more weaker as compared to perfect solver case. Interface is formed when the jet flow meets freestream flow and this interface formation takes place outside the cavity for reacting solver while it is formed inside the caity for perfect solver. Jet flow seprates from the body at the cavity lip and again reattaches to the body surface due to high speed freestream flow forming recirculation region near the cavity tip. Size of this region is much larger for reacting solver as compared to perfect solver case as the reattachment

point is found at 3.554 mm for reacting solver while it is found at 3.397 mm for perfect solver. Reattachment shock wave is also formed near the flow reattachment point. Mach contour for opposing jet and combination of jet with cavity for PR=0.1 is compared in Fig 6.5. Larger shock stand-off distance is observed for opposing jet technique as it forms bigger Mach disk near the cavity lip as compared to combinatorial technique. As opposing jet gives higher Mach disk diameter, big recirculation region is formed as compared to combinatorial technique due to downstream shift of reattachment point on the body surface. Reattachment point is found at 4.297 mm for opposing jet while it is found at 3.554 mm for combinatorial technique. Comparison of temperature contour for opposing jet and combinatorial technique at H_o= 2 MJ/kg is depicted in Fig 6.6. It is evident that area covered by higher temperature at the post shock location is larger for combinatorial technique as it is stretched more in transverse direction.

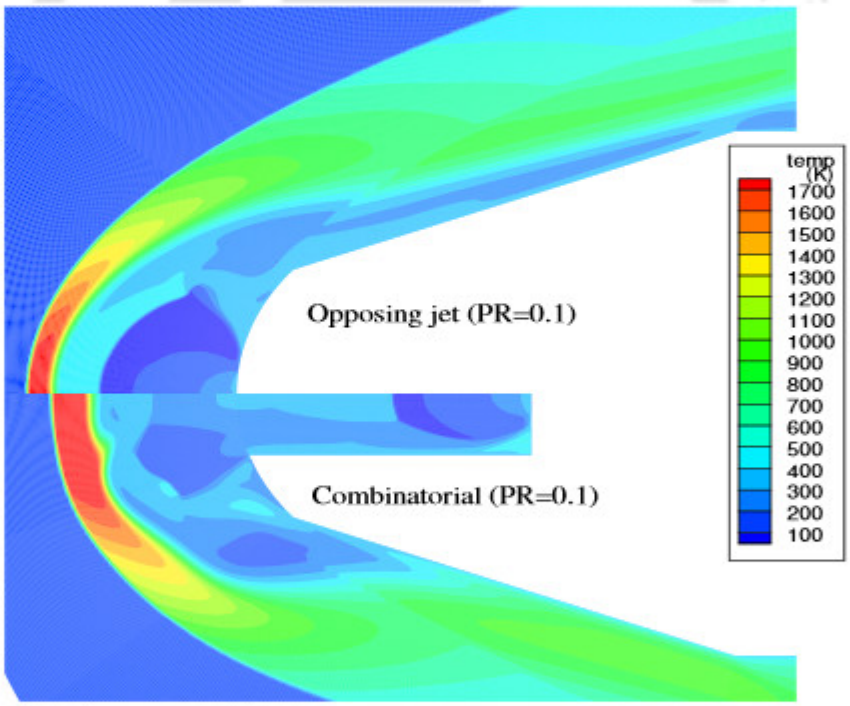

Figure 6.6: Comparison of temperature contour for opposing jet and combinatorial case at H_o=2 MJ/kg

6.5.2 Surface pressure

Surface pressure distribution for reacting and perfect solver at H_o= 1 MJ/kg is depicted in Fig 6.7. It is evident that perfect gas assumption overestimates surface pressure as the real gas reactions predicts much lower surface pressure. Perfect solver gives much higher surface pressure near the reattachment point while reacting solver gives almost constant

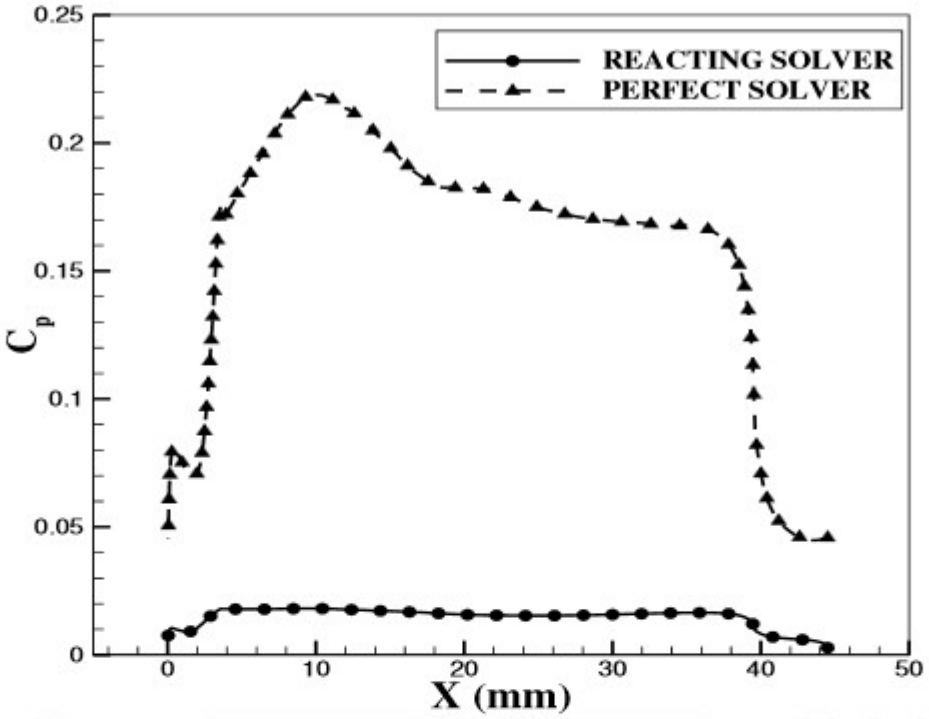

Figure 6.7: Surface pressure for reacting and perfect solver at H_o=1 MJ/kg

surface pressure over the entire body surface. Drag coefficient is calculated based on surface pressure for both solvers in order to analyse the effect of real gas reactions. Value of C_d for perfect solver is 0.29 while it is 0.2 for reacting solver. Reacting condition predicts much larger expansion of jet flow inside as well as outside the cavity resulting in bigger Mach disk and recirculation zone ahead of the body. Also, shock shifts more away from the body for reacting solver resulting in lowering of surface pressure and wave drag on the body surface. Figure 6.8 shows the comparison of surface pressure for different techniques at jet PR=0.1 and H_o=2 MJ/kg. Forward facing cavity gives much higher surface pressure over the curved surface of body as the shock stands closer to the body as shown in Fig 6.5 while surface pressure is significantly reduced when the opposing jet is turned on. As opposing jet technique predicts larger shock stand-off distance and bigger Mach disk, it gives slightly lower surface pressure as compared to combinatorial technique over the entire surface of the body.

6.5.3 Drag and entropy generation rate

Figure 6.9 elucidates drag and entropy generation rate variation with jet pressure ratio for opposing jet and combinatorial technique at H_o=2 MJ/kg. Drag and entropy generation rate vary in almost similar manner as they show monotonic variation with jet pressure ratio. Opposing jet technique predicts lower drag and entropy generation rate

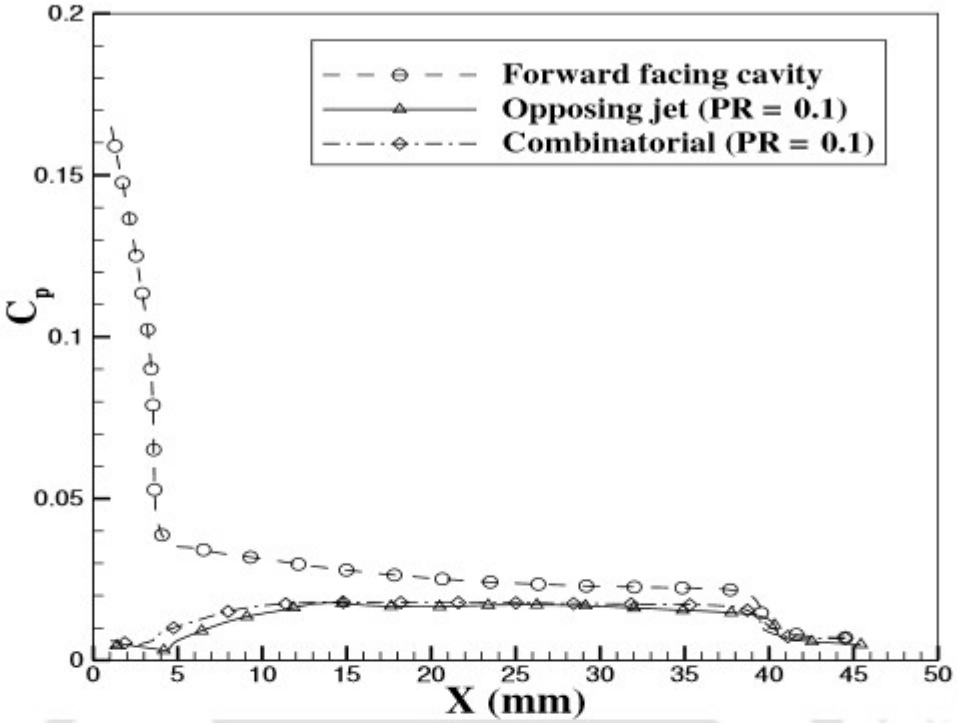

Figure 6.8: Surface pressure comparison for various techniques at H_o=2 MJ/kg

Table 6.3: Drag and entropy generation rate for various techniques

Technique	$\dot{S}_g$($\times 10^8$ W/K)	C_d
Blunt body	1.89	0.474
Forward facing cavity	1.67	0.4
Opposing jet (PR=0.1)	2.91	0.163
Combinatorial (PR=0.1)	3.17	0.21

as compared to combinatorial technique for all pressure ratios. Higher temperature gives higher entropy values and the area of higher temperature at post shock location is larger for combinatorial technique as shown in Fig 6.6 resulting in larger entropy increase of the system. Combinatorial technique shows steeper increment in entropy generation rate with jet pressure ratio. Drag and entropy generation values for various techniques are tabulated in Table 6.3. Introduction of cavity reduces drag and entropy generation rate while drag reduces further with the introduction of jet inside the cavity but this jet flow results in much higher entropy generation rate as the jet flow increases the entropy rise of the system.

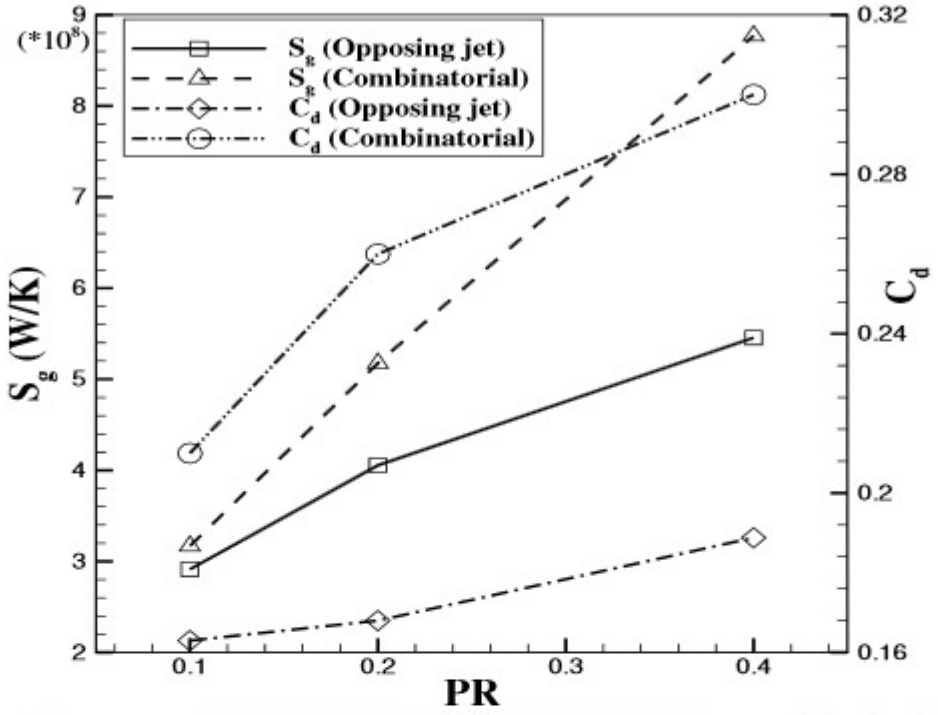

Figure 6.9: Entropy generation rate and drag for opposing jet and combinatorial technique

6.6 Conclusions

In the current study, detailed computational investigations of flow field, surface pressure, drag and entropy generation rate for high enthalpy hypersonic flow in the presence of real gas effects on the blunt body for opposing jet and jet with forward facing cavity combinatorial technique is considered. The major conclusions drawn from the current numerical study are summmarized as follows:

Perfect gas assumption over−estimates the surface pressure and wave drag as the surface pressure found is much lower when the real gas effects are considered. Significant flow field and shock alterations are observed when the real gas reactions are taken into consideration. Coefficient of drag and entropy generation rate varies in almost similar manner for different flow conditions. Thus, this newly proposed thermodynamic parameter can be used as a tool along with drag to analyze the performance of combinatorial technique. Introduction of cavity reduces the surface pressure, drag and entropy generation rate but significant reduction in surface pressure and drag is noted when the opposing jet is turned on but this jet flow results in much higher entropy generation rate. For given jet pressure ratio, opposing jet technique predicts lower drag and entropy generation rate as compared to combinatorial technique.

CHAPTER 7

CONCLUSIONS AND FUTURE SCOPE

7.1 Summary

The present thesis work is centered on the computational investigation of various drag reduction techniques based on exergy destruction parameter, high enthalpy effects often encountered during high speed flights and thermodynamic analysis of opposing jet and its combination with forward facing cavity technique. To acheive this, a cell-centered the finite volume method based non-equilibrium laminar compressible coupled Navier-Stokes and species continuity equations solver is successfully developed in OP2 framework and employed to simulate these high speed flow pertarbations. This solver incorporates dependence of thermo-physical and flow properties on temperature of the flow. Initially, the in-house developed unstructured solver is well validated with measured experimental data for various flow condtions reported in open literature and results are highly encouraging. Then, the solver has been used for the detailed numerical investigations of low and high enthalpy high speed flows. Further, perfect and reacting gas solvers are compared to explore the effect of real gas on flow features and corresponding drag calculations. The major outcomes of the current study are summarised as follows,

1) Exergy Destruction and Drag Reduction Analysis of Active and Passive Techniques

Initial investigations are based on counter flow injection and spike based drag reduction techniques to compare them on a common parameter. These active and passive techniques are assessed or compared by percentage drag reduction parameter only. This performance assessing parameter is not suitable to compare two techniques of different categories, therefore, new thermodynamic parameter named percentage exergy destruction is proposed for the first time for their comparison. Thus, simulations are performed

for supersonic flow over hemisphere injecting counterflow jet for different flow conditions. Results showed monotonic variation for percentage drag reduction and percentage exergy destruction with increase in injection pressure ratio as shock strength reduces at elevated jet pressures. Also, associated wave drag and exergy destruction lowers with injection pressure. Injection effectiveness, unique parameter for counterflowing jet shows inversion characteristics indicating a peak at specific injection pressure ratio. Spike mounting has also been assessed for different lengths in hypersonic freestream and here as well percentage drag reduction and percentage exergy destruction showed inverse trend among them. Technique of injecting jet from the spike tip has also been considered to demonstrate the significance of percentage exergy destruction as a performance assessment parameter. Present investigations recommend percentage exergy destruction as a unified performance assessment parameter for passive, active and combinatorial drag reduction technique.

2) Analysis of Counter Flow Injection Technique at Elevated Enthalpy Hypersonic Reacting Flows

Investigations are also carried out to examine the effect of elevated freestream stagnation enthalpy on flow field alteration for counter−jet drag reduction technique for a hypersonic flow over hemispherical object. Effects of real gas flow on the flow field, wave drag and wall heat flux are also presented. Further the influence of various flow parameters such as freestream Mach number, jet pressure ratio is observed on surface pressure distribution, surface heat flux and associated drag coefficient. It was concluded that the perfect gas assumption overestimates surface properties and related wave drag. Drag coefficient lowers with the increase in freestream total enthalpy (H_o) in the presence of real gas effects. Around 30% drag reduction is observed at H_o=1 MJ/kg for Mach number 5 as compared to no−jet case and this reduction becomes significant at higher freestream total enthalpy for given jet pressure ratio. Higher pressure ratio of the jet results in lowering of surface pressure and Stanton number on the object which gives lower wave drag.

3) Thermodynamic Analysis for Opposing Jet Technique in Hypersonic Reacting Flows

Results are presented to reveal the thermodynamic behaviour of opposing jet technique which includes variation of entropy generation rate, exergy destruction and drag analysis considering real gas effects. In this context, high entahlpy hypersonic flow over the hemispherical body in the presence of real gas reactions is studied. Numerical simulations are performed for different flow and geometrical parameters of jet and freestream to examine their impact on flow field, drag reduction, exergy destruction and entropy generation rate. Results revealed that freestream parameters has lesser effect on drag values and flow field but there is monotonic variation in entropy generation rate and

exergy destruction for constant momentum ratio of the jet. For given momentum ratio, jet parameters gives almost linear reduction in entropy generation rate and exergy destuction while minor alterations in flow field and drag values are observed. Significant reduction in drag coefficient and sharp rise in entropy generation rate and exergy destruction is found with momentum ratio of the jet. Shock stand-off distance increases with jet momentum ratio resulting in lowering of surface pressure and related drag coefficient but on the other hand it enhances the region covered by higher temperature region at post shock location giving higher exergy destruction and entropy generation rate, making the shock formation process much more irreversible. Moreover, entropy generation rate and drag coefficient shows reverse variation with given freestream or jet parameter for constant jet momentum ratio. Present investigation recommend exergy destruction and entropy generation rate as a performance accessing parameter along with drag coefficient for opposing jet technique. Flow features and associated wave drag shows alterations with jet momentum ratio. Only jet momentum ratio can be considered as major governing parameter for the impact of jet in the freestream flow which alters the shock structure and associated recirculation zone which is responsible for considerable drag reduction at hypersonic reacting flows as well.

4) Drag and Entropy Generation Analysis for Combinatorial Technique

Real gas effect (non−equlibrium flow) on surface pressure and flow field is analysed for the combinatorial technique (opposing jet and cavity) for high enthalpy hypersonic flow over the blunt body. Drag variation and entropy generation rate are also noted for different flow conditions and associated flow field alterations are examined. Results showed that perfect gas assumption over−estimates the surface pressure and associated wave drag for given flow parameters and cavity configuration. Flow field and shock structure portrays considerable alterations when the real gas reactions are considered. Wave drag and entropy generation rate varies in monotonic manner for different flow conditions. Addition of cavity at the nose of blunted body lowers the surface pressure, drag and entropy generation rate to some extent but large reduction in these parameters is observed when the opposing jet is turned on. For given jet pressure ratio, opposing jet technique predicts lower drag and entropy generation rate as compared to combinatorial technique for real gas flows.

7.2 Future scope

Even though the current thesis work gives some useful insight of different essential aspects of high speed flows, still there are many unexplored future works which need to be carried out. Some important scope of future development related to current solver are

presented as follows:

1) The present work was carried out considering solution of laminar N-S equations along with species continuity equations. However, turbulence effects cannot be neglected for any drag reduction technique as it may give rise to unsteadiness in the flowfield resulting in significant alterations of interested properties. Inclusion of turbulence models like $k-\epsilon$ or $k-\omega$ into the present solver would be very helpful to investigate unsteadiness of the high speed flows to capture accurate flow variables.

2) The present solver can simulate only 2-D axisymmetry flows. Efforts can be made to make it more versatile with the addition of third direction so that the solver can effectively simulate various aspects of 3-D hypersonic flows.

3) Further, different chemical species of CO_2 gas like C, CO etc can be incorporated in the current solver so that its capability can be enhanced and it can be effectively employed to simulate high speed CO_2 flows like in Mars atmosphere.

4) Only single or combination of at the most two techniques has been studied in the present thesis. Thus, combination of three or more active and passive drag reduction techniques can be investigate to explore their influence on surface properties to obtain large reduction in drag values for non-equilibrium flows.

5) Efforts can be given to explore the effects of cavity configuration on flow features and related surface properties to improve the performance of introduction of cavity in the blunted body. Cavity dimensions can also be optimized for given body diameter and flow conditions to obtain minimal wave drag on the object.

6) Optimization studies can be carried out for any given active or passive drag reduction techniques in order to acheive minimum drag forces and surface heating to enhance the overall performance of air vehicles so as to minimize its fuel consumption and increase its durability.

PUBLICATIONS

Journal Articles

1) **Ajay Patil**, Shailendra Kumar and Vinayak Kulkarni, 'Analysis of counter flow injection technique at elevated enthalpy hypersonic reacting flows', **International Journal of Heat and Mass Transfer**, 182 (2022): 121893.
2) **Ajay Patil**, Shailendra Kumar, Siddesh Desai and Vinayak Kulkarni, 'Thermodynamic analysis of counter flow injection', **Acta Astronautica**, 199 (2022), 14-24.
3) **Ajay Patil** and Vinayak Kulkarni, 'Alterations in dynamics of counterjet injection technique in presence of real gas effects' **Materials Today: Proceedings**, 64 (2022), 1153-1159.
4) **Ajay Patil** and Vinayak Kulkarni, 'Surface heat flux analysis for opposing jet and combination techniques in the presence of real gas effect' **Materials Today: Proceedings**, 64 (2022), 1445-1449.

Conference Papers

1) **Ajay Patil**, Vinayak Kulkarni, 'Exergy Destruction and Drag Reduction for Opposing Jet Technique in Presence of Real Gas Reactions', Proceedings of the 26^{th} National and 4^{th} International ISHMT-ASTFE Heat and Mass Transfer Conference (**IHMTC-2021**), IIT Madras, Madras, 17-20 Dec, 2021, DOI: 10.1615/IHMTC-2021.750, pages 501-507.

APPENDIX

Table : Formulations of different flux computation schemes with suitable modifications

Scheme	**Flux formula**		**Terms**
	Interface flux $F_{I\perp} = F_I^+ + F_I^-$		$M_L^+ = \begin{cases} M_L, & \text{if, } M_L \geq 1 \\ \frac{1}{4}(M_L+1)^2 & \text{if, } \lvert M_L \rvert < 1 \\ 0 & \text{if, } M_L \leq -1 \end{cases}$
Vanleer	$F_I^+ = F_{I\perp}, F_I^- = 0$	if, $M_\perp \geq 1$	
FVM	$F_I^- = F_{I\perp}, F_I^+ = 0$	if, $M_\perp \leq -1$	
Van-Leer B	$F_{I\perp} = F_I^+ + F_I^-$	if, $-1 < M_\perp < 1$	

Continued on next page

Table – *Continued from previous page*

Scheme	Flux formula	Terms
Van-Leer	$\mathrm{F}_{I\perp} = \begin{bmatrix} \rho V \\ \rho u V + p n_x \\ \rho v V + p n_y \\ (\rho e + p) V \\ C_i V \end{bmatrix}$ i=1,2,..,N-1	$\mathrm{M}_R^- = \begin{cases} 0 & if, M_R \geq 1 \\ \frac{1}{4}(M_R+1)^2 & if, \lvert M_R \rvert < 1 \\ M_R & if, M_R \leq -1 \end{cases}$
FVM	$\mathrm{F}_I^{\pm} = \begin{bmatrix} f_{mass}^{\pm} \\ f_{mass}^{\pm}[u + n_x(-V \pm 2a)\frac{p}{\rho a^2}] \\ f_{mass}^{\pm}[v + n_y(-V \pm 2a)\frac{p}{\rho a^2}] \\ f_{mass}^{\pm}[H + m(-V \pm a)^2] \\ f_{mass}^{\pm}\frac{C_i}{\rho} \end{bmatrix}$	$\mathrm{M}_{\perp L} = \frac{V_L}{a_L}, M_{\perp R} = \frac{V_R}{a_R}$
Van-Leer B	if, $\lvert \mathrm{M}_L \rvert < 1$	$f_{mass}^{\pm} = +\rho_L a_L \frac{(M_L+1)^2}{4}$ $f_{mass}^{\pm} = -\rho_R a_R \frac{(M_R-1)^2}{4}$ $m = \frac{h}{a^2+2h}$ h is specific enthalpy and H is total enthalpy

Continued on next page

Table – *Continued from previous page*

Scheme	Flux formula	Terms
AUSM-delta hybrid	Interface flux $\mathrm{F}_{I\perp} = (M_n)_{I+1/2} \begin{bmatrix} \rho a \\ \rho a u \\ \rho a v \\ (\rho e + p)a \\ C_i a \end{bmatrix}_{L/R} + \begin{bmatrix} 0 \\ p n_x \\ p n_y \\ 0 \\ 0 \end{bmatrix}_{I+1/2}$ where $(\mathrm{M}_n)_{I+1/2} = M_L^+ + M_R^-$ $(\mathrm{p})_{I+1/2} = p_L^+ + p_R^-$ $(.)\mathrm{L/R} = = \begin{cases} (.)_L & if, M_{nI+1/2} \geq 0 \\ (.)_R & otherwise \end{cases}$	$\mathrm{p}_L^+ = \begin{cases} p_L & if, M_L \geq 1 \\ \frac{p_L}{4}(M_L+1)^2(2+M_L) & if, \lvert M_L \rvert < 1 \\ 0 & if, M_L \leq -1 \end{cases}$ $\mathrm{p}_R^- = \begin{cases} 0 & if, M_R \geq 1 \\ \frac{p_R}{4}(M_R-1)^2(2+M_R) & if, \lvert M_R \rvert < 1 \\ p_R & if, M_R \leq -1 \end{cases}$ To avoid zero advection Mach number $(M_n)_{I+1/2}$ is modified in AUSM-delta as, $\lvert \mathrm{M}_{nI+1/2} \rvert = \begin{cases} \lvert M_{nI+1/2} \rvert & if, \lvert M_{nI+1/2} \rvert > \delta \\ \frac{M_{nI+1/2}^2 + \delta^2}{2\delta} & if, \lvert M_{nI+1/2} \rvert \leq \delta \end{cases}$

Continued on next page

Table – *Continued from previous page*

Scheme	Flux formula	Terms
AUSM+	Interface flux	
hybrid	$\mathrm{F}_{I\perp} = m^{+}_{I+1/2}(a)_{I+1/2} \begin{bmatrix} \rho a \\ \rho a u \\ \rho a v \\ (\rho e + p)a \\ C_i a \end{bmatrix}_L + \mathrm{m}^{-}_{I+1/2}(a)_{I+1/2} \begin{bmatrix} \rho a \\ \rho a u \\ \rho a v \\ (\rho e + p)a \\ C_i a \end{bmatrix}_R + \begin{bmatrix} 0 \\ p m_x \\ p m_y \\ 0 \\ 0 \end{bmatrix}_{I+1/2}$	$\mathrm{M}^{\pm}_{L/R} = \begin{cases} \frac{1}{2}(M_{L/R} \pm \lvert M_{L/R}\rvert) & if, \lvert M_{L/R}\rvert > 1 \\ \frac{1}{2}(M_{L/R} \pm 1)^2 \pm \beta(M^2_{L/R} - 1)^2 & otherwise \end{cases}$
		where, $\frac{-1}{6} \le \beta \le \frac{1}{2}$
	$m_{I+1/2} = M^{+}_{L} + M^{-}_{R}, a_{I+1/2} = \sqrt{a_L a_R}$	
	$m^{\pm}_{I+1/2} = \frac{1}{2}(m_{I+1/2} + \lvert m_{I+1/2}\rvert)$	$\mathrm{p}_{L/R} = \begin{cases} \frac{1}{2}(1 \pm sign(M_{L/R})) & if, \lvert M_{L/R}\rvert \ge 1 \\ \frac{1}{4}(M_{L/R} \pm 1)^2 \pm (2 \mp M_{L/R}) \pm \alpha M_{L/R} \times (M^2_{L/R} - 1)^2 & otherwise \end{cases}$
		where, $\frac{-2}{4} \le \alpha \le \frac{3}{16}$
		$p_{I+1/2} = p^{+}_{L} + p^{-}_{R}$

Continued on next page

Table – *Continued from previous page*

Scheme	Flux formula	Terms
Rusanov FDM	Interface flux $F_{I\perp} = \frac{1}{2}(F_{IL} + F_{IR}) - \frac{1}{2}S^{+}(X_R - X_L)$ $\mathrm{F}_{L/R} = \begin{bmatrix} \rho V \\ \rho u V + p n_x \\ \rho v V + p n_y \\ (\rho e + p) V \\ C_i V \end{bmatrix}_{L/R}$	$S^{+} = max(V_L + S_L, V_L - S_L, S_L, V_R + S_R, V_R - S_R, S_R)$ $S_L and S_R$ can be calculated either from equation given below or can be approximated as corresponding sonic velocity at left and right of the face $S = \sqrt{\lambda^2 + \beta}, \lambda_o = u n_x + v n_y$ β = pseudo-compressibility parameter

REFERENCES

[1] W. Huang, A survey of drag and heat reduction in supersonic flows by a counter-flowing jet and its combinations, Journal of Zhejiang University-Science A 16 (7) (2015) 551–561.

[2] B. Shen, W. Liu, L. Yin, Drag and heat reduction efficiency research on opposing jet in supersonic flows, Aerospace Science and Technology 77 (2018) 696–703.

[3] I. d. S. Rego, P. G. d. P. Toro, M. A. S. Minucci, J. B. Chanes Junior, F. J. d. Costa, A. C. d. Oliveira, Calculation of the vehicle drag and heating reduction at hypervelocities with laser-induced air spike, Journal of Aerospace Technology and Management 5 (1) (2013) 43–48.

[4] M. Mortazavi, D. D. Knight, O. A. Azarova, J. Shi, H. Yan, Numerical simulation of energy deposition in a supersonic flow past a hemisphere, in: 52nd Aerospace Sciences Meeting, 2014, p. 0944.

[5] A. C. Fraile, M. A. P. Rosa, A numerical investigation of localized and steady energy addition to high speed airflows, Journal of Aerospace Technology and Management 5 (2013) 169–180.

[6] Y. Xue, L. Wang, S. Fu, Drag reduction and aerodynamic shape optimization for spike-tipped supersonic blunt nose, Journal of Spacecraft and Rockets 55 (3) (2018) 552–560.

[7] P. Finley, The flow of a jet from a body opposing a supersonic free stream, Journal of Fluid Mechanics 26 (2) (1966) 337–368.

[8] K. Hayashi, S. Aso, Y. Tani, Experimental study on thermal protection system by

opposing jet in supersonic flow, Journal of Spacecraft and Rockets 43 (1) (2006) 233–235.

[9] S. Li, W. Huang, J. Lei, Z. Wang, Drag and heat reduction mechanism of the porous opposing jet for variable blunt hypersonic vehicles, International Journal of Heat and Mass Transfer 126 (2018) 1087–1098.

[10] N. Morimoto, J. Y. Yoon, S. Aso, Y. Tani, Reduction of aerodynamic heating with opposing jet through extended nozzle in high enthalpy flow, in: 52nd Aerospace Sciences Meeting, 2014, p. 0705.

[11] W. Huang, R.-R. Zhang, L. Yan, M. Ou, R. Moradi, Numerical experiment on the flow field properties of a blunted body with a counterflowing jet in supersonic flows, Acta Astronautica 147 (2018) 231–240.

[12] V. Kulkarni, K. Reddy, Enhancement in counterflow drag reduction by supersonic jet in high enthalpy flows, Physics of Fluids 20 (1) (2008) 016103.

[13] B. Venukumar, G. Jagadeesh, K. Reddy, Counterflow drag reduction by supersonic jet for a blunt body in hypersonic flow, Physics of fluids 18 (11) (2006) 118104.

[14] B. Meyer, H. F. Nelson, D. W. Riggins, Hypersonic drag and heat-transfer reduction using a forward-facing jet, Journal of Aircraft 38 (4) (2001) 680–686.

[15] L. Hai-Bo, L. Wei-Qiang, Numerical investigation on properties of attack angle for an opposing jet thermal protection system, Chinese Physics B 21 (8) (2012) 084401.

[16] C. Zhou, W. Ji, A three-dimensional numerical investigation on drag reduction of a supersonic spherical body with an opposing jet, Proceedings of the Institution of Mechanical Engineers, Part G: Journal of Aerospace Engineering 228 (2) (2014) 163–177.

[17] C. H. E. Warren, An experimental investigation of the effect of ejecting a coolant gas at the nose of a bluff body, Journal of Fluid Mechanics 8 (3) (1960) 400–417.

[18] M. B. Gerdroodbary, O. Jahanian, M. Mokhtari, Influence of the angle of incident shock wave on mixing of transverse hydrogen micro-jets in supersonic crossflow, International Journal of Hydrogen Energy 40 (30) (2015) 9590–9601.

[19] E. O. Daso, V. E. Pritchett, T.-S. Wang, D. K. Ota, I. M. Blankson, A. H. Auslender, Dynamics of shock dispersion and interactions in supersonic freestreams with counterflowing jets, AIAA journal 47 (6) (2009) 1313–1326.

[20] M. B. Gerdroodbary, S. Bishehsari, S. Hosseinalipour, K. Sedighi, Transient analysis of counterflowing jet over highly blunt cone in hypersonic flow, Acta Astronautica 73 (2012) 38–48.

[21] D. Sahoo, S. Das, P. Kumar, J. Prasad, Effect of spike on steady and unsteady flow over a blunt body at supersonic speed, Acta Astronautica 128 (2016) 521–533.

[22] M. Lopatoff, Wind-flow study of pressure-drag reduction at transonic speed by projecting a jet of air from the nose of a prolate spheroid of fineness ratio 6.

[23] T. Imoto, H. Okabe, Y. Tani, Enhancement of aerodynamic heating reduction in high enthalpy flows with opposing jet, in: 49th AIAA Aerospace Sciences Meeting including the New Horizons Forum and Aerospace Exposition, 2011, p. 346.

[24] M. B. Gerdroodbary, M. Imani, D. Ganji, Heat reduction using conterflowing jet for a nose cone with aerodisk in hypersonic flow, Aerospace Science and Technology 39 (2014) 652–665.

[25] K. Karashima, S. Aso, G. Takami, K. Sato, Experimental study on self-induced excitation phenomena of opposing jet in supersonic flow, 22nd ICAS, 2000.

[26] I. Tamada, S. Aso, Y. Tani, Reducing aerodynamic heating by the opposing jet in supersonic and hypersonic flows, in: 48th AIAA Aerospace Sciences Meeting Including the New Horizons Forum and Aerospace Exposition, 2010, p. 991.

[27] Y. Zheng, N. Ahmed, W. Zhang, Heat dissipation using minimum counter flow jet ejection during spacecraft re-entry, Procedia engineering 49 (2012) 271–279.

[28] B.-Y. Min, J.-W. Lee, Y.-H. Byun, Numerical investigation of the shock interaction effect on the lateral jet controlled missile, Aerospace Science and Technology 10 (5) (2006) 385–393.

[29] B. Venukumar, K. Reddy, Experimental investigation of drag reduction by forward facing high speed gas jet for a large angle blunt cone at mach 8, Sadhana 32 (1-2) (2007) 123–131.

[30] S.-b. Li, Z.-g. Wang, W. Huang, J. Liu, Effect of the injector configuration for opposing jet on the drag and heat reduction, Aerospace Science and Technology 51 (2016) 78–86.

[31] C.-L. Chang, B. S. Venkatachari, G. Cheng, Effect of counterflow jet on a supersonic reentry capsule, in: 42nd AIAA/ASME/SAE/ASEE Joint Propulsion Conference & Exhibit, 2006, p. 4776.

[32] G. Cheng, K. Neroorkar, Y.-S. Chen, T.-S. Wang, E. Daso, Numerical study of flow augmented thermal management for entry and re-entry environments, in: 25th AIAA Applied Aerodynamics Conference, 2007, p. 4560.

[33] K. Hayashi, S. Aso, Y. Tani, Numerical study on aerodynamic heating reduction by opposing jet, AIAA Journal 66 (1).

[34] S. Bilal Hussain Shah, X.-Y. Lu, Computational study of drag reduction at various freestream flows using a counterflow jet from a hemispherical cylinder, Engineering Applications of Computational Fluid Mechanics 4 (1) (2010) 150–163.

[35] K. Hayashi, S. Aso, Effect of pressure ratio on aerodynamic heating reduction due to opposing jet, in: 36th AIAA Thermophysics Conference, 2003, p. 4041.

[36] J. Hefner, J. Keyes, Effect of forward-facing jets on aerodynamic characteristics of blunt configurations at mach 6., Journal of Spacecraft and Rockets 4 (4) (1967) 533–534.

[37] J. R. Stalder, M. Inouye, A method of reducing heat transfer to blunt bodies by air injection, Tech. rep., National Aeronautics And Space Administration Washington Dc (1956).

[38] S. Aso, M. KAWAI, Y. ANDO, Experimental study on mixing phenomena in supersonic flows with slot injection, in: 29th Aerospace sciences meeting, 1991, p. 16.

[39] R. Sriram, G. Jagadeesh, Film cooling at hypersonic mach numbers using forward facing array of micro-jets, International journal of heat and mass transfer 52 (15-16) (2009) 3654–3664.

[40] S. Aruna, S. Anjalidevi, Computational study on the influence of jet on reduction of drag over cone flare bodies in hypersonic turbulent flow, Procedia engineering 38 (2012) 3635–3648.

[41] Y. Amini, M. Mokhtari, M. Haghshenasfard, M. B. Gerdroodbary, Heat transfer of swirling impinging jets ejected from nozzles with twisted tapes utilizing cfd technique, Case Studies in Thermal Engineering 6 (2015) 104–115.

[42] D. Roupassov, A. Nikipelov, M. Nudnova, A. Y. Starikovskii, Flow separation control by plasma actuator with nanosecond pulsed-periodic discharge, AIAA journal 47 (1) (2009) 168–185.

[43] N. Sahoo, V. Kulkarni, S. Saravanan, G. Jagadeesh, K. Reddy, Film cooling effectiveness on a large angle blunt cone flying at hypersonic speed, Physics of Fluids 17 (3) (2005) 036102.

[44] J. Shang, J. Hayes, J. Menart, Hypersonic flow over a blunt body with plasma injection, Journal of Spacecraft and Rockets 39 (3) (2002) 367–375.

[45] J. Poggie, Plasma-based hypersonic flow control, in: 37th AIAA Plasmadynamics and Lasers Conference, 2006, p. 3567.

[46] J. S. Shang, R. L. Kimmel, J. Menart, S. T. Surzhikov, Hypersonic flow control using surface plasma actuator, Journal of Propulsion and Power 24 (5) (2008) 923–934.

[47] Y. Watanabe, K. Suzuki, Effectiveness of direct current arc plasma discharge on aerodynamic control in hypersonic flow, TRANSACTIONS OF THE JAPAN SOCIETY FOR AERONAUTICAL AND SPACE SCIENCES, AEROSPACE TECHNOLOGY JAPAN 12 (ists29) (2014) Pe_1–Pe_4.

[48] W. Mair, Lxviii. experiments on separation of boundary layers on probes in front of blunt-nosed bodies in a supersonic air stream, The London, Edinburgh, and Dublin Philosophical Magazine and Journal of Science 43 (342) (1952) 695–716.

[49] D. Maull, Hypersonic flow over axially symmetric spiked bodies, Journal of Fluid Mechanics 8 (4) (1960) 584–592.

[50] C. Wood, Hypersonic flow over spiked cones, Journal of Fluid Mechanics 12 (4) (1962) 614–624.

[51] J. P. Reding, R. A. Guenther, B. J. Richter, Unsteady aerodynamic considerations in the design of a drag-reduction spike, Journal of Spacecraft and Rockets 14 (1) (1977) 54–60.

[52] A. G. Mikhail, Spike-nosed projectiles with vortex rings: steady and nonsteady flow simulations, Journal of Spacecraft and Rockets 33 (1) (1996) 8–14.

[53] S. S. Milicev, M. D. Pavlovic, Influence of spike shape at supersonic flow past blunt-nosed bodies: experimental study., AIAA journal 40 (5) (2002) 1018–1020.

[54] V. Menezes, S. Saravanan, K. Reddy, Shock tunnel study of spiked aerodynamic bodies flying at hypersonic mach numbers, Shock Waves 12 (3) (2002) 197–204.

[55] M. Gilinsky, C. Washington, I. Blankson, A. Shvets, Spike-nosed bodies and forward injected jets in supersonic flow, in: 38th AIAA/ASME/SAE/ASEE Joint Propulsion Conference & Exhibit, 2002, p. 3918.

[56] V. Kulkarni, V. Menezes, K. Reddy, Effectiveness of aerospike for drag reduction on a blunt cone in hypersonic flow, Journal of Spacecraft and Rockets 47 (3) (2010) 542–544.

[57] R. Mehta, Numerical heat transfer study around a spiked blunt-nose body at mach 6, Heat and Mass Transfer 49 (4) (2013) 485–496.

[58] R. Yadav, G. Velidi, U. Guven, Aerothermodynamics of generic re-entry vehicle with a series of aerospikes at nose, Acta Astronautica 96 (2014) 1–10.

[59] S. Mohandas, R. K. Siddharth, B. John, Reduction of wave drag on parameterized blunt bodies using spikes with varied tip geometries, Acta Astronautica 160 (2019) 25–35.

[60] S. Srinath, K. J. Reddy, Experimental investigation of the effects of aerospike geometry on aerodynamic drag and heat transfer rates for a blunt body configuration at hypersonic mach numbers, International Journal of Hypersonics.

[61] S. Khurana, K. Suzuki, E. Rathakrishnan, Flow field around a blunt-nosed body with spike, Int. J. Turbo Jet-Engines 29 (4) (2012) 217–221.

[62] R. Kalimuthu, R. C. Mehta, E. Rathakrishnan, Drag reduction for spike attached to blunt-nosed body at mach 6, Journal of Spacecraft and Rockets 47 (1) (2010) 219–222.

[63] E. Jones, S. Townsend, Y. Guy, T. McLaughlin, Reduction of the wave drag of a blunt body by means of a standoff spike, in: 38th Aerospace Sciences Meeting and Exhibit, 2000, p. 268.

[64] Y. Guy, T. McLaughlin, J. Morrow, Blunt body wave drag reduction by means of a standoff spike, in: 39th Aerospace Sciences Meeting and Exhibit, 2001, p. 888.

[65] G. d Humieres, J. Stollery, Drag reduction on a spiked body at hypersonic speed, The Aeronautical Journal 114 (1152) (2010) 113–119.

[66] M. Gauer, A. Paull, Numerical investigation of a spiked blunt nose cone at hypersonic speeds, Journal of Spacecraft and Rockets 45 (3) (2008) 459–471.

[67] S. Kumar, V. Kulkarni, S. P. Jammy, Aerothermodynamic assessment of spiked configuration for drag reduction at hypersonic speeds, Journal of Aerospace Engineering 33 (6) (2020) 04020076.

[68] D. Knight, Survey of aerodynamic drag reduction at high speed by energy deposition, Journal of Propulsion and Power 24 (6) (2008) 1153–1167.

[69] V. Y. Borzov, I. Rybka, A. Yur'ev, Effect of local energy supply to a hypersonic flow on the drag of bodies with different nose bluntness, Journal of engineering physics and thermophysics 67 (5) (1994) 997–1002.

[70] V. Levin, L. Terent'eva, Supersonic flow over a cone with heat release in the neighborhood of the apex, Fluid dynamics 28 (2) (1993) 244–247.

[71] V. Levin, V. Gromov, N. Afonina, Numerical analysis of the effect of local energy supply on the aerodynamic drag and heat transfer of a spherically blunted body in a supersonic air flow, Journal of Applied Mechanics and Technical Physics 41 (5) (2000) 915–922.

[72] V. Vlasov, B. Grudnitskii, V. Rygalin, Gas dynamics with local energy release in subsonic and supersonic flow, Fluid dynamics 30 (2) (1995) 275–280.

[73] R. Bracken, L. Myrabo, H. Nagamatsu, E. Meloney, M. Shneider, Experimental investigation of an electric arc air-spike in mach 10 flow with preliminary drag measurements, in: 32nd AIAA Plasmadynamics and Lasers Conference, 2001, p. 2734.

[74] P. Y. Georgievskii, V. Levin, Control of the flow past bodies using localized energy addition to the supersonic oncoming flow, Fluid Dynamics 38 (5) (2003) 794–805.

[75] E. Erdem, L. Yang, K. Kontis, Drag reduction studies by steady energy deposition at mach 5, in: 49th AIAA Aerospace Sciences Meeting including the New Horizons Forum and Aerospace Exposition, 2011, p. 1027.

[76] D. R. Gutierrez, J. Poggie, Effects of power deposition on the aerodynamic forces on a slender body, AIAA Journal 56 (7) (2018) 2911–2917.

[77] V. Kulkarni, G. Hegde, G. Jagadeesh, E. Arunan, K. Reddy, Aerodynamic drag reduction by heat addition into the shock layer for a large angle blunt cone in hypersonic flow, Physics of Fluids 20 (8) (2008) 081703.

[78] M. A. Ganesh, B. John, Concentrated energy addition for active drag reduction in hypersonic flow regime, Acta Astronautica 142 (2018) 221–231.

[79] M. Shneyder, S. Macheret, S. Zaidi, I. Girgis, R. Miles, Steady and unsteady supersonic flow control with energy addition, in: 34th AIAA Plasmadynamics and Lasers Conference, 2003, p. 3862.

[80] S. Desai, V. Kulkarni, H. Gadgil, B. John, Aerothermodynamic considerations for energy deposition based drag reduction technique, Applied Thermal Engineering 122 (2017) 451–460.

[81] D. Das, S. Desai, V. Kulkarni, H. Gadgil, Performance assessment of energy deposition based drag reduction technique for earth and mars flight conditions, Acta Astronautica 159 (2019) 418–428.

[82] P. Georgievsky, V. Levin, Bow shock wave structures control by pulse-periodic energy input, in: 42nd AIAA Aerospace Sciences Meeting and Exhibit, 2004, p. 1019.

[83] A. Tahsini, Heat release effects on drag reduction in high speed flows, International Journal of Heat and Mass Transfer 57 (2) (2013) 657–661.

[84] S. Zaidi, M. Shneider, D. Mansfield, Y. Ionikh, R. Miles, Influence of upstream pulsed energy addition on shock-wave structure in supersonic flow, in: 22nd AIAA Aerodynamic Measurement Technology and Ground Testing Conference, 2002, p. 2703.

[85] Y. Ogino, N. Ohnishi, S. Taguchi, K. Sawada, Baroclinic vortex influence on wave drag reduction induced by pulse energy deposition, Physics of fluids 21 (6) (2009) 066102.

[86] A. R. Sangtabi, A. Ramiar, A. A. Ranjbar, M. Abdollahzadeh, A. Kianifar, Influence of repetitive laser pulse energy depositions on supersonic flow over a sphere, cone and oblate spheroid, Aerospace Science and Technology 76 (2018) 72–81.

[87] R. Kandala, G. V. Candler, Numerical studies of laser-induced energy deposition for supersonic flow control, AIAA journal 42 (11) (2004) 2266–2275.

[88] A. Zheltovodov, E. Pimonov, D. Knight, Energy deposition influence on supersonic flow over axisymmetric bodies, in: 45th AIAA Aerospace Sciences Meeting and Exhibit, 2007, p. 1230.

[89] S. Saravanan, G. Jagadeesh, K. Reddy, Investigation of missile-shaped body with forward-facing cavity at mach 8, Journal of Spacecraft and Rockets 46 (3) (2009) 577–591.

[90] F. Xiao, Z. Li, Y. Zhu, J. Yang, Experimental and numerical study of hypersonic type iv shock interaction on blunt body with forward facing cavity, in: 20th AIAA International Space Planes and Hypersonic Systems and Technologies Conference, 2015, p. 3666.

[91] S. I. Silton, D. B. Goldstein, Use of an axial nose-tip cavity for delaying ablation onset in hypersonic flow, Journal of Fluid Mechanics 528 (2005) 297.

[92] K. Mohri, R. Hillier, Computational and experimental study of supersonic flow over axisymmetric cavities, Shock Waves 21 (3) (2011) 175–191.

[93] L. Zhu, Y. Li, L. Gong, X. Chen, J. Xu, Coupled investigation on drag reduction and thermal protection mechanism induced by a novel combinational spike and multi-jet strategy in hypersonic flows, International Journal of Heat and Mass Transfer 131 (2019) 944–964.

[94] J. Shang, J. Hayes, K. Wurtzler, W. Strang, Jet-spike bifurcation in high-speed flows, AIAA journal 39 (6) (2001) 1159–1165.

[95] W. Huang, J. Liu, Z.-x. Xia, Drag reduction mechanism induced by a combinational opposing jet and spike concept in supersonic flows, Acta Astronautica 115 (2015) 24–31.

[96] Z. Jiang, Y. Liu, G. Han, W. Zhao, Experimental demonstration of a new concept of drag reduction and thermal protection for hypersonic vehicles, Acta Mechanica Sinica 25 (3) (2009) 417–419.

[97] W. Huang, Y.-p. Jiang, L. Yan, J. Liu, Heat flux reduction mechanism induced by a combinational opposing jet and cavity concept in supersonic flows, Acta Astronautica 121 (2016) 164–171.

[98] H. Lu, W. Liu, Investigation of thermal protection system by forward-facing cavity and opposing jet combinatorial configuration, Chinese Journal of Aeronautics 26 (2) (2013) 287–293.

[99] X.-w. Sun, Z.-y. Guo, W. Huang, S.-b. Li, L. Yan, A study of performance parameters on drag and heat flux reduction efficiency of combinational novel cavity and opposing jet concept in hypersonic flows, Acta Astronautica 131 (2017) 204–225.

[100] W. Huang, L. Yan, J. Liu, L. Jin, J.-g. Tan, Drag and heat reduction mechanism in the combinational opposing jet and acoustic cavity concept for hypersonic vehicles, Aerospace Science and Technology 42 (2015) 407–414.

[101] M. Ou, L. Yan, W. Huang, S.-b. Li, L.-q. Li, Detailed parametric investigations on drag and heat flux reduction induced by a combinational spike and opposing jet concept in hypersonic flows, International Journal of Heat and Mass Transfer 126 (2018) 10–31.

[102] X.-w. Sun, Z.-y. Guo, W. Huang, S.-b. Li, L. Yan, Drag and heat reduction mechanism induced by a combinational novel cavity and counterflowing jet concept in hypersonic flows, Acta Astronautica 126 (2016) 109–119.

[103] H.-B. Lu, W.-Q. Liu, Research on thermal protection mechanism of forward-facing cavity and opposing jet combinatorial thermal protection system, Heat and Mass Transfer 50 (4) (2014) 449–456.

[104] L. L. Moore, A solution of the laminar boundary-layer equations for a compressible fluid with variable properties, including dissociation, Journal of the Aeronautical Sciences 19 (8) (1952) 505–518.

[105] J. A. Fay, F. R. Riddell, Theory of stagnation point heat transfer in dissociated air, Journal of the Aerospace Sciences 25 (2) (1958) 73–85.

[106] P. H. Rose, W. I. Stark, Stagnation point heat-transfer measurements in dissociated air, Journal of the Aerospace Sciences 25 (2) (1958) 86–97.

[107] P. H. Rose, J. Stankevics, Stagnation point heat transfer measurements in partially ionized air, AIAA Journal 1 (12) (1963) 2752–2763.

[108] S. J. Fenster, Stagnation-point heat transfer for a new binary air model including dissociation and ionization., AIAA Journal 3 (12) (1965) 2189–2196.

[109] R. Conti, M. Van Dyke, Inviscid reacting flow near a stagnation point, Journal of Fluid Mechanics 35 (4) (1969) 799–813.

[110] Y. Liu, M. Vinokur, Upwind algorithms for general thermo-chemical nonequilibrium flows, in: 27th Aerospace Sciences Meeting, 1989, p. 201.

[111] B. Grossman, P. Cinnella, Flux-split algorithms for flows with non-equilibrium chemistry and vibrational relaxation, Journal of Computational Physics 88 (1) (1990) 131–168.

[112] M. Netterfield, Validation of a navier-stokes code for thermochemical non-equilibrium flows, in: 27th Thermophysics Conference, 1992, p. 2878.

[113] C. Park, Assessment of a two-temperature kinetic model for dissociating and weakly ionizing nitrogen, Journal of Thermophysics and Heat Transfer 2 (1) (1988) 8–16.

[114] C. Park, Review of chemical-kinetic problems of future nasa missions. i-earth entries, Journal of Thermophysics and Heat transfer 7 (3) (1993) 385–398.

[115] M. L. Sawley, S. Wuthrich, Non-equilibrium hypersonic flow simulations using the second-order boundary layer equations, Computer methods in applied mechanics and engineering 89 (1-3) (1991) 129–140.

[116] F. Sabetta, B. Favini, G. Moretti, M. Onofri, M. Valorani, Reactive and inert inviscid flow solutions by quasi-linear formulations and shock fitting, in: Hypersonic Flows for Reentry Problems, Springer, 1991, pp. 782–797.

[117] S. Kumar, V. Kulkarni, Drag of a spiked body in chemically reacting hypersonic flow, Journal of Spacecraft and Rockets 57 (5) (2020) 1092–1097.

[118] S. Gordon, B. J. McBride, Computer program for calculation of complex chemical equilibrium, NASA reference publication 1311.

[119] J.-S. Shuen, M.-S. Liou, B. Van Leer, Inviscid flux-splitting algorithms for real gases with non-equilibrium chemistry, Journal of Computational Physics 90 (2) (1990) 371–395.

[120] B. Van Leer, Flux-vector splitting for the euler equation, in: Upwind and high-resolution schemes, Springer, 1997, pp. 80–89.

[121] M.-S. Liou, C. J. Steffen Jr, A new flux splitting scheme, Journal of Computational physics 107 (1) (1993) 23–39.

[122] M.-S. Liou, A sequel to ausm: Ausm+, Journal of computational Physics 129 (2) (1996) 364–382.

[123] V. V. Rusanov, Calculation of interaction of non-steady shock waves with obstacles, NRC, Division of Mechanical Engineering, 1962.

[124] T. Barth, D. Jespersen, The design and application of upwind schemes on unstructured meshes, in: 27th Aerospace sciences meeting, 1989, p. 366.

[125] J. Blazek, Computational fluid dynamics: principles and applications, Butterworth-Heinemann, 2015.

[126] T. J. Poinsot, S. Lelef, Boundary conditions for direct simulations of compressible viscous flows, Journal of computational physics 101 (1) (1992) 104–129.

[127] T. R. Bussing, E. M. Murman, Finite-volume method for the calculation of compressible chemically reacting flows, AIAA journal 26 (9) (1988) 1070–1078.

[128] B. John, G. Sarath, V. Kulkarni, G. Natarajan, Performance comparison of flux schemes for numerical simulation of high-speed inviscid flows, Progress in Computational Fluid Dynamics, an International Journal 14 (2) (2014) 83–96.

[129] W. S. LII, The viscosity of gases and molecular force, Lond. Edinb. Dublin Philos. Mag. J. Sci 36 (1893) 507–531.

[130] A. BEJAN, Advanced engineering thermodynamics. new york: Editorial john wiley & sons (2006).

[131] S. Desai, V. Prakash K, V. Kulkarni, H. Gadgil, Universal scaling parameter for a counter jet drag reduction technique in supersonic flows, Physics of Fluids 32 (3) (2020) 036105.

[132] G. Mudalige, M. Giles, I. Reguly, C. Bertolli, P. Kelly, Op2: An active library framework for solving unstructured mesh-based applications on multi-core and many-core architectures, in: 2012 Innovative Parallel Computing (InPar), IEEE, 2012, pp. 1–12.

[133] A. Patil, S. Kumar, S. Desai, V. Kulkarni, Thermodynamic analysis of counter flow injection, Acta Astronautica 199 (2022) 14–24.

[134] L.-W. Chen, G.-L. Wang, X.-Y. Lu, Numerical investigation of a jet from a blunt body opposing a supersonic flow, Journal of Fluid Mechanics 684 (2011) 85–110.

[135] S. Desai, V. Kulkarni, H. Gadgil, Delusive influence of nondimensional numbers in canonical hypersonic nonequilibrium flows, Journal of Aerospace engineering 29 (5) (2016) 04016030.

[136] F. S. Billig, Shock-wave shapes around spherical-and cylindrical-nosed bodies., Journal of Spacecraft and Rockets 4 (6) (1967) 822–823.

[137] S.-b. Li, Z.-g. Wang, W. Huang, J. Liu, Drag and heat reduction performance for an equal polygon opposing jet, Journal of Aerospace Engineering 30 (1) (2017) 04016065.

[138] L. Zhu, Y. Li, X. Chen, L. Gong, J. Xu, Z. Feng, Novel combinational aerodisk and lateral jet concept for drag and heat reduction in hypersonic flows, Journal of Aerospace Engineering 32 (1) (2019) 04018133.

[139] S. Desai, Numerical study of flow alteration techniques and high temperature effects at supersonic/hypersonic speeds, Ph.D. thesis (2019).

[140] S. Reddy, K. Sinha, Analysis of high-enthalpy air-chemistry and its effect on stagnation point heat flux, in: 43rd AIAA Thermophysics Conference, 2012, p. 3002.

[141] D. O. Iyinomen, Numerical approach to ablation measurements using a new plasma pre-heating technique, International Journal of Thermofluids 1 (2020) 100014.

[142] R. N. Gupta, J. M. Yos, R. A. Thompson, K.-P. Lee, A review of reaction rates and thermodynamic and transport properties for an 11-species air model for chemical and thermal nonequilibrium calculations to 30000 k, NASA STI/Recon Technical Report N 90 (1990) 27064.

[143] R. Yisheng, Drag reduction research in supersonic flow with opposing jet, Acta Astronautica 91 (2013) 1–7.

[144] A. Patil, S. Kumar, V. Kulkarni, Analysis of counter flow injection technique at elevated enthalpy hypersonic reacting flows, International Journal of Heat and Mass Transfer 182 (2022) 121893.